Bubble Generation under Turbulent Conditions within a Steelmaking Ladle Shroud: A Water Modeling and CFD Study

Xinyu Ren

Materials Engineering
McGill University

April 2015

A thesis submitted to McGill University in partial fulfillment of the requirements of the degree of Master of Engineering

Abstract

The mechanism of bubble generation under turbulent conditions within a steelmaking ladle shroud was studied experimentally by water modelling, and mathematically by CFD (Computational Fluid Dynamics) simulation. The sizes of bubbles generated were quantitatively characterized through optical measurements. Based on the bubble size distributions, six potentially important experimental parameters were assessed. The optimal operating condition for the generation of small bubbles in the steelmaking ladle shroud was proposed, based on combining the experimental data and CFD results.

To directly produce super clean steel, one key task for the steelmaking industry is to remove tiny inclusions less than 50μm as far as possible. However, due to their low rising velocity, these tiny inclusions remain in the liquid steel entering into the casting processes. Small gas bubbles (0.25mm to 3.0mm) could enhance the removal efficiency of small inclusions from the liquid steel [1-4]. Due to the high surface tension of liquid steel, and the non-wetting characteristics, traditional gas injection techniques, such as lances, porous plug, orifices can only produce gas bubbles in the range of 10-50mm diameters under conditions applying to liquid steel. Nonetheless, the technique of micro-bubble generation in the ladle shroud is now proposed.

In the water modelling experiments, a new tundish model was built which provided the possibility to quantitatively characterize the sizes of bubbles generated. Six experimental factors were studied: the water speed in the ladle shroud model, the air injection rate, the slide gate opening ratio, the gas injection point distance from the slide gate, the air injection direction orientation and the orifice size. The experimental results showed that the water speed and the slide gate opening ratio determined the critical bubble size of the system. A high water speed and a low slide gate opening ratio lead to smaller critical bubble sizes. In general, the bubble size increased with any increase of the air injection rate and increase in the gas injection point distance from the slide gate. Therefore, the air injection rate must be kept low and the gas injection point should be located as close to the slide gate as possible, in order to generate very small bubbles. The direction of air injection and the orifice size did not show very strong correlations with the bubble sizes in the current experimental setups and conditions. The smallest bubbles

generated from the experiments were about 0.5mm in diameter, which are predicted to be the optimum for removing mall inclusions (10-50μm) from liquid steel.

In the CFD simulation, the commercial code package Ansys Fluent (version 14.5.7) was used. The simulations were carried out using the high performance computer in the McGill Metals Processing Centre (MMPC) at Stinson laboratory. The simulation results, particularly the local turbulence dissipation rate values, were used to calculate the theoretical critical bubble size. The trajectories of bubbles with different sizes were studied using the so-called discrete phase modelling (DPM). The mathematical simulation results were found to match with the experimental results reasonably well.

Finally, a physical model analysis was performed by combining the results from the water modelling experiments and the CFD simulations. The optimal condition to produce small bubbles by injecting gas into ladle shroud is proposed in the end of this research.

Résumé

Le mécanisme qui mène à la création de bulles durant l'écoulement turbulent de l'acier liquide dans le canal de coulée entre la poche et le distributeur d'une aciérie a été étudié. Cette étude a été divisée en deux volets : un volet expérimental avec des expériences à l'eau et un volet mathématique avec des simulations en mécanique de fluides numérique (MFN). La distribution des grosseurs des bulles dans les expériences à l'eau a été mesurée visuellement. Six paramètres pouvant influencer ces distributions ont été identifiés et étudiés. Les conditions idéales pour produire des petites bulles dans le canal de coulée ont été proposées selon les résultats des expériences à l'eau et de la MFN.

Une des tâches les plus importantes pour produire de l'acier propre consiste à éliminer les inclusions de moins de 50 μm de diamètre. Malheureusement, dû au temps requis pour qu'ils soient éliminés par eux-mêmes en flottant à la surface de l'acier liquide, la plupart de ces inclusions demeurent dans l'acier même après la coulée. L'ajout de petites bulles (0.25 mm à 3.0 mm de diamètre) pourrait accélérer l'élimination de ces inclusions [1-4]. Les méthodes d'injection de gaz couramment utilisées en sidérurgie (lance, bouchon poreux, orifice) ne sont pas capables de produire des bulles de cette grosseur. Elles ne peuvent produire que des bulles de 10 mm à 50 mm de diamètre due à la haute tension superfielle de l'acier liquide et de ses propriétés non-mouillantes. Une nouvelle technique pour la production de petites bulles dans le canal de coulée est donc proposée.

Pour les expériences à l'eau, un modèle d'un distributeur a été conçu qui permet l'observation des bulles produites. Six paramètres expérimentaux ont été étudiés : la vitesse d'écoulement de l'eau dans le canal de coulée, le taux d'injection du gaz, la proportion de l'ouverture du canal de coulée qui est ouverte, la distance entre le lieu d'injection du gaz et l'ouverture du canal de coulée, la direction de l'injection du gaz ainsi que la grosseur de l'orifice d'injection. Les résultats expérimentaux démontrent que la vitesse d'écoulement de l'eau et la proportion de l'ouverture du canal de coulée qui est ouverte déterminent la grosseur critique des bulles. Une vitesse d'écoulement élevée et une petite proportion de l'ouverture du canal de coulée qui est ouverte mènent à des bulles plus petites. En général, un taux plus élevé d'injection du gaz et une plus grande distance entre le lieu d'injection du gaz et l'ouverture du canal de coulée étaient liés à une

augmentation de la grosseur des bulles. Il faudrait donc minimiser ces deux paramètres. La direction de l'injection du gaz n'avait aucun effet significatif sur la grosseur des bulles dans les conditions expérimentales utilisées. Les plus petites bulles produites avaient un diamètre d'environ 0.5 mm. Il est prédit que les bulles de cette grosseur sont les plus efficaces pour éliminer les petites inclusions (10 μm à 50 μm de diamètre) de l'acier liquide.

Pour les simulations en MFN, le logiciel commercial Ansys Fluent (version 14.5.7) a été utilisé. Les simulations ont été réalisées sur un ordinateur à haute performance dans le *McGill Metals Processing Centre* (MMPC) au laboratoire Stinson. Les résultats des simulations, en particulier les valeurs pour la dissipation d'énergie due à la turbulence, ont été utilisés pour calculer la grosseur critique théorique des bulles. Les trajectoires des bulles de différentes grosseurs ont été étudiées avec la méthode *Discrete Phase Modelling* (DPM). Les résultats des simulations mathématiques sont semblables aux résultats expérimentaux.

Finalement, une analyse a été réalisée en combinant les résultats des expériences à l'eau et des simulations mathématiques afin de déterminer les conditions idéales pour produire des petites bulles en injectant du gaz dans le canal de coulée. Ces conditions sont détaillées à la fin de ce texte.

Acknowledgements

Foremost, I would like to express the deepest appreciation to my supervisors, Prof. Roderick Guthrie and Dr. Mihaiela Isac for their continuous academic advice and support during my Master's study at McGill University. My sincere thanks also to Dr. Luis Calzado for his support in my experimental setups.

Sincere thanks to Yumin Zhang, Link Ding and Dr. Sa Ge for their help and support during my studies at McGill University.

Special thanks to my colleges and friends in the McGill Metals Processing Centre (MMPC), and the McGill Mineral Processing Group, for their help and support to improve my water modelling experiments and the mathematical simulation models. Special thanks to Jonathan Spring for translating my thesis abstract into French.

I would also like to acknowledge the financial supporting from NSERC and the MMPC supporting companies. Special thanks to ANSYS for providing licenses for the CFD simulations.

Most importantly, I would like to express my sincere gratitude to my loving parents and elder sister for their unconditional love and endless patience.

Table of Contents

Nomenclature

ρ, Density of the fluid, Kg m^{-3}

g, Acceleration due to gravity, m s^{-2}

σ, Surface tension, N m^{-1}

ε, Rate of dissipation of k, m^2 s^{-3}

k, Kinetic energy of turbulence per unit mass, m^2 s^{-2}

μ, Viscosity of the fluid, kg m^{-1} s^{-1}

u_p, Particle velocity, m s^{-1}

u_b, Bubble velocity, m s^{-1}

$u_{aggregate}$, Aggregate velocity, m s^{-1}

P_{total}, Overall probability of inclusion removal, %

P_a, Probability of inclusion attach to bubble, %

P_c, Probability of inclusion collide to bubble, %

$P_{de\text{-}a}$, Probability of inclusion detach from bubble-inclusion aggregate, %

D_p, Particle diameter, m

D_b, Bubble diameter, m

D_{32}, Sauter mean diameter, m

D_{10}, Average diameter, m

Q, Flow rate, m^3/s

τ_{Bubble}, Restoring pressure, N m^{-2}

$\tau_{Turbulence}$, Deformation pressure, N m^{-2}

η, Kolmogorov microscale, m

β, Constant

u, velocity, m s^{-1}

u, X component of velocity, m s^{-1}

v, Y component of velocity, m s^{-1}

w, Z component of velocity, m s^{-1}

C_1, C_2, C_μ, σ_κ, σ_ε, Empirical constants

a_1, a_2, a_3, Constants

We, Weber number

We_{cr}, Critical Weber number

Re , Reynolds number

Eo, Eötvös number

CFD, Computational fluid dynamics

CAD, Computer-aided design

DPM, Discrete Phase Modeling

EAF, Electric Arc Furnace

PMMA, Poly(methyl methacrylate)

PIV, Particle Image Velocimetry

DNS, Direct Numerical Simulation

LCD, Liquid Crystal Display

LED, Light Emitting Diode

DSLR, Digital Single-lens Reflex Camera

LES, Large Eddy Simulation

SIMPLE, Semi-Implicit Method for Pressure linked Equations

PISO, Pressure Implicit Splitting of Operators

PRESTO, Pressure Staggering Option

RTD, Residence Time Distribution

Introduction

There is an increasing demand for cleaner steels. The cleanness level of steel largely depends on the inclusions. Inclusion size, volume fraction and composition heavily influence the final steel's mechanical properties. For example oxides can lower a steel's ductility. Inclusions can also act as stress raisers. Therefore inclusions quantity must be controlled low to produce clean steels.

Most inclusions are lighter than liquid steel. Therefore the inclusions will spontaneously float up due to the synergy of the gravity force and the buoyancy force. However, the size of the inclusion plays an important role in determining the removal efficiency of the inclusions. Typically, large inclusions (75-150μm) have large rising velocity. Hence, those large inclusions can be removed from the liquid steel through floatation to the slag surface or sticking to the tundish wall [5]. Small inclusions (less than 50μm), on the other hand, cannot be directly removed from the liquid steel efficiently due to their low rising velocity. Instead, the small inclusions tend to follow the flow of the liquid steel and enter into the casting processes.

Needless to say, it will be hugely beneficial for steelmaking industry, both economically and technologically, if these small inclusions could be removed directly in the liquid steel refining processes, which means direct production of super clean steel. In the past few decades, academic researchers and steelmaking industries have tried to use gas bubbles to enhance the removal efficiency of small inclusions. Bubbles were introduced into the liquid metal generally through two approaches: first, to introduce gas bubbles through a porous media located on the bottom of a tundish; second, to inadvertently introduce gas bubbles through orifices located at the ladle shroud, where an inert gas is introduced to prevent oxygen entering into the liquid steel.

Despite which route is taken, all the studies in both water modeling experiments and liquid steel experiments reached the same conclusions: 1, gas bubbles can improve the removal rate of the small inclusions by attaching the gas bubbles with the small inclusions and increase the rising velocity of the aggregates 2, small gas bubbles (0.25-3mm) are required to remove small inclusions; if the bubbles are large (3-5mm), it is not longer beneficial to have them in the liquid metal system [1-4].

However, there are no studies to date that could quantitatively show how to achieve the optimal operation conditions to generate the small gas bubbles in the range of less than 1mm in liquid steel refinement processes. Therefore, the objective of this research is to perform a quantitative analysis, using both water modeling experiments and computational fluid dynamics (CFD) simulations, in order to propose the optimal condition for obtaining the small bubbles in steelmaking tundishes.

Chapter 1: Literature Review

1.1 Introduction of inclusions

Steel is the most commonly used metal in the world. With technologies end usages progress, the requirement of steel cleanness level increases dramatically, namely the impurities such as sulfur, phosphorous, oxygen, nitrogen, carbon, hydrogen and oxide content (non-metallic inclusions) need to be removed as much as possible during the steelmaking processes. The cleanness level of steel is directly associated with the quantity, size distribution and morphology of the inclusions.

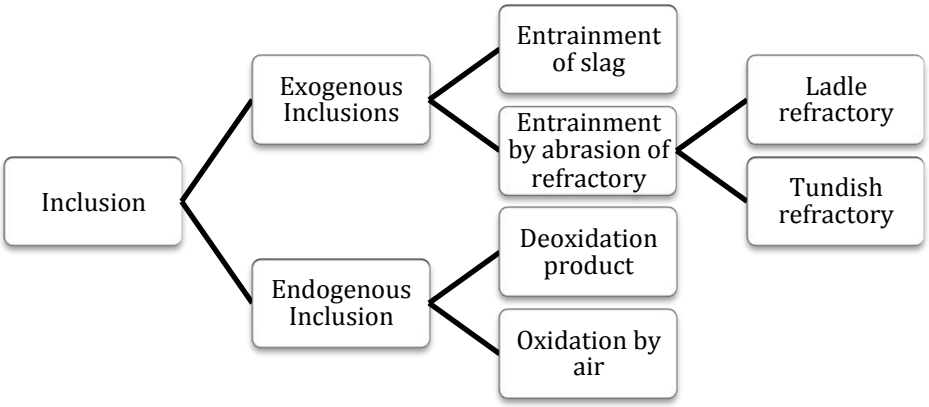

Figure 1 Possible sites for inclusion generation in a tundish [5]

Inclusions can be exogenous and endogenous as show in Figure 1. Exogenous inclusions can come from the slag entrapment and impurity particles from the refractories while endogenous inclusions are usually formed in the deoxidation reactions, typically in the secondary metallurgy processes [6]. The oxygen level is more than 500ppm at the end stage of a converter or the electric arc furnace (EAF). In order to achieve a target level of 2-4ppm dissolved oxygen, aluminum, silicon, calcium, and manganese are usually added. In this process, inclusions could be formed according to the reactions shown below:

$$2\underline{Al} + 3\underline{O} \rightarrow Al_2O_3\ (s)$$

$$\underline{Si} + 2\underline{O} \rightarrow SiO_2\ (s)$$

$$\underline{Ca} + \underline{O} \rightarrow CaO\ (s)$$

$$\underline{Mn} + \underline{O} \rightarrow MnO\ (s)$$

Inclusions in general are not favored in the steel making processes or in the final steel products. Inclusions (e.g. Al_2O_3 agglomerates) may stick to the submerged entry nozzle (SEN) and lead to a decreased casting velocity. In some cases, they may even clog the nozzles. Inclusions also act as stress raisers, and lower the mechanical properties of the final steel products, such as toughness, ductility, formability, welding properties, fatigue strength and corrosive resistance [7]. Figure 2 demonstrates the fatigue limit for different inclusion sizes at different strength levels. Clearly, the smaller the inclusions are, the higher is the fatigue limit, which means more durable steel products.

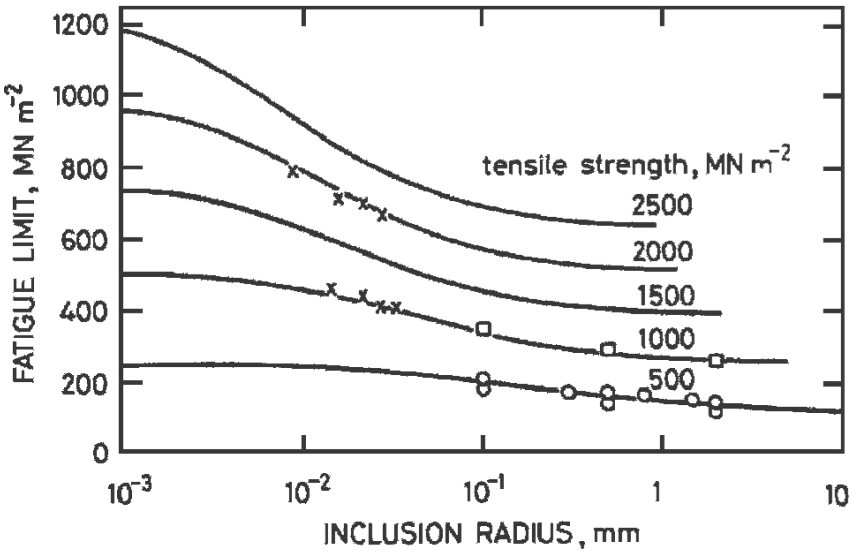

Figure 2 Fatigue limit for different inclusion sizes at different strength levels (Experimental data in dots; Prediction in curves) [8]

Industries have higher and higher requirements in the maximum size of inclusions acceptable in the final products, as shown in Table 1. Therefore in the processes of refining liquid metals, various methods have been implemented to remove inclusions, such as inert gas stirring, filtering, using ultrasonic and magnetic fields. In the later rolling treatment, some inclusions will break, while other inclusions will end up on the grain edges, which leads to surface silvers and blisters.

However, there is no available technology in steelmaking processes to effectively remove small inclusions (<50 μm). This is intrinsically due to the low rising speed of small inclusions, which is too low to float out by themselves. Small inclusions removal techniques, using ceramic filter, for example, which is widely used in the aluminum

refinement processes, cannot be utilized in the liquid steel due to technical difficulties and cost issues.

Steel Product	Maximum Inclusion Size
Automotive and deep-drawing sheet	100 μm
Drawn and ironed cans	20 μm
Line pipes	100 μm
Ball bearings	15 μm
Tire cord	10 μm
Wire	20 μm

Table 1 Maximum inclusion size in different steel products [9]

Bubbles serve as a promising candidate to remove the small inclusions in the liquid steel. Namely very fine gas bubbles will be introduced into the liquid metal system, to collide and attach with the small inclusions and to then float out to the slag surface together with attached small inclusions. Fine bubbles are chosen as they can provide large gas/liquid interfacial areas, and a high probability of small inclusions becomes attached.

1.2 Use bubbles to remove inclusions

Among the available inclusion removal techniques, gas stirring is the most popular method due to its low cost and simplicity of application. Gas stirring promotes good mixing and enhances the efficiency of the transfer of impurities. Inert gas, such as argon, is injected in the secondary steel refining processes. Examples include ladle argon gas treatment, RH vacuum degassing and gas injection via SEN. The gas injected typically perform three roles: to improve the homogeneity, to remove inclusions and to help prevent reoxidation and clogging [10].

The present research concentrated on the ability to remove inclusions by gas stirring. Gas stirring could enhance the removal of inclusions in two ways: first to help inclusions aggregate into larger inclusions; and second, bubbles will attach to small inclusions and float out.

One thing must be clearly understood before a study of the bubble and inclusion interactions is made. This is that big bubbles/inclusions, and small bubbles/inclusions, have different flow patterns and physical properties [11-13]. Sinha et al. [5] showed that

large inclusions (75-150μm) have large rising velocities and therefore would primarily float up to the slag surface or stick to the tundish wall if no turbulence is present. On the other hand, most of the small inclusions (<50μm) could not be removed by sticking to the walls or by floating out to the top slag layer due to their low rising velocity.

Several studies [2, 3, 14-16] showed that small particles that are not wetted by the liquid could attach to the bubbles to float out to the top surface. As shown in Figure 3, the following steps are suggested to describe particle and bubble interactions, based on aqueous experiments: 1, bubble approaches inclusion; 2, formation of a thin liquid film between the inclusion and the bubble; 3, oscillation or sliding of inclusion on the bubble surface; 4, drainage and rupture of the liquid film; 5 stabilization of bubble/inclusions aggregates; 6, flotation of bubble/inclusion aggregates.

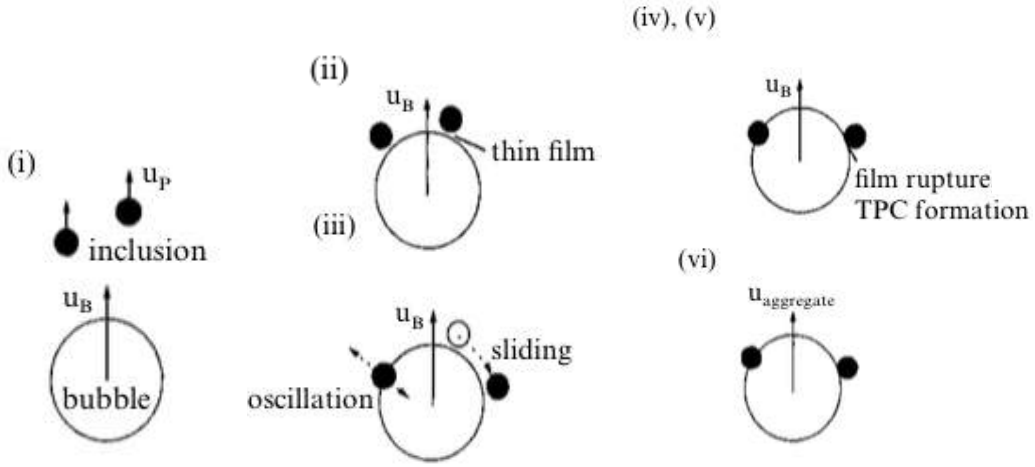

Figure 3 Inclusion flotation process divided into sub-processes [17]

Various factors can influence the performance of an inclusions removal by a gas bubble. These factors include liquid flow rate, inclusion size and properties, bubble size and velocity. Wang et al. [2, 3] studied collision, attachment and de-attachment phenomena, considering the "time" required to complete each step: if the time for rupture of the liquid film between bubbles (corresponding to bubble coalescence) is less than the time required to establish bubble/inclusions aggregation, then the inclusion particle will be floated out to the surface. However, this static aqueous based single bubble analysis most likely will no longer be valid in a liquid steel system where complex turbulent conditions are usually present with a large amount of bubbles interactions.

The overall inclusion removal performance in general depends on three interactions: inclusion and bubble collision, inclusion and bubble adhesion, inclusion and bubble detachment [10]. Therefore the overall inclusion removal probability can be measured by Equation (1), where P_{total} is the total probability of the inclusion removal, P_c is the probability of inclusion and bubble collision, P_a is the probability of inclusion and bubble adhesion and P_{de-a} is the probability of inclusion detach from the bubbles.

$$P_{total} = P_c \times P_a \times (1 - P_{de-a}) \quad (1)$$

Several simplifications could be made about P_{de-a} and P_a. For small inclusions already attached to bubbles, the detachment probability (P_{de-a}) can be neglected according to Yoon et al. [18]. Based on this simplification, Zhu et al. [1] showed from water modelling that the removal of inclusions in the range of 20-50μm from molten steel involves three stages: contact, adhesion and flotation. The mechanism is presented in Figure 4. The same study also showed that bubbles in the range of 1-2mm could improve the efficiency of small inclusions removal.

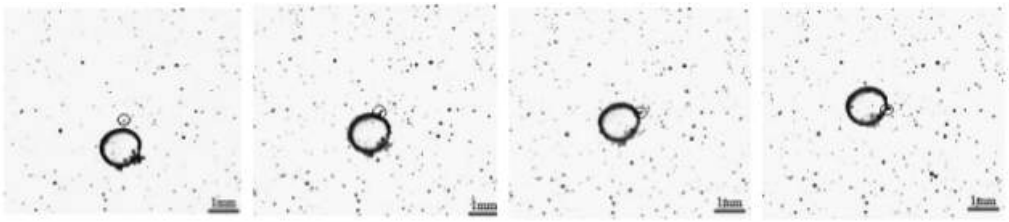

Figure 4 Particle approach a bubble, then adhesion and float with the bubble[1]

P_a is primarily determined by the contact angle between the particle and the liquid. Zheng et al. [19] showed that the adhesion probability is close to 100% when the contact angle is more than 90^o. Inclusions from molten steel such as Al_2O_3 and SiO_2 have contact angle with liquid steel of 144^o and 117^o respectively. Other studies [2-4] further stated that the adhesion probability also depends on the inclusion size. Inclusions less than 50μm have P_a more than 95%. The inclusions of interest in this research are the non-metallic inclusions less than 50μm. Therefore the P_a can be generally assumed to be 100%.

To this point, it is clear that the total removal efficiency of small inclusions by bubble flotation is dominated by P_c, the collision probability between bubbles and inclusions. Yoon and Luttrell [18] showed that the collision efficiency between inclusions and bubbles varies as the square of the particle size (D_p) and inversely as the square of

the bubble size (D_b). The bigger inclusions and smaller the bubbles, the easier it will be for them to collide. The collision probability is shown in Equation (2).

$$P_c = \left[\frac{3}{2} + \frac{4Re^{0.72}}{15}\right]\left(\frac{D_p}{D_b}\right)^2 \quad (2)$$

Several studies [1-4] confirmed experimentally that the collision probability increases with a decrease in bubble size and an increase in inclusion size. Therefore, for the removal of small inclusions, where D_p is less than 50μm, small bubbles (0.25-3mm) are required to achieve a high collision probability between bubbles and inclusions.

1.3 Bubble formation mechanism

Sections 1.1 and 1.2 showed that small bubbles are required to remove small inclusions in the liquid steel. These small bubbles however, are very hard to be produced in liquid steel using nozzles, owning to the high surface tension of liquid steel and the non-wetting properties between the nozzle and the liquid steel. Typical injection methods such as tuyeres, lances and porous plugs will generate bubbles with diameter of 10 to 40mm.

1.3.1Bubble formation regimes in liquid metal

Gas is typically injected into the liquid steel through submerged nozzles or orifices. Bubble formation in the liquid steel can be categorized into three regimes according to the air inflow rate: the surface tension regime, the inertial flow regime, and the jetting regimes [20, 21].

Static Regime:

The static regime occurs when the gas inflow rate is very low. Therefore the acceleration of liquid due to the release of bubble can be neglected. For a wetting system, the bubble size is purely determined by the balance between the buoyancy force of the bubble and the surface tension forces holding the bubble to the inner diameter of the nozzle [22, 23]. Hence the volume of the bubble generated in a wetting system, $V_{b\text{-}wet}$, can be calculated by Equation (3).

$$V_{b-wet} = \frac{\pi D_{ni}\sigma}{\rho g} \quad (3)$$

Where $V_{b\text{-}wet}$ is the bubble volume in a wetting system, D_{ni} is the inner diameter of the submerged nozzle, σ is the liquid surface tension and ρ is the liquid density.

However, liquid steel is a non-wetting system, in which the gas injected will attach to the non-wetting ceramic nozzle surface. Hence, bubbles will form at the outer circumference of the nozzle. A comparison of the bubble formation in a wetting and non-wetting system is shown in Figure 5.

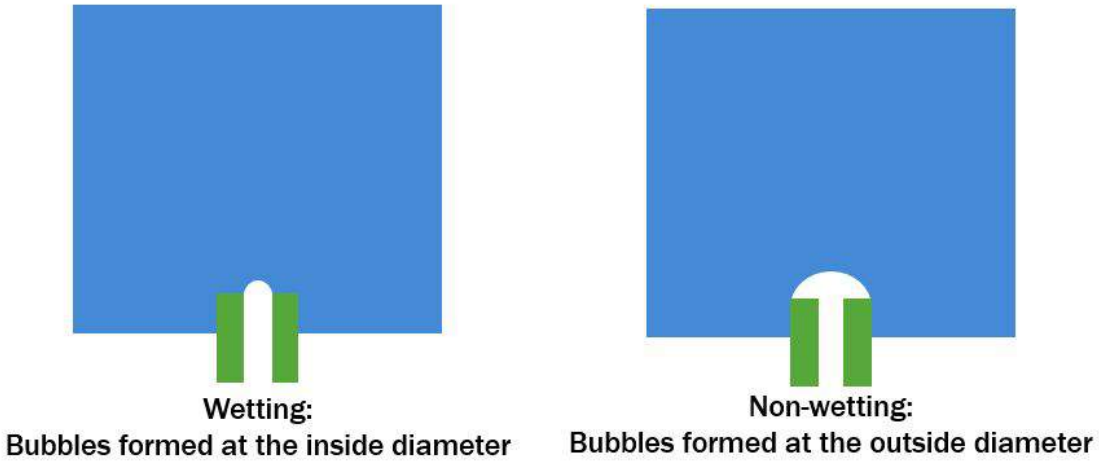

Figure 5 Bubble formation in wetting and non-wetting system: bubbles tend to form at the inner diameter of the nozzle in wetting system and at the outer diameter in non-wetting system [24].

The volume of a bubble generated in a non-wetting system can be calculated by Equation (4).

$$V_{b-nonwet} = \frac{\pi D_{no} \sigma}{\rho g} \quad (4)$$

Where $V_{b\text{-}nonwet}$ is the bubble volume in a non-wetting system, D_{no} is the outer diameter of the submerged nozzle, σ is the liquid metal surface tension and ρ is the liquid metal density.

In the static regime, according to Equation (3) and (4), the size of bubbles forming remains constant, even with increasing gas flowrate through a nozzle. Only the bubble formation frequency increases with the gas inflow rate. Therefore the static regime is also known as the ‘constant volume regime’. Bubbles formed are approximately spherical in shape [25]. The bubble formation frequency is low and typically less than 100 bubbles per minute. [26].

Experimental results from water modelling tests (wetting system) [20, 27-29] confirmed that when the gas flow rate is low, the size of the bubble is determined by the nozzle inner diameter. The properties of the gas injected and the viscosity of the liquid have no significant impact on the size of bubble generated, especially for liquids with low viscosity [26]. Experimental results from liquid metals tests confirmed that the outer diameter of the nozzle is a dominant factor in controlling the bubble size, for nozzle Reynolds numbers below 500 [30].

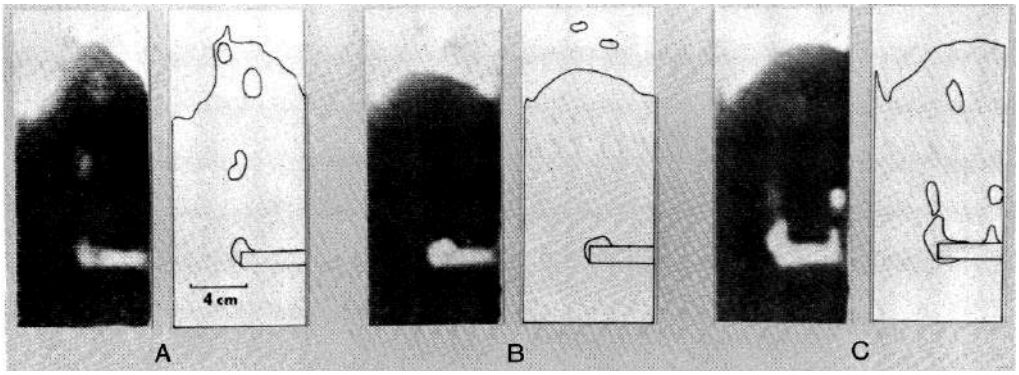

Figure 6 (A)buble formation at the outer diameter at the nozzle, idea case; (B) bubble form on the top of the nozzle; (C) bubble move back to attach to the nozzle [22]

Figure 6 shows various bubble and nozzle attachment from X-ray images of liquid Indium-Gallium alloy (a non-wetting system) [22]. In current pyro-metallurgical operations, it is still very challenging to obtain small bubble plumes.

Dynamic Regime:

With increasing gas flow rates, (e.g. 1-1000 cc/sec), both bubble volume and the frequency of formation begin to change. The frequency of formation will eventually reach a maximum, as suggested by study [20], and after that, only the bubble volume increases with increasing flow rates, while the frequency of formation practically remains constant at about 10-15 bubbles/second for regular nozzles [26]. Hence it is also referred as "constant frequency regime". By using Newton's Law, Iron and Guthrie [24] showed experimentally, that the bubble volumes in aqueous systems could be predicted as:

$$V_b = 1.378\, Q^{1.2} g^{-0.6} \quad (5)$$

Where V_b is the bubble volume, Q is the gas flow rate and g is the gravity.

Equation (5) confirms that the bubble volume, in the range of middle to high gas flow-rates range, is almost linearly proportional to gas flow-rate. Studies [27, 31]

suggested that in this regime the buoyancy force is balanced against the force required to accelerate the liquid from the expanding gas-liquid interface. Experimental results from water modeling are in excellent agreement with the theory [32, 33].

With further increases in gas velocity, more circulation and turbulence are expected [25]. Due to the complex dynamic forces involved in this regime, the bubbles are very easily distorted, primarily in four ways [20, 34] : pairing bubbling, double bubbling, delayed release, and bubble coalescence after release. The first three mechanisms are due to the fluctuations brought about by the release of the preceding bubble, while the last one is an intrinsic gas bubble characteristic. Figure 7 shows the pairing bubbling and double bubbling mechanisms. In pairing bubbling, a small bubble is formed immediately after the first bubble releases, due to residual pressure. In double bubbling, two similarly sized bubbles are formed, in sequence, due to reduced static liquid pressure.

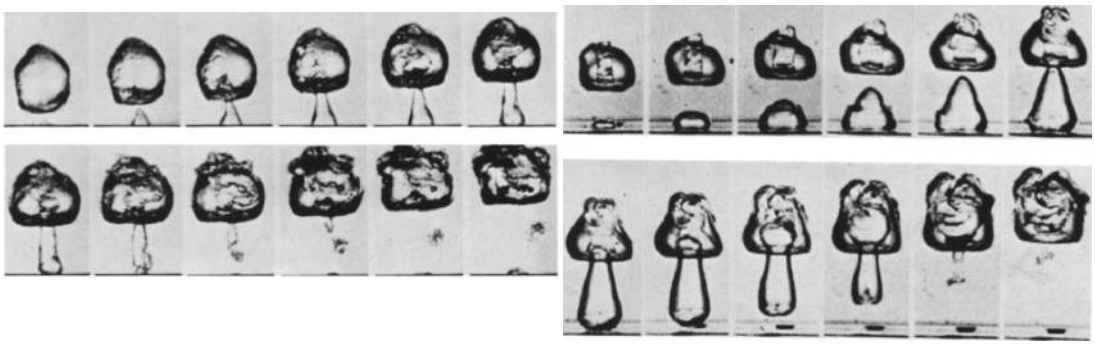

(a) (b)

Figure 7 (a) Pairing bubbling due to residual pressure in the gas chamber upstream, (b) Double bubbling due to reduced pressure in the wake of the first bubble [20]

These bubble distortions preclude accurate predictions of bubble sizes. It also limits the precision of experimental results. Studies [28, 30, 34, 35] based on water modeling and non-wetted nozzles in liquid metal experiments, lead to an empirical correlation for predicting bubble sizes in liquid metals:

$$V_b = 0.083\, Q^{0.867} {D_{no}}^{0.435} \quad (6)$$

where V_b is the bubble volume, Q is the gas flow rate and D_{no} is the outer diameter of the submerged nozzle.

Equation (6) indicates that at intermediate gas flow rates in a non-wetting system such as a liquid metal in contact with an oxide refractory, the frequency of bubble formation is approximately constant, and its size depends on the gas flow rate and the outer diameter of the injection nozzle.

Turbulent Jetting Regime:

The turbulent jetting regime occurs at high gas flow rates, where irregular bubbles rise in a swirling motion. This regime is featured by two characteristics: first, bubbles experiencing extensive coalescence right after release to form very big bubbles; and second, these large bubbles generally tend to shatter into smaller bubbles of various sizes, due to the turbulent created from the high flow rate, just a short distance away from the nozzles or orifices [20, 28]. At higher flow rates, the bubbles are no longer formed at the nozzle, instead, a continuous jet of gas was observed at the end of the nozzle. As such, it is known as the "jetting zone" [29].

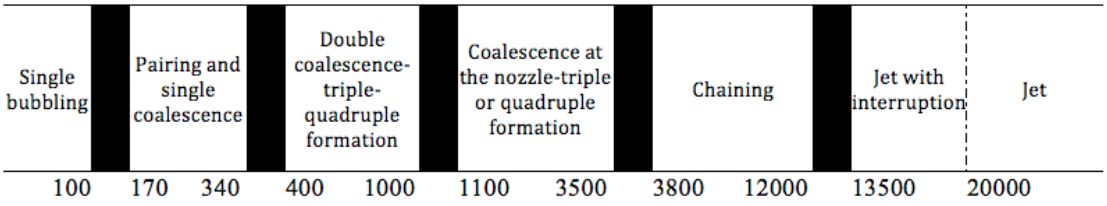

Figure 8 Different regimes of bubbling behavior in liquids based on Reynolds Number[36]

It was experimentally found from studies [37, 38] that the critical value for the transaction from bubbling to jetting is a little bit higher than, but very close to, the sonic velocity, regardless of nozzle size, while other study [36] summarized the transition of different regimes based on Re number, as shown in Figure 8. It worth noticing that the transition to jetting is gradual, such that more and more jetting is observed and less and less bubbling is seen, with increasing speed of gas injection. The present research is interested in how to consistently create small bubbles in liquid metals; as such, the jetting regime is outside the scope of this study.

1.3.2 Small bubble formation in turbulent conditions

Turbulence in a flow system can exert shear forces on any gas bubbles existing within the liquid. There is a maximum bubble size (also called critical bubble size) for a given level of turbulence. If the bubbles go above the maximum bubble size, the resulting shear forces will break up the large bubbles towards the maximum or critical bubble size. The details of the mechanism of bubble break up under turbulent conditions can be found in Section 4.10 of this thesis. Several critical bubble size models [39-41] have been proposed by previous research works as shown in Table 2.

Researchers	Equation
Sevik and Park [39]	$D_{b-max} = We_{cr}\left(\frac{\sigma\times10^{3}}{\rho\times10^{-3}}\right)^{0.6}(\varepsilon\times10)^{-0.4}\times10^{-2}$
Schulze [40]	$D_{b-max} = \left(\frac{2.11\times\sigma\times10^{3}}{\rho\times10^{-3}\times(\varepsilon\times10^{4})^{0.66}}\right)\times10^{-2}$
Evans et al. [41]	$D_{b-max} = \left(\frac{We_{cr}\sigma\times10^{3}}{2(\rho\times10^{-3})^{1/3}}\right)^{0.6}(\varepsilon\times10)^{-0.4}\times10^{-2}$

Table 2 Maximum bubble sizes under turbulence conditions. [39-41]

The maximum bubble size under turbulent conditions is determined by the critical Weber number (We_{cr}), liquid density(ρ), surface tension(σ) and turbulence energy dissipation rate(ε). All models suggest that the stronger the turbulent field, the smaller is the critical or maximum bubble size.

Martínez-Bazán et al. [42, 43] studied, experimentally, the transient evolution of bubble size distribution resulting from bubble break up in a fully developed turbulent water flow. The experimental results showed that the final bubble size distribution depends on the critical bubble size and initial bubble size.

Tang et al. [44] performed mathematical modelling, based on Sevik's equation [39], and showed that small bubbles (1-3mm in diameter) could be generated under turbulent conditions that are already available in the current steelmaking ladle and tundish system. However, Tang's mathematical modelling is only capable of calculating the average turbulence energy dissipation rate in the ladle shroud, which is not sufficient. As shown later in Chapter 4, the local turbulence dissipation energy is the dominant factor in creating small bubbles.

Arai et al. [45] and [46] performed water modelling experiments to study the rate of inclusion removal in the turbulent conditions by using an impeller-stirred vessel. However, this result is not consistent with those of other researchers: the small inclusions removal rate decreased with the increase in turbulence energy dissipation rate (smaller bubble size). This discrepancy most likely was due to the impeller-stirring induced turbulent flow, which contains strong rotational forces.

Due to the bubbles generated in turbulent conditions are usually small. Therefore, the shape of these bubbles can be approximately considered spherical as shown in Figure 9, which could validate the assumption of spherical bubbles when performing CFD simulations.

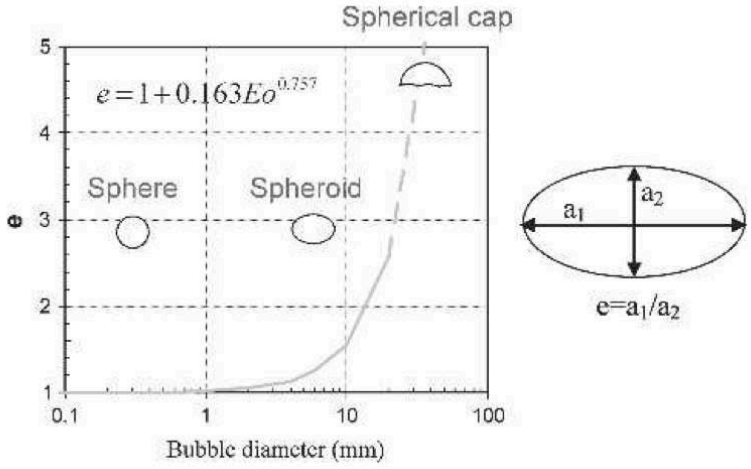

Figure 9 Bubble shape with diameter [47]

1.4 Tundish bottom blowing

1.4.1 Basic concept

It has been shown that small inclusions (<50μm) can be removed by using fine bubbles (0.25-3mm).

Now the question become to where and how to introduce these bubbles into the steelmaking process. One method is to inject inert gas at the bottom of the tundish, which is the final liquid metal reservoir before casting starts. The basic idea of bottom blowing is shown in Figure 10. Bubble generating devices (porous plugs, porous bricks or lances) are placed in the bottom of the tundish. Then the flow of steel with inclusions will pass through the bubbling region, where bubbles pick up inclusions.

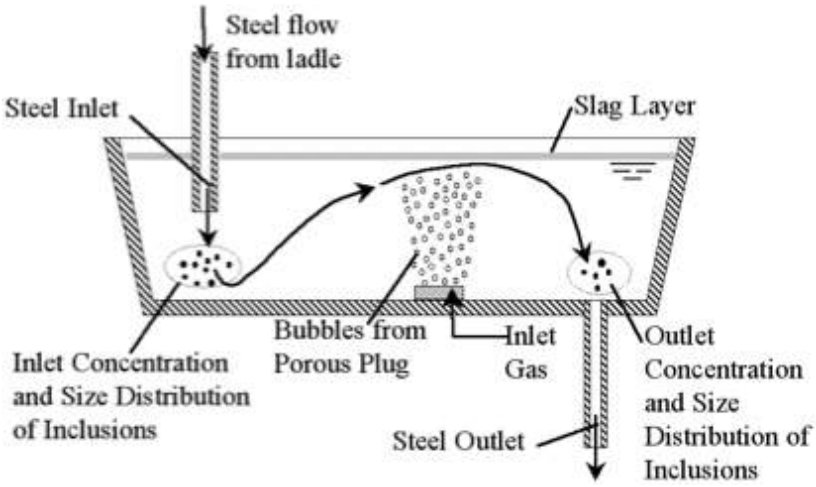

Figure 10 The basic idea of bottom blowing is shown as above [48, 49]

In general, the bottom blowing method can improve steelmaking process in three ways: first, the bubbles will form a bubble curtain and enhance the flow pattern in the tundish; second, the bubbles will help inclusions aggregate; third, the fine bubbles will help small inclusions float out as previous discussed.

1.4.2 Flow pattern enhancement

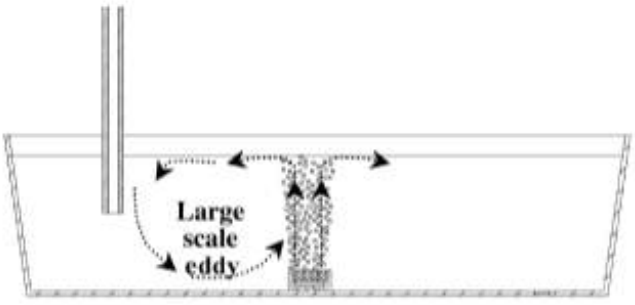

Figure 11 Flow enhancement from bottom blowing from tundish [48, 49]

Several studies [50-56] showed that bottom blowing from tundish could enhance the flow pattern for a better mixing, especially if proper impact pads were used to modify the flow. This is generally due to the eddy created from the bubbles plumes. Zhang et al. [52] performed a mathematical simulation on bottom blowing in a tundish in liquid steel and reported that gas bubbles could enhance recirculation in tundish and promote mixing and reduce dead zone. They also showed that the flow rate of gas has significant effects on the flow pattern, too large a flow rate will create vortex near the slag and cause undesired slag entrapment. On the other hand, if the flow rate is too small, the flow curtain cannot form and improvement from the bottom blowing is not that significant and bubbles may enter the SEN. Meijie Z. et al. [51] showed that by using the bottom blowing method (porous plug), the RTD is longer and less dead zone would be expected. By using PIV and CFD, Vargas-Zamora and Morales [53] [54] studied the flow pattern from bottom blowing and found out that under isothermal conditions, a gas curtain promotes a fluid flow by large eddies and promotes homogenization. Donghui Li et al. [55, 56] performed mathematical simulations and discovered that gas injection from the bottom could improve flow homogeneity and increase the rate of removal of inclusions. The impact pad and filter dam have minimum effects on the distribution of the gas in the liquid. However, the more gas that was injected, the more likely was the liquid surface to fluctuate. Therefore, it is crucial to control the amount of gas injection to avoid slag entrainment. Feng et al. [57] also did an RTD study and found out that collision probability is increased if the porous plug is located within the injection flow area, as shown in Figure 12.

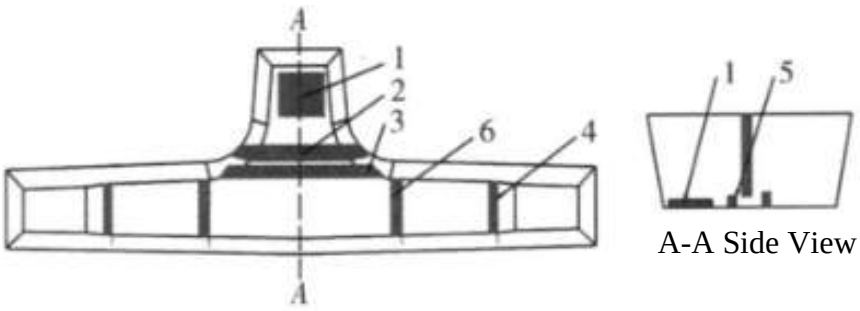

Figure 12 Tundish constitution and schematic diagram of gas purging sites 1- Impact Pad; 2-Inclusions filter; 3-Big block dam; 4-Small block dam; 5,6-Porous bricks [57]

1.4.3 Inclusions removal performance by bottom blowing

Arcos-Gutierrez [50] performed a purely mathematical simulation of the bottom blowing approach based on the models proposed by Wang [3]. Together with several other studies [48, 49] , it was theoretically shown that fine bubbles are required for removal efficiency to be acceptable. Particularly for small inclusions less than 60µm, less than 3mm bubble is required to achieve a removal efficiency above 80%.

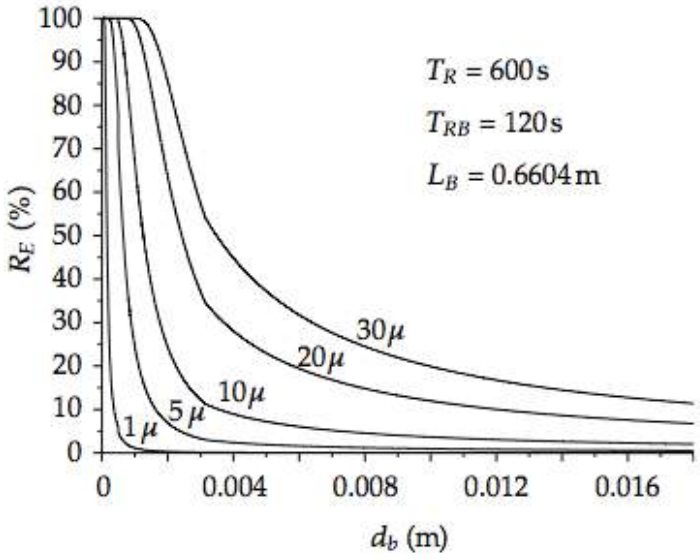

Figure 13 Removal rate (R_E) with different bubble sizes and inclusion sizes [50]

Meijie Z. et al. [51] did the only liquid steel experiment in industrial practice in a 30t tundish at Lai Wu Iron & Steel Ltd., China with argon blowing from the tundish bottom as shown in Figure 14. It was found that average inclusions of less than 20µm decreases more than 24% and average overall oxygen content decreases about 15% with controlled blowing parameter. Porous plugs were used at the bottom of the tundish.

However, the study did not report the actual bubble size in the tundish. The bubble coalescence effects were neglected as well. The trajectory of flows and bubble entrapment were not discussed. Despite all the limitations of the study, it showed that even without a full understanding, bubbles can still improve the steel cleanness level.

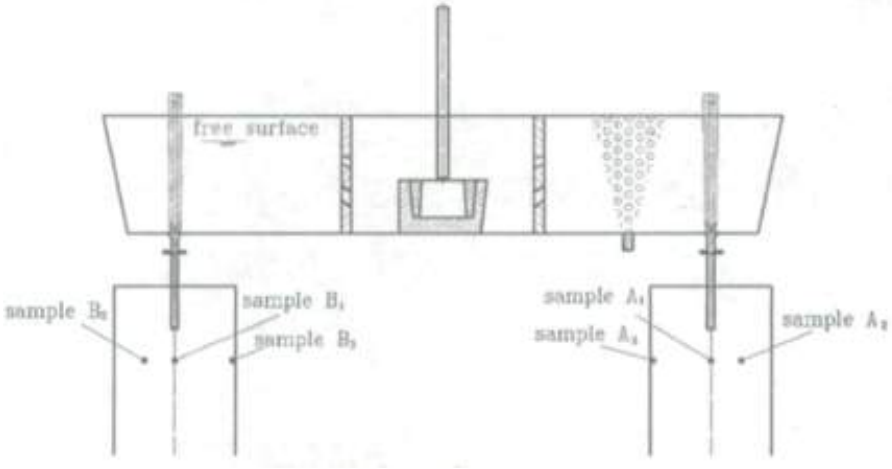

Figure 14 Experimental set-up for a liquid steel experiment [51]

1.4.4 Concerns regarding the bottom blowing method

There are three main concerns about the bottom blowing method are: how to generate fine bubbles, the proper flow rate of gas, and the rising speed of bubbles.

The most important factor is about generating fine bubbles. As discussed in Equation (2), the bubbles need to be below 3mm to pick up small inclusions. All the experiments were performed in water with a porous plug, which is only capable of generating small bubbles in water, not liquid metals. It was shown previously that the most promising way to generate such bubbles in liquid metal is to use turbulent shearing forces. However, none of the current studies about bottom blowing successfully utilize the turbulence from the jetting.

The second concern is about the flow rate of the inert gas issuing from the nozzle. In order to avoid clogging and attacks from liquid steel to the nozzle, blow speed used in steelmaking is super-sonic. However, this apparently would not work in the tundish, as the high-speed flow rate of injected gas will break the slag, create a slag eye, and cause slag emulsification [55, 56]. Not even to mention the high flow rate will lead to massive bubble coalescence, which loses the whole point of removing the tiny inclusions by using fine bubbles.

The third concern is about the rising speed of the bubbles, if the bubbles do not have sufficient rising velocity they might enter the SEN. Bao et al. [58] carried out a bubble terminal velocity calculation and showed that bubbles with 1.5-3mm size has rising velocity of 0.05 to 0.6m/s, which is sufficient large to float out in a 0.8m tundish within its residence time (5min). Other studies [50, 52-54] state that fine bubbles have a bigger likelihood to enter the SEN.

1.5 Ladle shroud gas injection

1.5.1 Basic concept

The basic idea here is to inject gas at the ladle shroud, where metal flow-speeds are high (1-3m/s) and turbulence is assumed to be fully developed. The turbulent flow will break up the gas into finer gas bubbles. These fine bubbles, dispersed in the highly turbulent flow, have a high probability of colliding with inclusions. The schematic approach is presented in Figure 15.

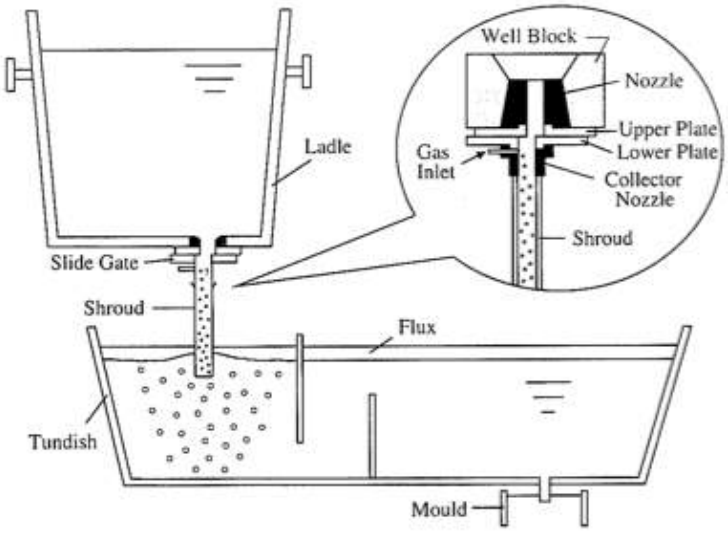

Figure 15 Schematic representation of gas injection at ladle shroud [2]

Compared with the bottom-bubbling method, the implementation of this idea to the system of steelmaking would require a minimum modification to the status quo; similarly it is more likely to generate fine bubbles consistently.

In 2005 Wang et al. [59] performed a mathematical simulation to exam the inclusion removal by injecting gas at the ladle shroud. The mathematical prediction used the previously determined relationship by Wang et al. [2, 3]. In this model all three removal methods are included: the simple Stokes flotation, wall adhesion and bubble adhesion.

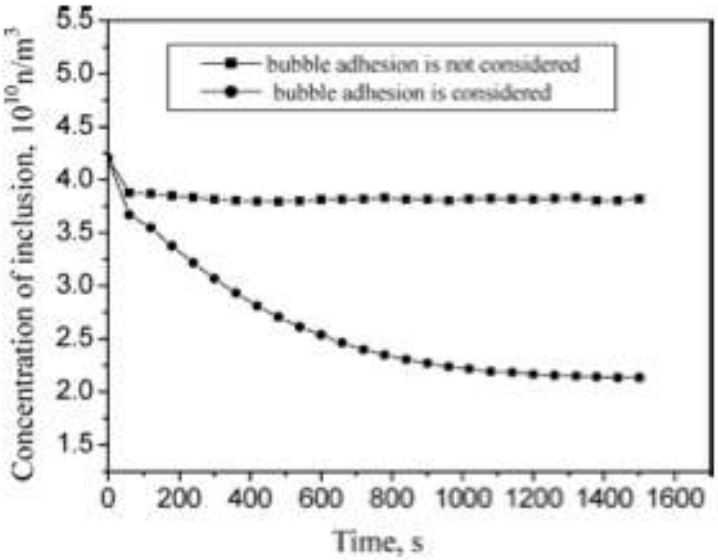

Figure 16 Inclusion concentration with and without bubble adhesion consideration [59]

Figure 16 shows that the inclusion adhesion to rising bubble surface leads to a significant improvement than only Stokes floatation and wall adhesion mechanisms. Bubble size is the key factor in determining the performance of adhesion to small inclusions. The study also stated that when the bubble reaches 5mm or more, the removal efficiency of small inclusions is very low and in reality, the coarse bubble adhesion effects are practically negligible.

1.5.2 Slide gate opening ratio, nozzle position and bubble sizes

In practice, the slide gate changes from small to large openings in order to maintain a steady flow rate of the molten steel. Tang et al. [44] studied the formation mechanism of fine bubbles in the shroud nozzle of a ladle. Based on Sevik's equation shown in Table 2. The results are presented in Figure 17.

The study shows that by using turbulent field already existed in ladle shroud, it is possible to create fine bubbles less than 3mm in diameter. The results show that the flow

rate, surface tension and the slide gate opening affect the bubble size. The study also performed a simple pressure prediction along the shroud. Both predictions are fairly close to its experimental results.

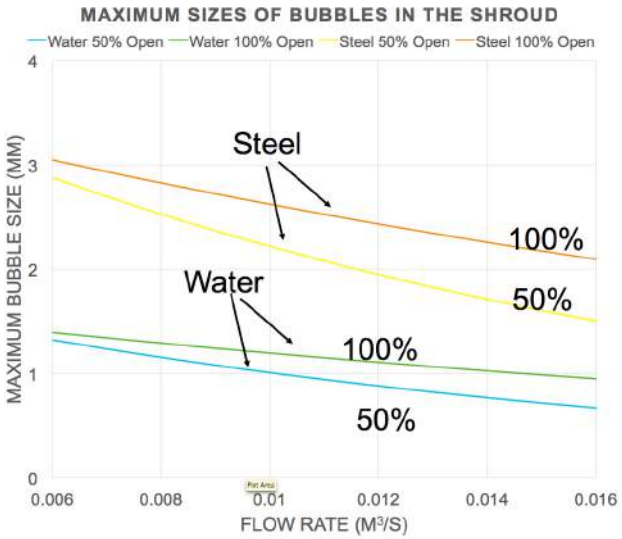

Figure 17 Maximum bubble size prediction with different liquid flow rate and slide gate opening [44]

Cho and Lee [60] studied bubble generation using ladle shroud gas injection with different nozzle positions and slide gate opening ratios and different air/water ratios using the experimental set-up shown in Figure 18. The flow rate of water was controlled in the range of 2-3.2m^3/h, which is equivalent to 1.77 to 2.83m/s in flow speed. The air/water ratio is 0-12%. The gate opening was from 0-100%.

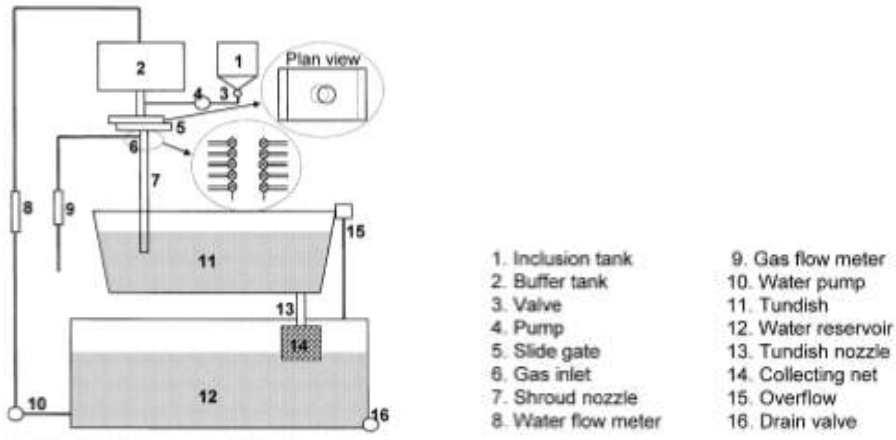

Figure 18 Experimental set-up by Cho[60] to study the bubble formation mechanism with different nozzle position and slide gate opening ratio

Cho and Lee found that there was a decrease in turbulence with a increase in the slide gate opening, and also down along the ladle shroud. This is due to the flow speed decrease with slide gate opening and along the shroud. For fluid flow with a mean velocity of 2.5m/s at the end of the ladle shroud, the speed at the slide gate could go to as high as 8m/s. Therefore less slide gate opening and close to the slide gate can help generate finer bubbles and improve mixing efficiency. In their study they also showed that the wettability dominates the inclusion removal efficiency.

Figure 19 shows the photos of bubble formation with a constant flow rate of liquid, constant gas/water ratio at gas injection port#1, with different slide gate opening ratios. It is clear that more bubbles are formed (hence finer bubbles due to the gas injection rate was fixed) when the slide gate-opening ratio is low. At gate opening ratio of 37%, the ladle shroud was filled with fine bubbles. Cho stated the bubbles are less than 0.5mm in this case. When the gate opening increased to 78%, the bubbles formed were obviously bigger and the quantity of bubbles decreased dramatically as well.

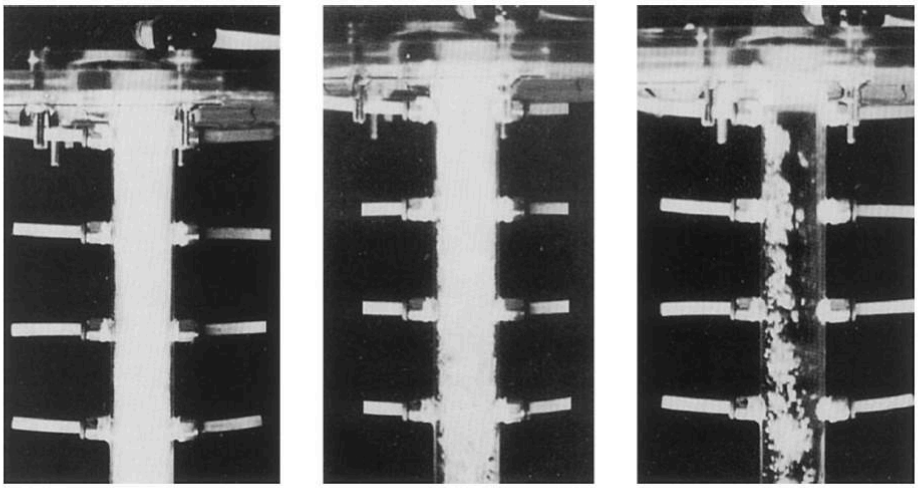

Figure 19 Effect of slide gate opening on bubble formation and mixing behavior of the gas and liquid phases (water flow rate = 3.2m^3/h, gas/water ratio=10%, gas injection port=#1) [60]

Figure 20 shows the effects of nozzle positions. Due to the flow speed gradually decreases along the ladle shroud, the lower position the gas was injected, the less turbulence there is to break the gas into fine bubbles. As shown from the figure that at constant water flow rate, gas/water ratio and slide gate opening, port #1 gave the largest amount and the finest bubbles.

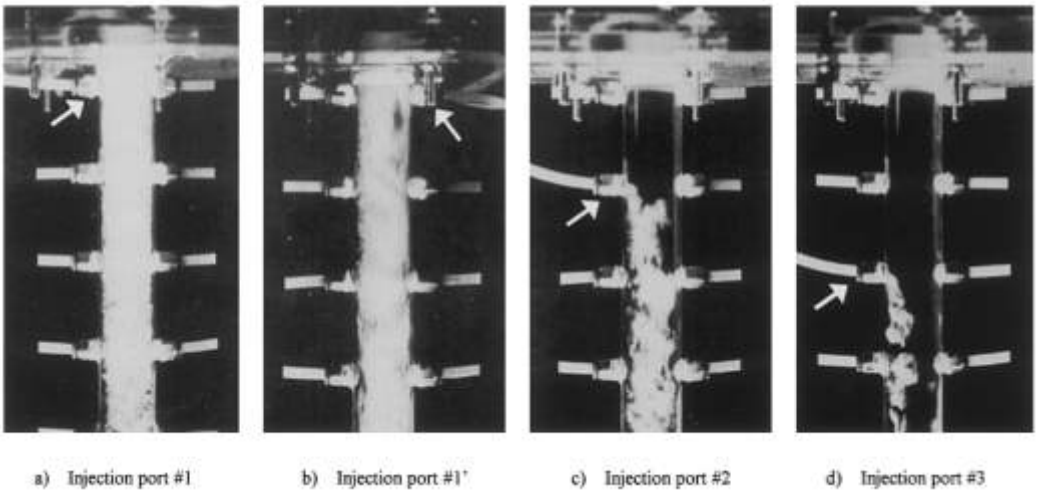

Figure 20 Effect of injection position on bubble formation and mixing behavior of the gas and liquid phases (water flow rate = 3.2m^3/h, gas/water ratio=10%, slide gate opening = 58%)[60]

Li et al. [61] used a similar set up and found that low flow rate of gas could generate fine bubbles and enhance inclusion removal rate. Figure 21 shows that at liquid flow rate controlled at 3m^3/h, bubbles less than 1mm are formed with low gas injection rate (0.3L/min). When the gas injection rate increases to 1.5L/min; the bubbles are in the range of 3-5mm. The study showed that gas injection rate of 0.6L/min gave best inclusion removal rate.

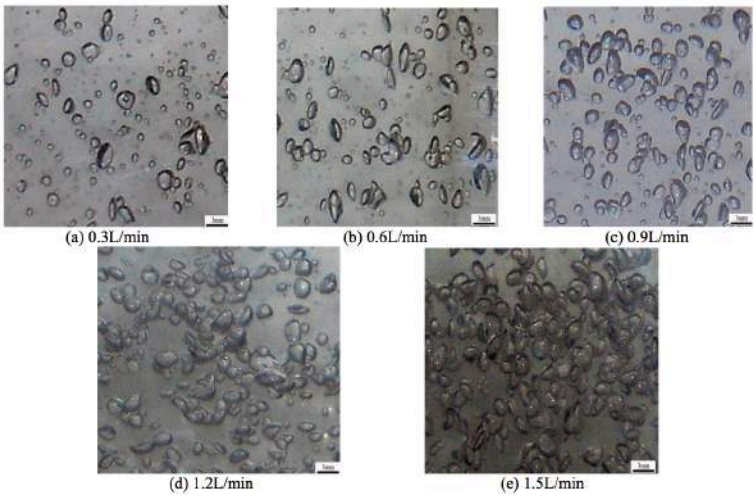

Figure 21 Bubble size decrease with decrease gas flow rate [61]

Li et al. concluded that increase the gas injection rate first facilitates bubble generation and helps improve the inclusion removal. However, further increase the gas injection flow will lead to fewer contacts between inclusions and bubbles.

Wang et al. [3] performed water simulation study with the water flow rate from 0.0006 to 0.012m^3/s, identical to the flow rate of ladle teeming into a two strand caster with slab size 1.6m by 0.5m and casting speed of 1.2m/min. They found that with high flow rates (more turbulence), the bubble created from the shroud pipe is estimated as less than 0.5mm.

Zhang et al. [62] from Beijing in 2006 showed that fine bubbles in diameter of 0.3-0.5mm can be generated in the shroud. The fluid velocity decreases with distance from slide gate. Turbulence reaches maximum just under the slide gate. When the gas injection rate is too high cavitation is reported. The flow rate effects and nozzle sizes on the bubble sizes were briefly discussed, namely the less flow rate and less nozzle size, the smaller bubbles are observed. The author summarized that optimum operation condition is 0.3mm nozzle size with 0.08L/min gas flow rate. According to their set-up, the bubble size was between 0.3-0.5mm. The bubbles are very small, therefore a low quantity of gas can generate a lot of bubbles.

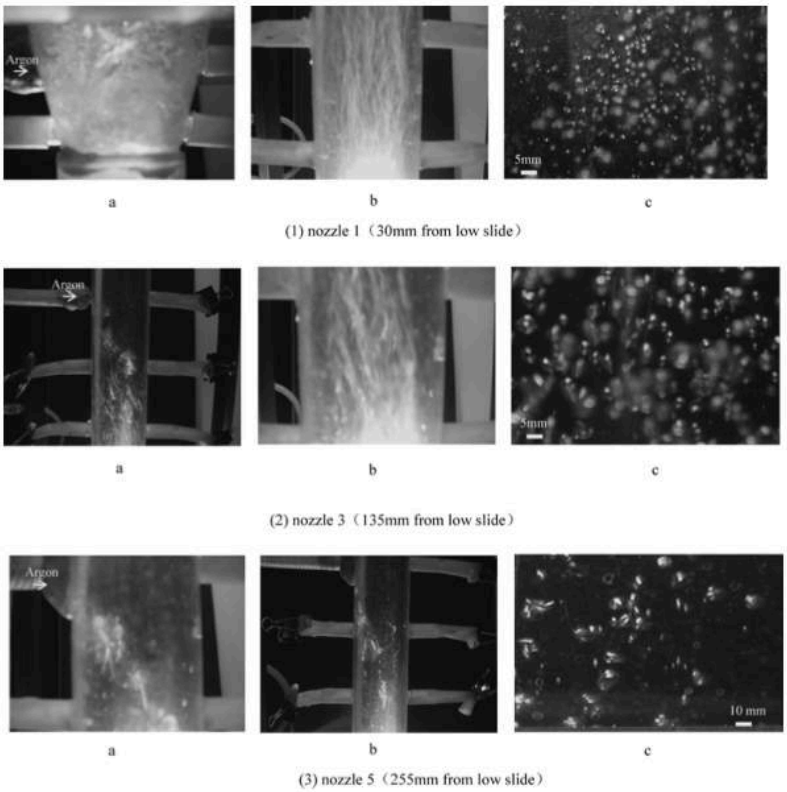

Figure 22 Bubble size increases along the ladle shroud by Zhang et al. [62]

In a study by Zhu et al. [1], bubbles down to 1mm were observed. However, the bubble size distribution was not reported. The exact location for bubble observing was also not reported. The work was aimed at studying single bubble and inclusion particle interaction.

1.5.3 Flow patterns and bubble trajectories

Chattopadhyay et al. [13, 63] performed a detailed study of inert gas shrouded ladle nozzles and their role on slag behavior and fluid flow patterns within the tundish. The key finding from the study was that bubbles in the size range 100-500µm, will follow the liquid flow and will spread out within the tundish instead of forming a rising bubble column. When such bubbles are dispersed throughout the tundish, it will provide a higher probability of bubble and inclusion collisions [63]. Too high s gas flow rate will lead to exposed eye on the slag in the tundish, which will cause more reoxidation. For inclusion removal purposes, an optimum amount is 6% gas by volume.

Li et al. [61] found that the depth of penetration of the bubble column is inversely related to the flow rate, the results are shown in Figure 23.

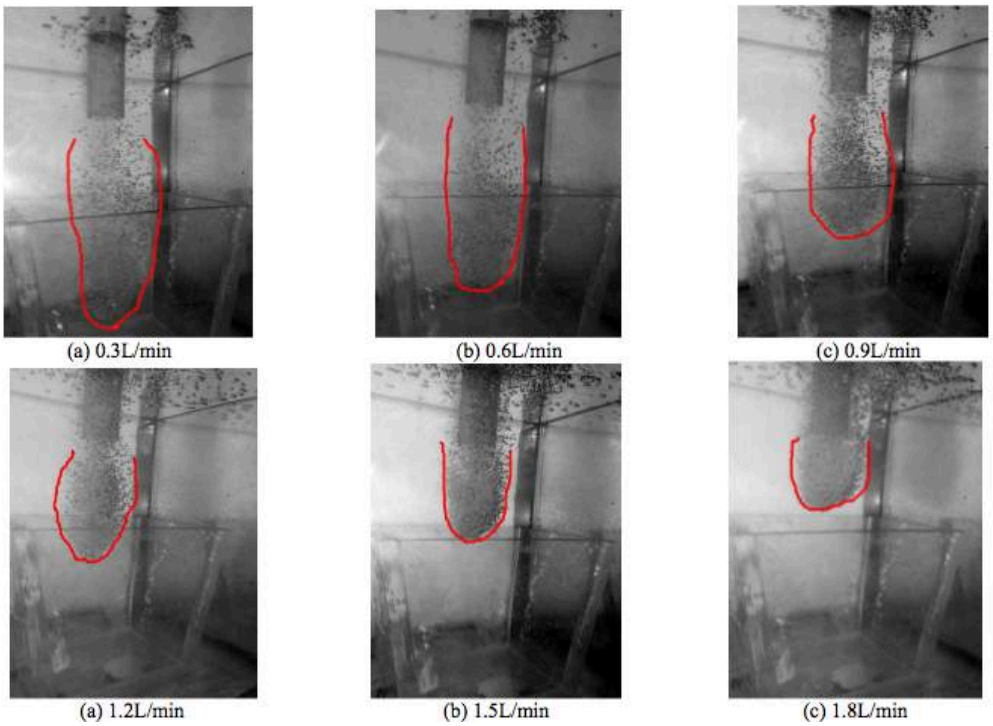

Figure 23 Gas injection through ladle shroud: Flow rate and depth of penetration [61]

This is in agreement with other studies [13, 63], whose results are shown in Figure 24. At low flow rates and low air/water ratios, the depth of penetration and quantity of bubbles increase with gas injection flow rate. However, when the flow rate or the air/water ratio goes too high, bubbles coalesce to form large bubbles and the penetration depth decreases accordingly.

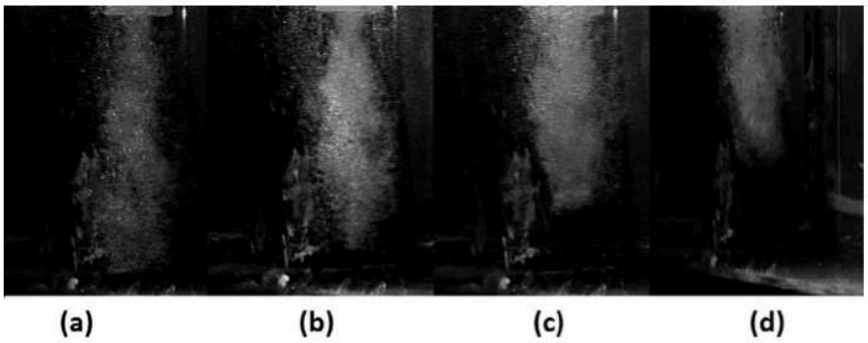

Figure 24 Bubble plume in the full scale water model for gas injection at (a) 4% (b) 6% (c) 8% (d) 19% of water entry flows [13]

Zheng et al. [19] showed that the when the aggregate particle /bubble were discharged into the bottom tank where an abrupt change occurred in their relative movements, large particles were detached from the bubbles due to high inertia force, whereas the small particles kept sticking with bubbles.

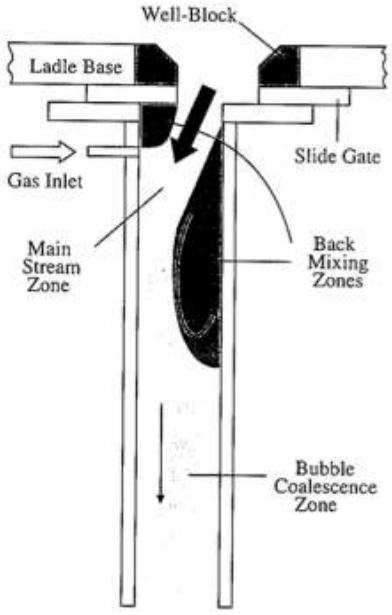

Figure 25 Schematic representation of fluid flow pattern in ladle shroud system[2]

The flow pattern inside the ladle shroud was identified by the back mixing zone as shown in Figure 25 [2]. The size of the back mixing zone decreases with increase slide gate opening. An air/water ratio of more than 0.45 will lead to cavitation in the back mixing zone. The flow pattern is independent of the gas injection ports.

Bai et al. [64] studied bubble formation during horizontal gas injection into a downward-flowing liquid. They found that in their water model, a low liquid flow speed and low gas flow rate will cause uniformly-sized bubbles form and detach from the side-wall. If the flow rate of liquid increases, the injected gas becomes elongated down along the wall and then breaks into uneven-sized bubbles. If both liquid flow and gas flow rates are high, the gas elongates over a longer distance down the nozzle walls, forming a sheet before breaking up into bubbles.

1.6 Experimental Set-up

Zhang and Wang [52, 59] used polythene particles with a density of 1.02g/cm^3 to simulate inclusions. Their contact angle is 91^o with water. The particle size was from 100-424μm. The study divided the inclusions into three groups: 100-140μm; 140-283μm; 283-424μm. However, the densities of the particles were not identical. The authors mentioned that density differences between particles was a source of error.

Zhu et al.[1] used polystyrene plastic particles to simulate the inclusions in steel; the size of those inclusions varying from 20-50μm. Those particles are chosen due to the contact angle of 110^o with density of 1g/cm^3. The inclusions are kept uniform suspended in the water by suspension compounds.

Li et al. [61] selected polystyrene plastic particles as inclusions as well. They reported that the contact angle between polystyrene plastic particles and salt water was 118^o. Their polystyrene plastic particles sizes are from 0.6-0.7mm. According to Sahai and Emi [65], these inclusions can imitate inclusions less than 50μm in the steel. The density of salt water is 1.02g/cm^3. In their experiment, they have also used some aromatic solvents as dispersant. The results are shown in Figure 26.

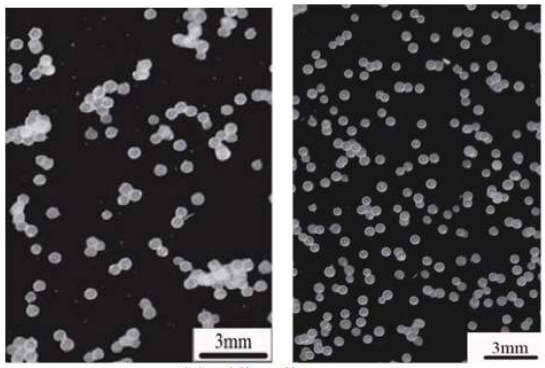

Figure 26 Particles with and without dispersant by Li et al. [61]

Feng et al. [57] suggested to use aniline to simulate inclusions and silicone oil to simulate slag in water. They argued that this selection could better simulate the possible aggregation of inclusions than polymers.

Chapter 2 Experimental Work

2.1 Introduction

Chapter 1 concluded that small gas bubbles could help improve the removal efficiency of small inclusions. However, due to the high surface tension and the non-wetting characteristic of liquid steel, small gas bubbles could not be generated through conventional methods, such as porous media, nozzles, lances or tuyeres. Therefore the 'bottom blowing method', though it was demonstrated to be working in aqueous models, most likely would not work once put into a real liquid metal scenario. On the other hand, the 'ladle shroud blowing method' shows a lot of potential as the most promising candidate to be able to generate small bubbles in liquid metal applications.

However, we still lack the knowledge and understanding of the mechanism of bubble generation under turbulent conditions in a ladle shroud. Several studies[2, 19, 60-62] performed water-modeling experiments on the 'ladle shroud blowing method' and claimed to be able to successfully generate bubbles in the range of 0.5-3 millimeter in diameter. Unfortunately, none of these studies performed reliable bubble size measurements. Instead, the size of the bubbles was only 'estimated' by visual examination with little justification. Second, each of these studies reached a different optimal condition for operation that varied due to the differences in experimental set-up among these studies.

Therefore, the main objective of this research is to have a quantitative understanding of the mechanism of bubble generation under turbulent conditions in the ladle shroud, as well as to propose a universal optimal operation condition for bubble generation in ladle shroud applications.

To experimentally study the mechanism of bubble generation under turbulent conditions in the ladle shroud, two criteria must be met: 1, precisely controlled turbulent environments and 2, accurate and precise measurements of bubble sizes. Due to the lack of transparency of liquid metals to visual light wavelengths, as well as the high temperature operating environments, one generally looks for low temperature, transparent models of these pyro-metallurgical processes. As such, a large number of metallurgical process studies have been made using aqueous systems. It is often legitimate to simulate

gas and liquid metal interactions in aqueous systems, and many studies suggest that properties such as gas hold up and average rising velocity of bubbles simulated in aqueous solutions match those found in actual liquid metal systems [66-68]. These studies proposed various bubble formation models and identified parameters including; inside nozzle diameter, liquid density, viscosity, surface tension, gas velocity and gas density, to describe bubble size, and bubble frequency, as a function of gas flow rate [69].

2.2 Experimental set-up

A schematic diagram of experimental set-up is shown below, as Figure 27. The top tank represents the ladle (referred as the 'ladle model' in the rest of this text) while the bottom tank represents the tundish (referred as the 'tundish model' in the rest of this text). The tube connecting the two tanks represents the ladle shroud (hence referred to as the 'ladle shroud model' in the rest of this text). The red-circled part serves as a function of the slide gate.

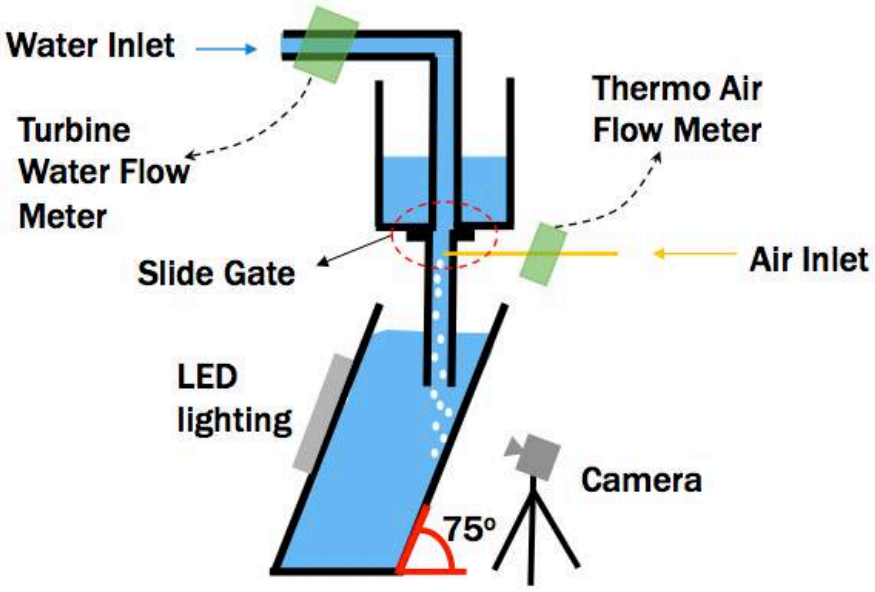

Figure 27 Schematic diagram of the experimental set-up

Water was directly introduced from the top into the system through a water hose as shown in Figure 27. A turbine water flow rate sensor was installed in the water line to measure the flow rate of the water. The turbine water flow rate sensor is equipped with a

LCD panel, to provide a the digital reading of the instantaneous flow rate. The water flow rate was controlled by the ball valve of the water hose.

Air was introduced into the ladle shroud model through small size orifices located beneath the slide gate. A high precision thermo air flow rate sensor was installed in the air line to measure the air flow rate. An LCD panel is also built into the sensor to read the digital value of the instantaneous flow rate. The air flow rate was controlled by a high precision needle valve. As shown later in Chapter 4, to generate small bubbles, the air flow rate needs to be very low and well controlled. Therefore, the air rotameter used in previous studies [2, 19, 60-62] is not suitable for the current research. Finally, a pressure gauge was installed in the air line to monitor the air pressure.

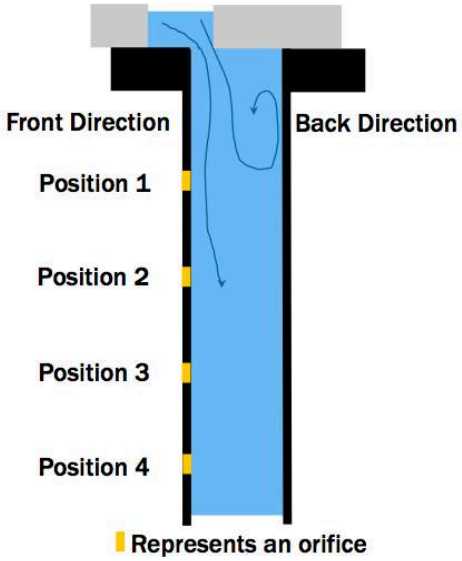

Figure 28 Enlarge details for the orifices in the ladle shroud

Figure 28 shows the enlarged details for the orifices design in the ladle shroud model. 3 sets of ladle shroud with 0.3mm, 0.5mm and 1.0mm diameter orifices respectively were built for this experiment. All ladle shroud models have an inner diameter of 21.0mm. In each ladle shroud model, 4 orifices were precisely drilled by laser near the top region of the tube. This was connected right below the slide gate. The CAD design drawing for the ladle shroud model can be found in Appendix I. As shown later in Chapter 4, the turbulence dissipation rate decays quickly along the ladle shroud. As such, the orifices were designed to be concentrated in the top part, instead of evenly distributed down along the tube. Figure 28 also shows that when the slide gate was not fully open, a back flow would occur. Therefore, the ladle shroud model was designed to

have a square flange as shown below, in such a way that it can be installed with 90^{o} rotational ability. By rotating the ladle shroud model, the air can be injected into the system at the front direction (expected to have high water flow speed), at the back direction (expected to have back flow when slide gate is not fully closed), as well as the side direction.

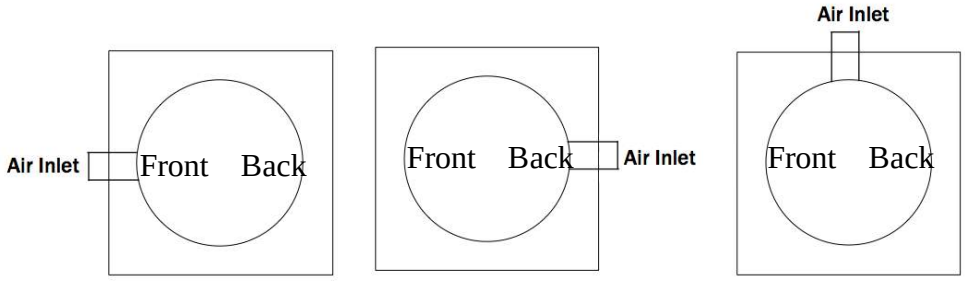

Figure 29 Front, Back, and Side Direction

Since the slide gate can alter the flow pattern of the water in the ladle shroud and vary the turbulence dissipation rate in the zone concerned, the slide gate opening ratio must be accurately controlled in order to quantitatively study the effects of the slide gate on sizes of bubbles generated. A conventional mechanically controlled slide gate set-up, for example the gear track type slide gate set-up in the MMPC full scale tundish, is not suitable for the current experiment due to the size limitation and the accuracy of the controlling lever. Therefore, an aluminum plate with 3 sets of drilled and tapped holes was used serve the function of the slide gate. The holes were arranged as shown in the Figure 30. The full CAD drawing can be found in Appendix II.

Each set of the holes was separated by 8.0mm. Once the ladle shroud model was installed, the water can only go through the overlap area as shown in Figure 31. Depends on the set of holes chosen, the overlap area, more commonly referred as the slide gate opening ratio, varies from 23.8% open to 61.9% open to 100% fully open. The slide gate opening ratio was calculated based on the equation below:

$$Slide\ Gate\ Opening\ Ratio = \frac{L_{overlap}}{D_{ladle\ shroud}} \times 100\%$$

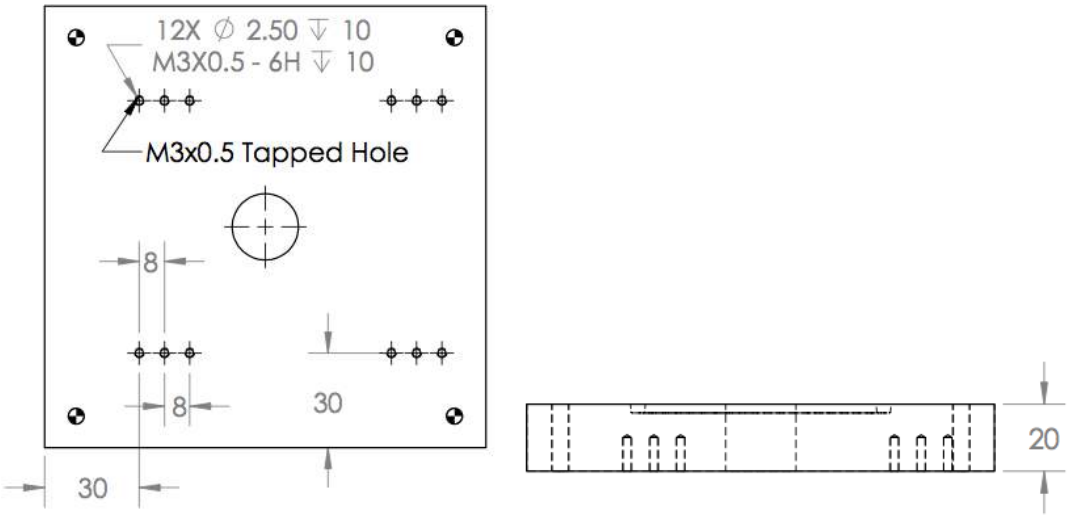

Figure 30 Aluminum plate with 3 sets of drilled and tapped holes

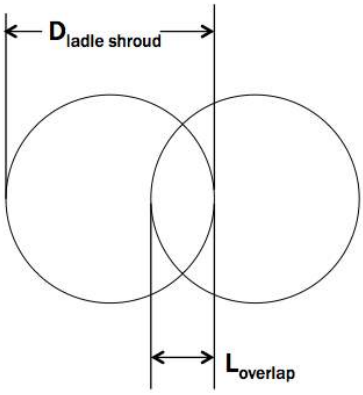

Figure 31 Slide gate overlap

Most of the experimental equipment parts (ladle model, ladle shroud model, tundish model) were made of Poly-methyl methacrylate (PMMA), or commonly referred as the acrylic glass, since PMMA combines the advantages of highly transparent properties and high mechanical strength. However, PMMA is relatively brittle, which limits its ability for drilling and tapping holes. Therefore the slide gate was made of aluminum alloy.

One key innovation in the experimental set-up was the design of the tundish model, the inclined tank as shown by the 75^{o} remark in Figure 27. The inclined surface made it possible to accurately observe and measure a monolayer of bubbles, which is crucial in quantitatively investigating relationships. From experimental observations, the bubbles generated from the orifices tended to follow the water stream to enter the tundish

model, hit and then slide along the inclined acrylic glass wall for a short period of time. This provided an observation window to characterize the bubble size distributions by utilizing optical measurement techniques.

On the contrary, all other researchers [2, 19, 60-62] who studied bubbles generation in ladle shrouds failed to characterize bubble sizes experimentally. In a few cases, pictures of bubble swarms were presented to estimate bubble sizes with very little justifications, as shown in Figure 32 a. However, once implemented, the inclined surface tank (observe only a monolayer of bubbles) provided a drastic improvement in the quality of the bubble pictures as shown in Figure 32 b. This innovation in measurement technique sets the corner stone to quantitatively analyze bubble generation mechanisms under turbulent conditions in the ladle shroud.

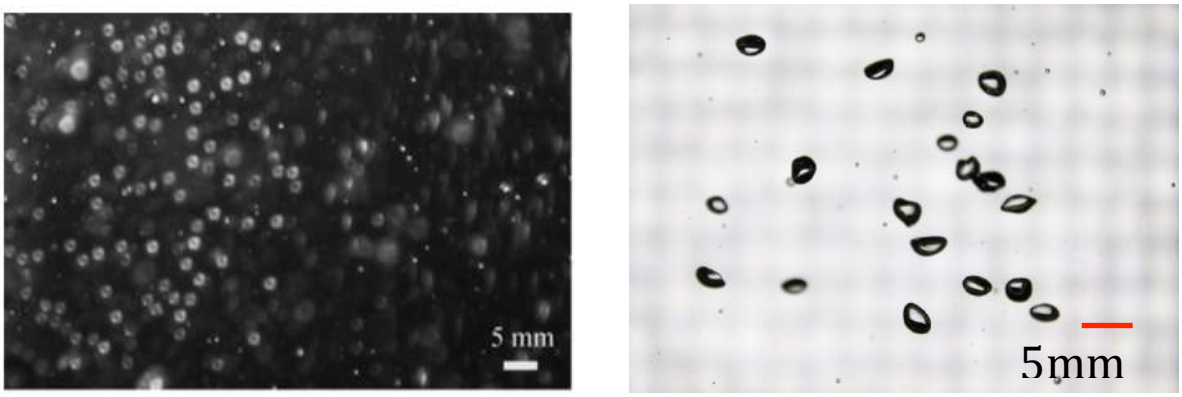

Bubble cluster [62] A monolayer of bubbles (current research)

Figure 32 Bubble measurement comparison

2.3 Optical measurement techniques

Optical measurement techniques were used in the experiments to characterize bubble size distributions. In order to achieve reliable and accurate experimental results, two factors must be met: 1, proper setting of camera and lighting: to get clear, sharp, well illuminated pictures of a monolayer of bubbles and 2, image processing: fine tuned image processing routines to analyze the pictures.

2.3.1 Settings of camera and lighting conditions

A professional Digital Single-lens Reflex (DSLR) camera, model Canon 50D, was used to capture bubble images. This model is capable of taking photos with a maximum 4752*3168 pixel resolution with highest ISO (a measurement of the camera

light sensitivity) of 3200 while the fastest shutter speed is 1/8000 second. In the experiment, the picture format was set as ‘large’ to get maximum resolution pictures. The ISO was set to 200 to avoid over-exposure and ‘noise’ in the pictures. The shutter speed used usually was in the range from 1/4000 to 1/5000 second.

Ideally, a macro lens should be used in this experiment since a macro lens is usually equipped with a bigger aperture that can provide better focus for near objects in a fixed picture frame. However, the cost of a macro lens is almost triple that of a normal lens. After testing both a macro lens and a normal lens, it was found that the improvements brought from the macro lens were not very significant. Therefore, a normal 50mm lens with a 5.6 aperture was used in the experiment.

A professional photography level LED light was installed on the back of the inclined tank to provide consistent and bright lighting conditions. It is worth pointing out that when the experimental equipment is largely built using PMMA materials, high power light sources should be avoided. Because the heat from high power light sources could easily build up and soften, or even melt the PMMA.

Both the camera and the LED light were supported by tripods, so as to avoid any vibrations. A remote shutter line was used to take images without physically pressing buttons on the camera. Due to the high shutter speed, even the slightest shake of the camera body can lead to blurry images, these are useless as they cannot be processed later in the computer.

2.3.2 Image and data processing

In the first step, the program ‘ImageJ’ was used to process the pictures of bubbles taken from the experiments. For each set of experiments, one random picture would be chosen to fine-tune the process routine parameters. Once the parameter values were set, a macrocode was written (see in Appendix III) to batch process the set of images to record size of each bubble into a text file.

In the second step, the text files would be imported into Excel to perform statistical analysis. Due to the extremely high volume of data from the text file, an Excel macrocode (see in Appendix IV) was also written to automate the importation and statistical analysis procedures. Finally the processed data would be imported into a program called ‘Origin’ to produce graphs.

2.3.3 Image processing routines

1. Get the scale factor: A ruler image (as shown in Figure 33) was imported into ImageJ. The pixel quantity across a certain physical distance was reported from the program. For example in Figure 33, 2617 pixels represent 35mm distance, which means 74.86pixels/mm. This ratio was used in ImageJ as the scale factor.

Figure 33 Ruler Image

2. Convert picture to 8-bit format: A random picture was chosen to convert the original RGB (24-bit) format to a new 8-bit format. This conversion is necessary as in the next step: threshold set-up can only work properly with limited colors. The 24-bit photo contains 2^{24} = 16,777,216 colors while the 8-bit photo only contains 2^{8} = 256 colors. The conversion is shown in Figure 34.

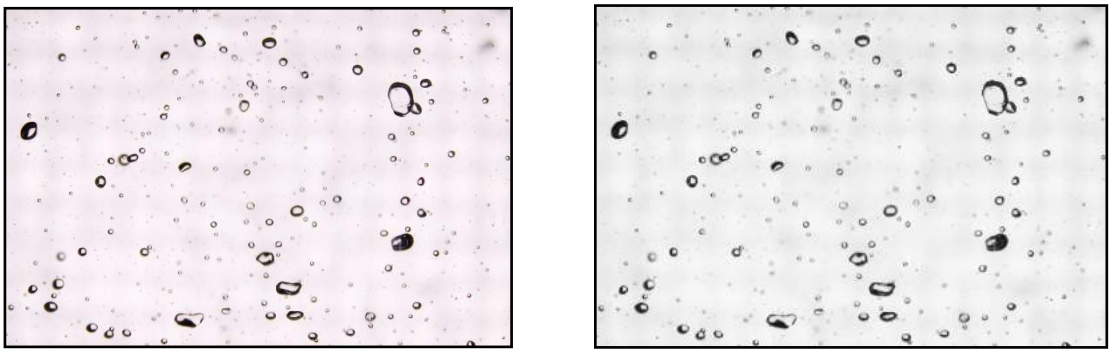

24-bit 8-bit

Figure 34 24bits photo would be degraded to 8bits photo

3. Threshold set-up: The 8-bit picture then went through a manual threshold set-up process. The optimal threshold limit was found through trial and error. As shown in Figure 35 a, the red contour was used as an indicator for the threshold limit selected. Once the proper threshold limit was confirmed, one can apply the threshold and get a

black and white image as shown in Figure 35 b. One should avoid the use of the built-in automatic threshold function, in the ImageJ, for air bubble analysis. This follows because through dozens of tests, the automatic threshold function always failed to properly identify the optimal thresholds.

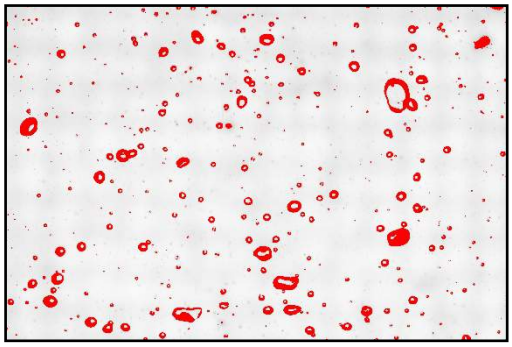

Threshold optimal value search

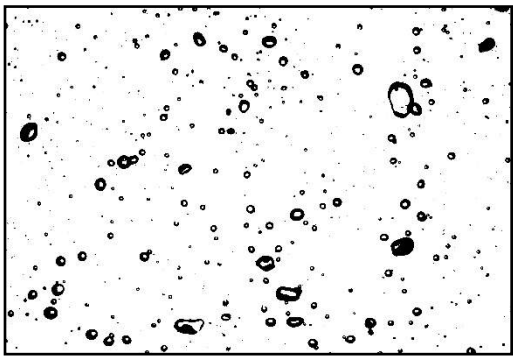

After apply Threshold

Figure 35 Threshold optimal value search

4. Particle analysis: The black and white image then went through particle analysis in ImageJ. Several parameters were carefully tuned such as minimum and maximum circularity, minimum and maximum areas, edge particles selection conditions etc.. Once these parameters were optimized, the processed image showed the bubbles identified (as shown in Figure 36) and also recorded each bubble size into a data file.

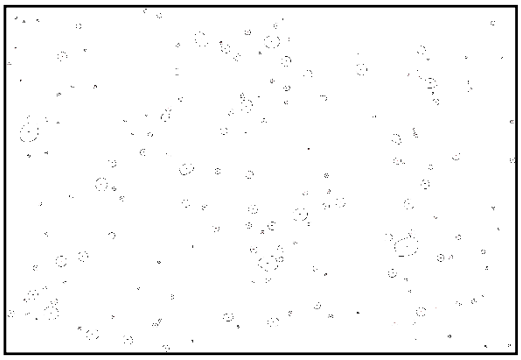

Bubbles identified

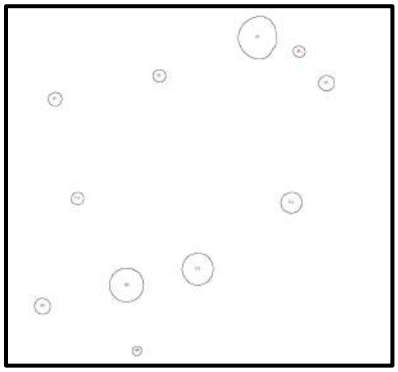

Enlarged details

Figure 36 Particle analysis results

5. Final check of the parameters: In this step, the identified bubbles were masked in black as shown in Figure 37 b, while the original RGB (24-bit) photo was shown in Figure 37 a. One can exam the results visually to make sure the bubbles identified from the program were proper and accurate.

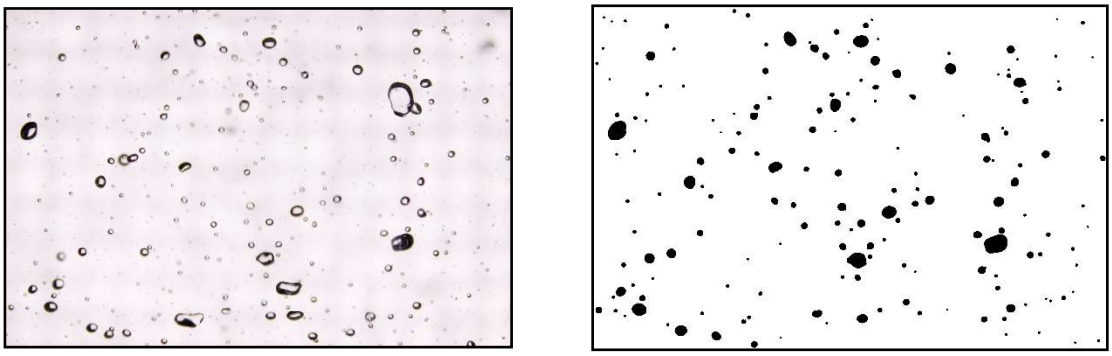

a. Original b. Masked

Figure 37 final checks of image process results

2.4 Bubble Size Controlling Factors

As discussed earlier in the experimental set-up part, six factors were identified as potentially influencing the size of bubbles generated. Therefore, six controlled experimental factors. Here is a short summary of the 6 factors and their corresponding values used in the experiments.

1. Water speed in the ladle shroud: the water speed in the ladle shroud model can influence the turbulent conditions in the ladle shroud model. The water speed was calculated based on the equation:

$$V_{water} = \frac{Q_{water}}{Area_{ladle\ shroud}}$$

Three average water speeds were tested in the experiments: 0.5m/s, 1.0m/s and 1.5m/s.

2. Air inlet rate: the air inlet rate plays an important role on the sizes of bubbles formed through an orifice. The air inlet rate in the experiments typically varied from 0.04L/min to 0.25L/min with four increments.

3. Slide gate opening ratio: the slide gate opening alters the flow pattern in the water within the ladle shroud model. Three slide gate opening ratios were tested in the experiments: 23.8% open, 61.9% open and 100% open.

4. Distance from the slide gate: the turbulence dissipation rate usually decays quickly along the ladle shroud model. Four positions were tested with distances: 3.0cm, 6.0cm, 8.0cm and 10.0cm.

5. Direction of the gas injection point: when the slide gate was not 100% open, back flow will occur opposite the entry point and the water speeds vary from the each side. Four orientations were tested: front direction, back direction and two side directions.

6. Orifice Size: From bubble formation studies[70-72], in static system orifice size can influence the bubbles generated. Three orifice sizes were tested: 0.3mm, 0.5mm and 1.0mm in diameter.

A full factorial experimental design showed that 3*4*3*3*3*4 = 1296 sets of experiments were required. During the study, it was found that the orientation of the gas injection point and the orifice size did not have a strong influence on the bubble sizes formed. Therefore, in total, around 800 sets of experiments were performed.

2.5 Experimental Procedures

The procedures for experiment preparation, performing experiments and post-experiments are summarized and presented below:

1. Experiment preparation:

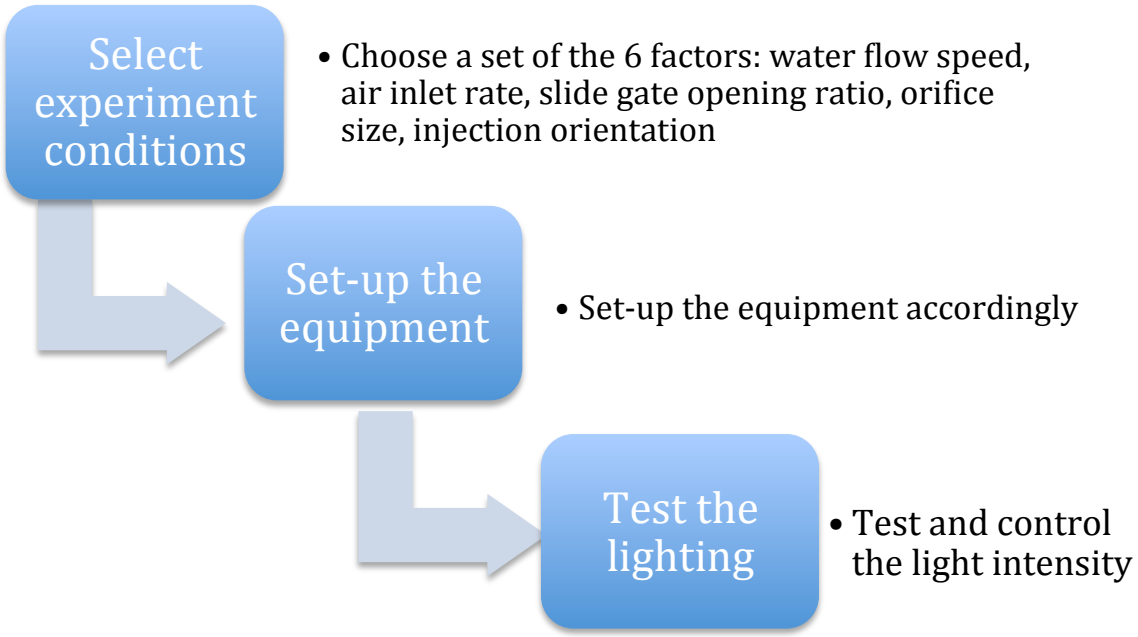

2. Perform experiment:

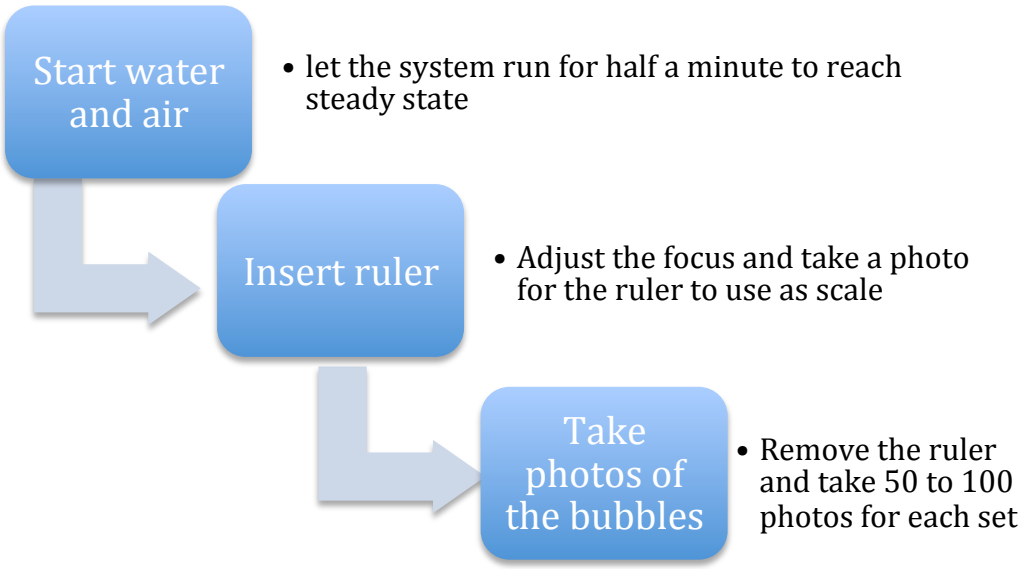

3. After the experiment

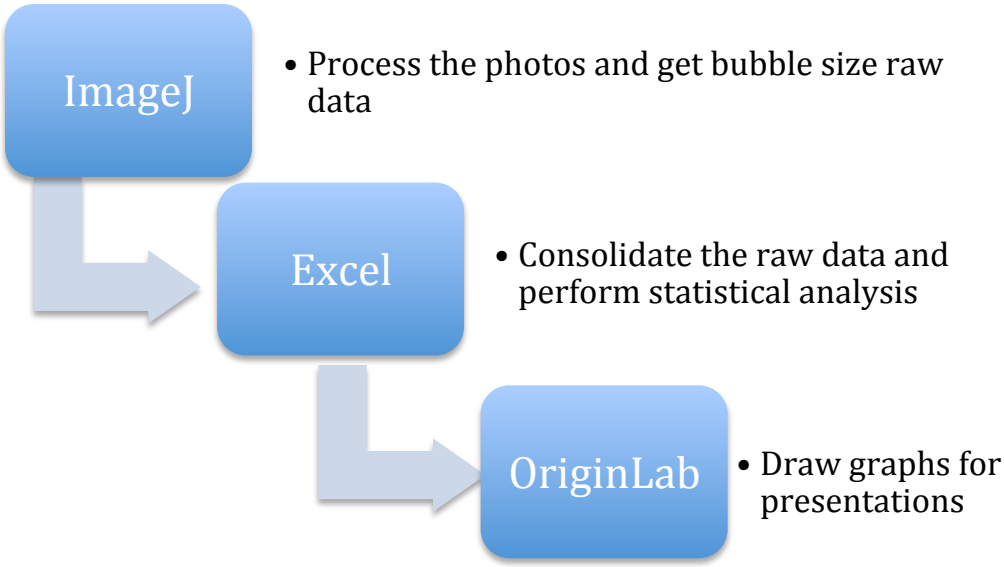

Chapter 3. Computational Fluid Dynamics (CFD) Work

3.1 Introduction of CFD

Computational fluid dynamics (CFD) uses the modern computer's strong processing power to numerically solve fluid mechanics conservation equations. Compared with physical modeling, which usually requires costly equipment and long set-up time, CFD has the ability to simulate complex fluid flows and to quickly provide key information to characterize the fluid flows. Several CFD codes, either free or commercial, are available. In this research, we used the commercial CFD code package by Ansys Fluent (version 14.5.7). The Ansys Fluent code uses the finite volume method (FVM) approach to solve the conservation equations.

For instance, in the current research, it is believed that bubble formation in the ladle shroud is heavily influenced by local fluid dynamic properties, such as the local instantaneous water speed and the local turbulence dissipation rate. However, to physically measure those local values, usually one needs to rely on complex and expensive equipment such as: wire anemometers, laser Doppler anemometers or PIV (Particle Image Velocimetry) [73].

Another problem is that the conservation equations are highly non-linear partial differential equations, so it is almost impossible to achieve analytical results. For example, one important factor in this research is to find the local turbulence dissipation rate. Tang [44] and Evans [41] proposed some semi-empirical equations to calculate the turbulence dissipation rate in a mixing zone, but those equations are highly dependent on geometry. Not to mention those equations also need some experimentally determined values, which are not easy to measure.

However, once CFD has been implemented to simulate the ladle shroud flow process, the local speed and local turbulence dissipation rate can be readily obtained. As such, the CFD simulation results together with the water modeling experimental results can then be used to perform a quantitative analysis of bubble generation mechanisms in turbulent flow conditions specific to ladle shrouds.

3.2 CFD Procedures

3.2.1 Four steps of CFD

Generally there are four steps in a CFD simulation, as shown below. The software used for each step is presented below each flag.

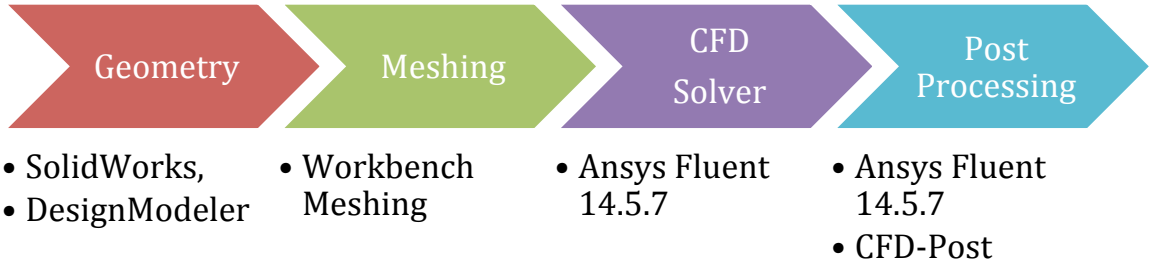

1. Geometry:

The 2D/3D geometry must be constructed first in order to start a CFD simulation. For fast and robust CFD calculations, the geometry needs to be built as 'clean' as possible. Namely the geometry should only reflect the most important features. Too much geometry details do not necessarily lead to more accurate results. On the contrary redundant details make it harder to produce good meshing, which actually limits the CFD performance.

When constructing a multi-body geometry, it is always suggested to keep the geometry conformal. Otherwise, the non-conformal surfaces can easily cause the Fluent calculation to diverge. The Ansys DesignModeler program is highly recommended for constructing multi-body structures, as the program will always keep the geometry conformal. If the geometry was built by other CAD programs (e.g. AutoCAD, Solidworks), clean up of the geometry before meshing is required.

2. Meshing:

Meshing means to discretize the fluid domain into finite volumes, or cells. Conservation equations will be solved from cell to cell. It is important to keep the meshing fine at regions where one expects large gradients (velocity, pressure, etc.). 'Ansys Workbench Meshing' program was used in all the CFD models meshing process for this research.

When the turbulence wall function is activated, it is also suggested to 'inflate' the geometry. This will make the layers of cells near the wall finer. The Figure below shows the inflation function.

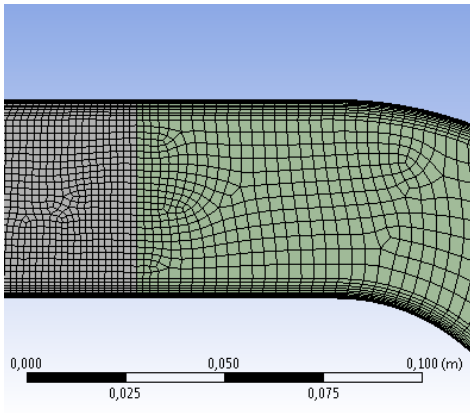

Figure 38 The wall gets finer

Typical meshing quality metrics include element quality, aspect ratio, skewness and orthogonal quality. In order to get fast and robust convergence calculations, the skewness must be keep low (<0.8) and orthogonal quality should be kept high (>0.7). Most importantly, one has to make sure that the minimum cell volume has a positive value; otherwise the mesh contains degenerate cells. However, it worth pointing out that the meshing can only influence the efficiency of the CFD calculation and speed of results convergence to a solution. The final CFD results should be mesh independent [74]. Meshing independent tests were performed in this research.

3. Fluent solver set up:

The typical Fluent solver work flow chart is shown in Figure 39. Two types of solvers are available in the Fluent code: pressure-based and density-based. The pressure-based solver is the most widely used solver, as it mainly targets simulating flows with Mach number less than 3. The density-based solver is normally used for >3 Mach number or for some very complex flows, such as shockwave interactions. All the CFD simulations performed in this research used the pressure-based solver.

When the Fluent pressure-based solver is selected, one must specify the pressure-velocity coupling scheme. The four available coupling schemes and their uses are presented in the table below.

Table 3 Pressure-velocity coupling scheme[74]

Pressure-velocity coupling scheme	Usage
SIMPLE	Day-to-day incompressible flow applications
SIMPLEC	Only for CFD academic interest
PISO	Suitable for transient calculations
Coupled	Good for applications with strong body forces resulting from rotation

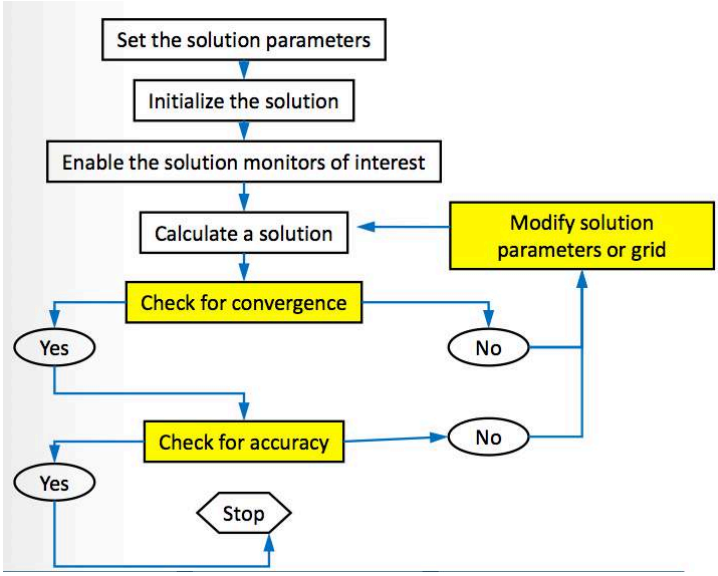

Figure 39 CFD solver process [74].

4. Post processing:

Once the CFD calculation is complete, the final data file can be imported into post processing programs to extract the information desired. Vector, streamline and contour graphs can be generated for presentation purposes.

5. Parameterize:

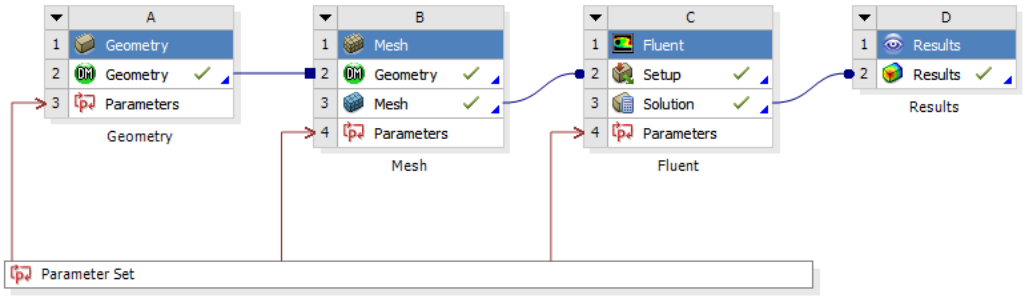

Figure 40 Parameterize of Workbench

It is highly recommended to use the Ansys Workbench scheme, as shown in the figure above. Besides the excellent file organization, and seamless connection between different components, the Workbench allows the user to parameterize their model. The same parameter set can be used through the whole cycle of CFD calculations, which makes it extremely easy to try different set-ups.

3.2.2 Governing Equations and Models

Conservation equations (mass, energy, momentum) and other fluid flow governing equations (turbulence model, discrete phase model) are solved using the finite volume method in Fluent. In this research, there is no heat exchange; hence the heat conservation equation was not included.

1. Mass conservation:

$$\frac{\partial \rho}{\partial t} + \frac{\partial(\rho u)}{\partial x} + \frac{\partial(\rho u)}{\partial y} + \frac{\partial(\rho u)}{\partial z} = 0$$

for incompressible fluids: $\frac{\partial \rho}{\partial t} = 0$

2. Momentum conservation:

$$\rho\left(\frac{\partial u_x}{\partial t} + u_x\frac{\partial u_x}{\partial x} + u_y\frac{\partial u_x}{\partial y} + u_z\frac{\partial u_x}{\partial z}\right) = -\frac{\partial p}{\partial x} + \mu\left(\frac{\partial^2 u_x}{\partial x^2} + \frac{\partial^2 u_x}{\partial y^2} + \frac{\partial^2 u_x}{\partial z^2}\right) - \mu\frac{\partial}{\partial x}\left(\frac{\partial u_x}{\partial x} + \frac{\partial u_y}{\partial y} + \frac{\partial u_z}{\partial z}\right) + \rho g_x$$

$$\rho\left(\frac{\partial u_y}{\partial t} + u_x\frac{\partial u_y}{\partial x} + u_y\frac{\partial u_y}{\partial y} + u_z\frac{\partial u_y}{\partial z}\right) = -\frac{\partial p}{\partial y} + \mu\left(\frac{\partial^2 u_y}{\partial x^2} + \frac{\partial^2 u_y}{\partial y^2} + \frac{\partial^2 u_y}{\partial z^2}\right) - \mu\frac{\partial}{\partial y}\left(\frac{\partial u_x}{\partial x} + \frac{\partial u_y}{\partial y} + \frac{\partial u_z}{\partial z}\right) + \rho g_y$$

$$\rho\left(\frac{\partial u_z}{\partial t} + u_x\frac{\partial u_z}{\partial x} + u_y\frac{\partial u_z}{\partial y} + u_z\frac{\partial u_z}{\partial z}\right) = -\frac{\partial p}{\partial z} + \mu\left(\frac{\partial^2 u_z}{\partial x^2} + \frac{\partial^2 u_z}{\partial y^2} + \frac{\partial^2 u_z}{\partial z^2}\right) - \mu\frac{\partial}{\partial z}\left(\frac{\partial u_x}{\partial x} + \frac{\partial u_y}{\partial y} + \frac{\partial u_z}{\partial z}\right) + \rho g_z.$$

3. Turbulence model

There are three basic approaches to calculate a turbulent flow: Direct Number Simulation (DNS), Large Eddy Simulation (LES) and the Reynolds Averaged Navier-Stokes Simulation (RANS). RANS model is the most widely used model in industrial turbulence simulations due to this method offers reasonably accurate turbulence results together with affordable computational costs.

Ansys Fluent offers several RANS based turbulence models such as: standard k-ε, realizable k- ε, standard k-ω etc.. In this research, the standard k-ε model was chosen to solve the turbulence as the flows involved in the experiments are relatively simple flows (no presence of strong rotation or massive separation) and this model is robust and widely used.

$$\frac{\partial(\rho k)}{\partial t} + \frac{\partial(\rho k u_i)}{\partial x_i} = \frac{\partial}{\partial x_j}\left[\frac{\mu_t}{\sigma_k}\frac{\partial k}{\partial x_j}\right] + 2\mu_t E_{ij}E_{ij} - \rho\epsilon$$

$$\frac{\partial(\rho \epsilon)}{\partial t} + \frac{\partial(\rho \epsilon u_i)}{\partial x_i} = \frac{\partial}{\partial x_j}\left[\frac{\mu_t}{\sigma_\epsilon}\frac{\partial \epsilon}{\partial x_j}\right] + C_{1\epsilon}\frac{\epsilon}{k}2\mu_t E_{ij}E_{ij} - C_{2\epsilon}\rho\frac{\epsilon^2}{k}$$

3.2.3 Current CFD set-ups

Figure 41 and Figure 42 show the 3D and meshing results for two of the CFD models studied in this research.

Set-up to study the ladle shroud

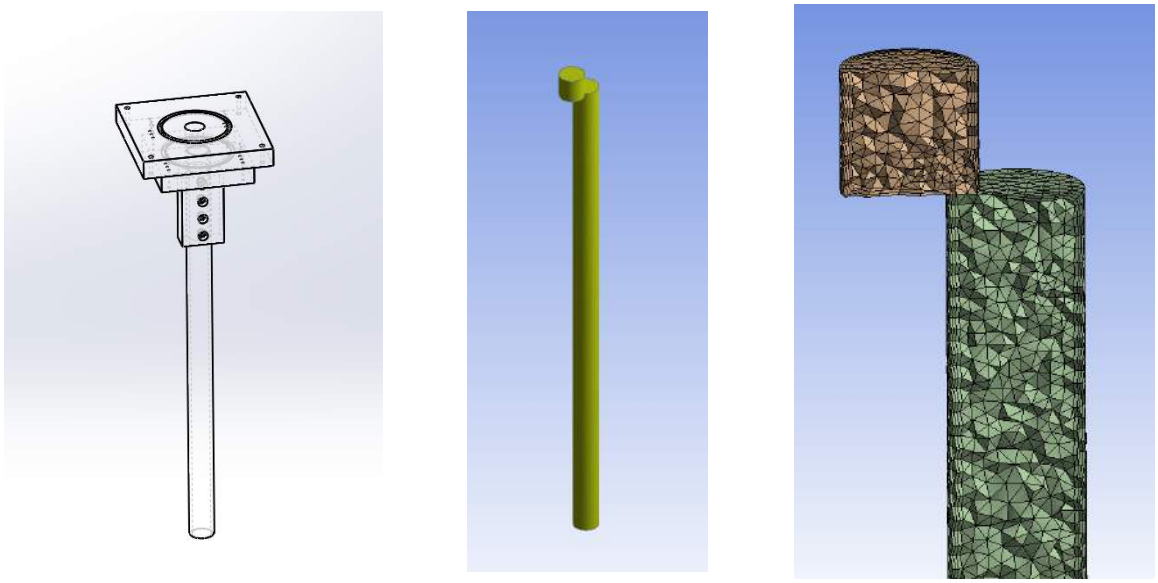

Full 3D Geometry | 3D Fluid domain | Meshing

Figure 41 CFD setups to study the flow in ladle shroud

Set-up to study the small bubble trajectories

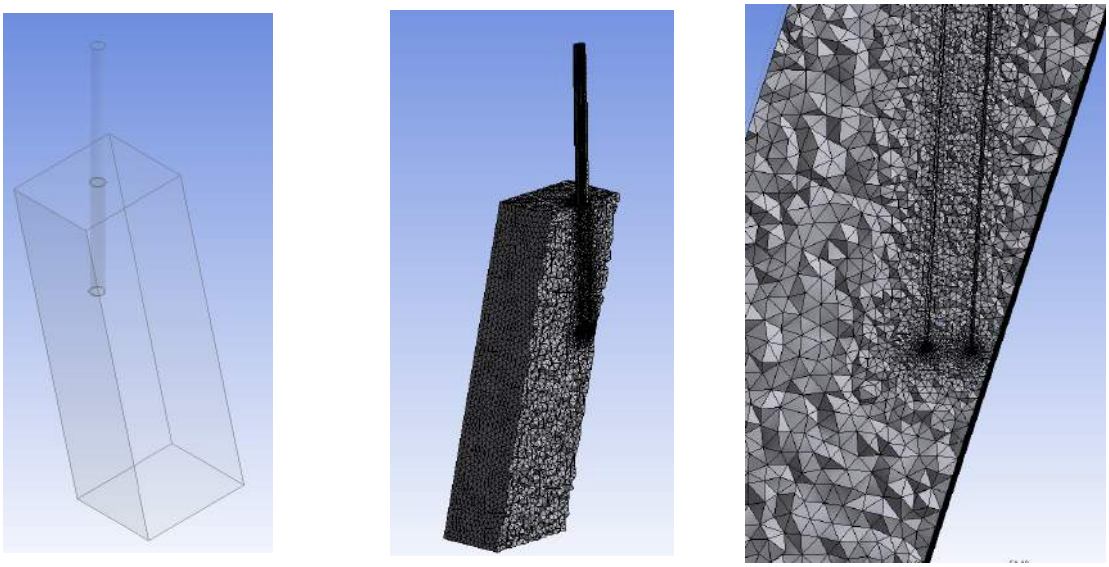

3D Geometry | Meshing | Meshing details

Figure 42 CFD setups to study small bubble trajectories

Figure 41shows that the full 3D geometry was simplified to get the fluid only domain for more robust and faster Fluent calculation. Wall inflation is shown in the meshing results. Figure 42 shows the finer mesh and gradual transition of mesh around close edges.

For all the CFD models in the present research, mesh independence was tested through three Ansys Workbench automatic meshing quality settings: coarse, medium and fine.

Chapter 4. Results and Discussion

4.1 Introduction

The six controlled experimental factors were assessed experimentally and the results are presented in this chapter. For each set of experiments, the fluid flow patterns and the turbulence conditions were simulated through CFD modelling.

The sizes of bubbles generated were found to be smaller than the predicted bubble birth size but larger than the theoretical critical bubble size in turbulent conditions. This indicates that bubble break-up occurred.

Finally, a quantitative physical model analysis was performed. The optimal conditions to generate small bubbles within ladle shroud are presented at the end of the discussion section.

4.2 Visual Observations

First, two regimes of bubble formation were observed: 1) when the water speed was high (1.5m/s) and the air injection rate was low (0.05L/min), small bubbles were generated as shown in Figure 43 a. Most of these bubbles were less than 1mm in diameter. 2) when the water speed was low (0.5m/s) and the air injection rate was high (0.25L/min), mostly big bubbles larger than 3mm were generated from the ladle shroud as shown in Figure 43 b.

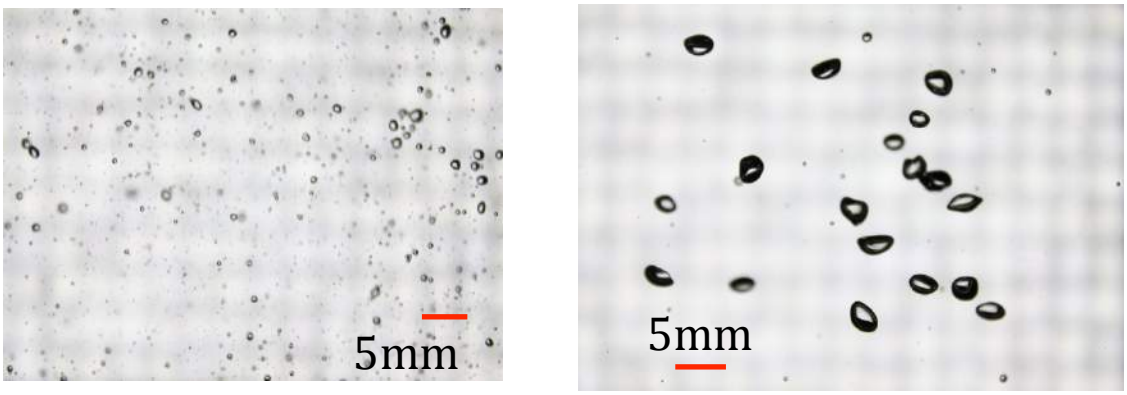

a b

Figure 43 Two regimes of bubble formation: a. small bubbles less than 1mm formed when the water speed is high and the air injection rate is low; b. big bubble more than 3 mm formed when the water speed is low and the air injection rate is high

Second, it was obvious that the bubble trajectories depended on the bubble size. As shown in Figure 44, big bubbles tended to hit the wall and quickly rise up to the surface. This is due to the larger buoyancy force of the big bubbles. The small bubbles, on the other hand, tended to follow the water streams and to fill the tundish model as shown in Figure 45. The DPM simulation results matched reasonably well with the experimental results. The differences in trajectories of bubbles of different sizes are in good accord with literature results [13, 63] [61].

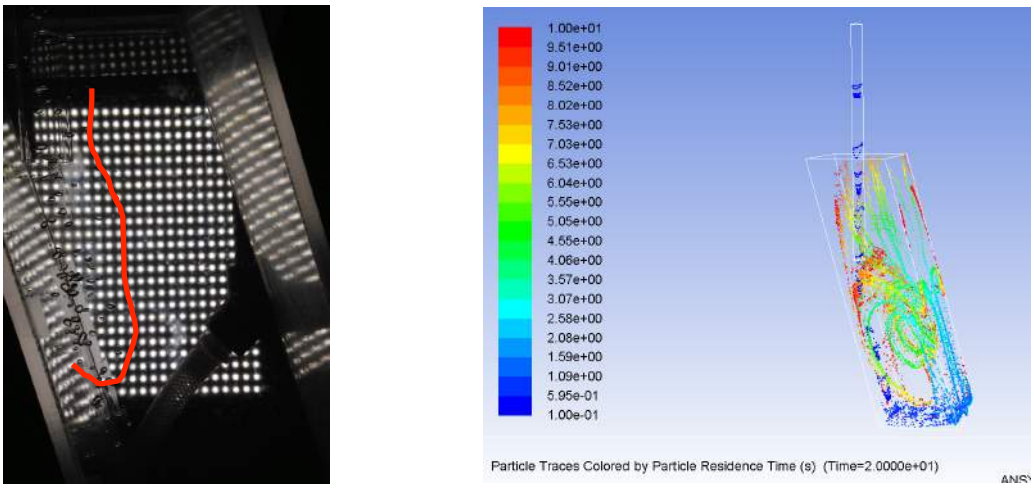

Experimental Results CFD simulation results

Figure 44 Big bubbles trajectories (Experimental results and CFD results): big bubbles hit the tundish model wall and quickly rise up

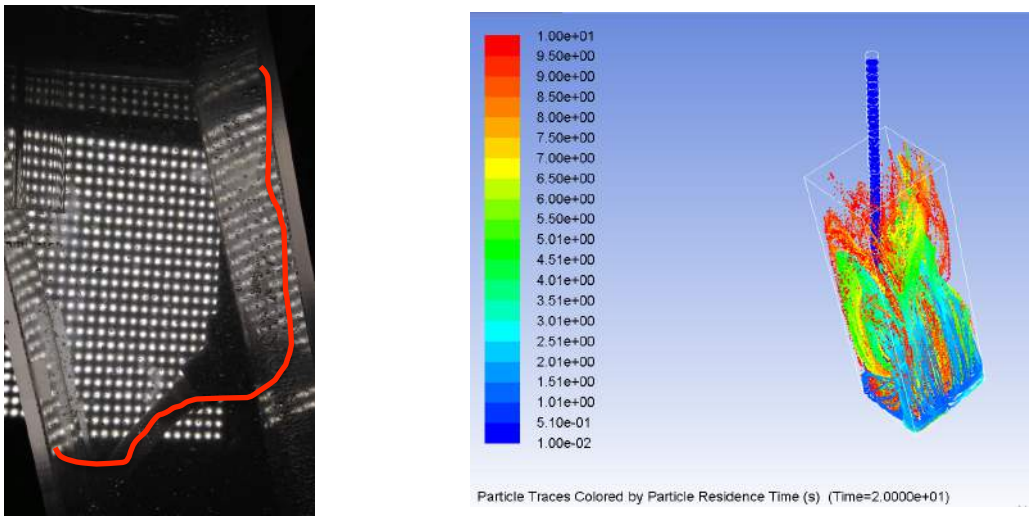

Experimental Results CFD simulation results

Figure 45 Small bubbles trajectories (Experimental results and CFD results): small bubbles follow the water flows and fill the tundish model

The trajectory results for the small bubbles further justified the choice of small bubbles to remove small inclusions. Now there are two reasons: first, small bubbles have higher a probability to collide with and to attach with, small inclusions (as explained earlier in Chapter 1) and second, small bubbles are better dispersed in the tundish model (as shown from the trajectory results). This would increase the probability of bubbles and inclusions meeting.

It worth mentioning that no significant bubble coalescence was observed in the current experimental set-ups and conditions. This was due to the water speed vs. air inlet speed ratio being relatively high. Hence, the system stayed in the 'bubble' regime as shown in Figure 46. Once the small bubbles enter into the tundish model, they quickly dispersed hence there was very little chance the bubbles could collide and coalesces with each other.

When the air inlet rate was set to very high values (e.g. 2.0L/min comparing with the 0.25L/min, the maximum experimental condition), massive bubble coalescence was observed. The water flows in the ladle shroud model were then in the slug/churn flow regimes.

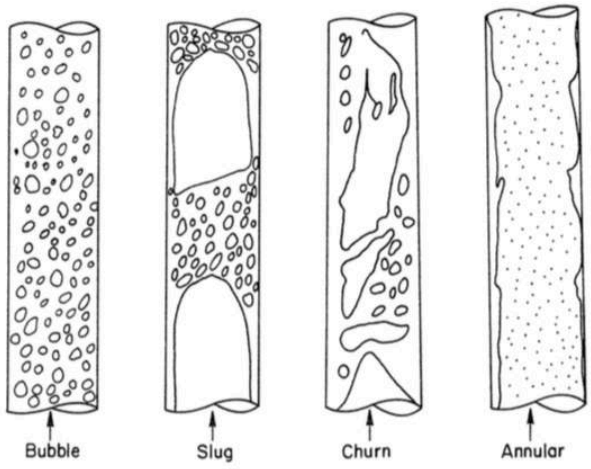

Figure 46 Generic regimes of gas and liquid interactions: from left to right, the liquid speed vs. gas speed decrease [75]

However, it would impossible to completely eliminate bubble coalescence. Therefore bubble coalescence is a source of error in bubble size characterizations.

4.3 Water speed vs. Bubble Size

Among the six controlling experimental factors, water speed was shown to have the strongest impact on the size of bubbles generated. In general, the higher the water speed in the ladle shroud model, the smaller were the bubbles generated. This trend is shown from Figure 47 to Figure 52.

Take Figure 47 for example, the three lines represent three sets of experiments with identical conditions except the water inlet speed. The X-axis shows the bubble size in diameter (unit: mm), and all three Y-axes are bubble counts. It is clear that the bubble size peak shifts with water inlet speed. High water inlet speed (blue line: 1.5m/s) has the bubble size peak around 0.5mm; medium water speed (red line: 1.0m/s) has the bubble size peak around 1.5mm; low water speed (black line: 0.5m/s) has bubble size peak around 2.5mm.

For a fixed air inlet rate (in this case it is 0.04L/min), if individual bubbles were smaller, there would be more bubbles in total. This is why there are three Y-axes: when bubble size peak (blue line) was around 0.5mm, the peak bubble count (blue Y-axis) went as high as 1800; when bubble size peak (red line) was around 1.5mm, the peak bubble count (red Y-axis) dropped to 200; when bubble size peak (black line) was around 2.5mm, the peak bubble count (black Y-axis) dropped below 100. If only one Y-axis was used, then the peaks of the red and the black line would not be seen.

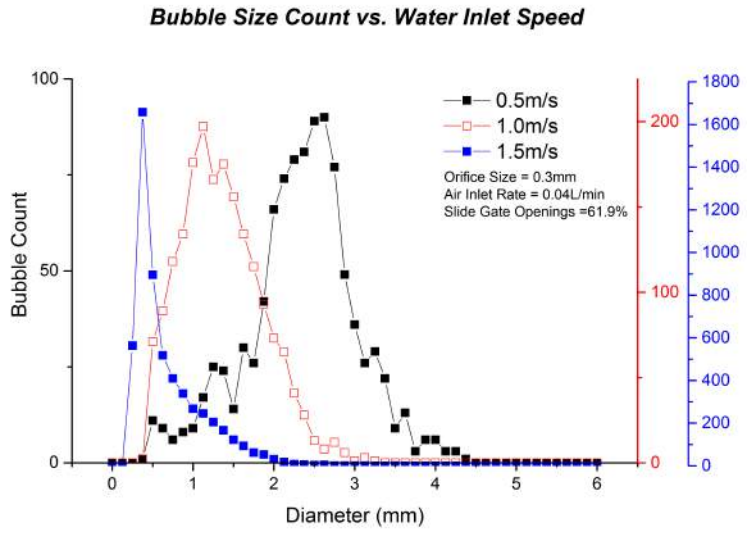

Figure 47 Bubble size vs. water inlet speed. Orifice size: 0.3mm; Air inlet flowrate: 0.04L/min; Slide gate opening ratio: 61.9%; Position 1

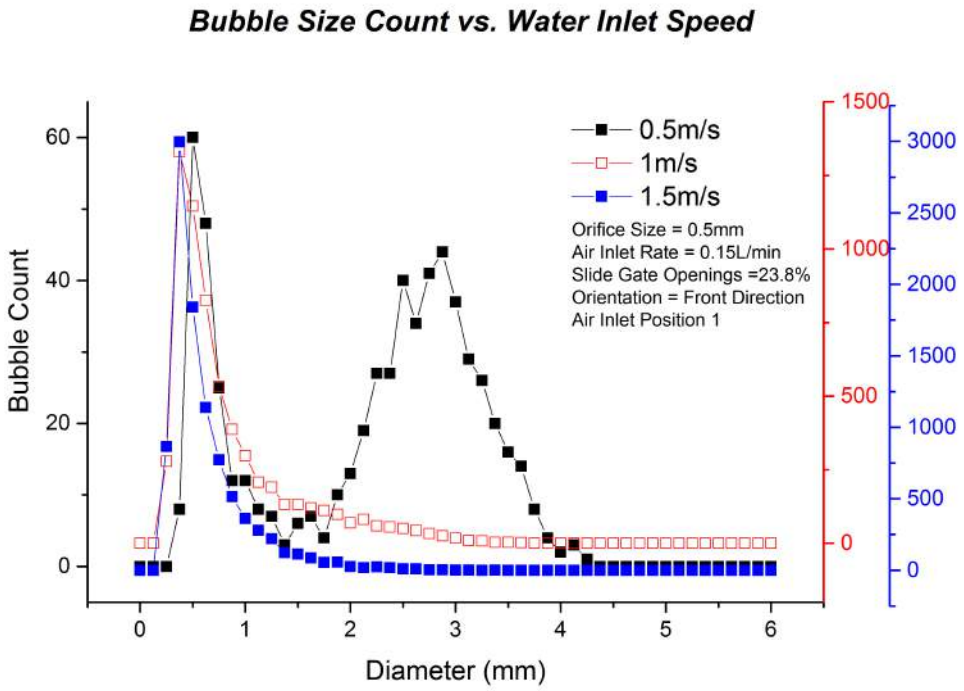

Figure 48 Bubble size vs. water inlet speed. Orifice size: 0.5mm; Air inlet flowrate: 0.15L/min; Slide gate opening ratio: 23.8%

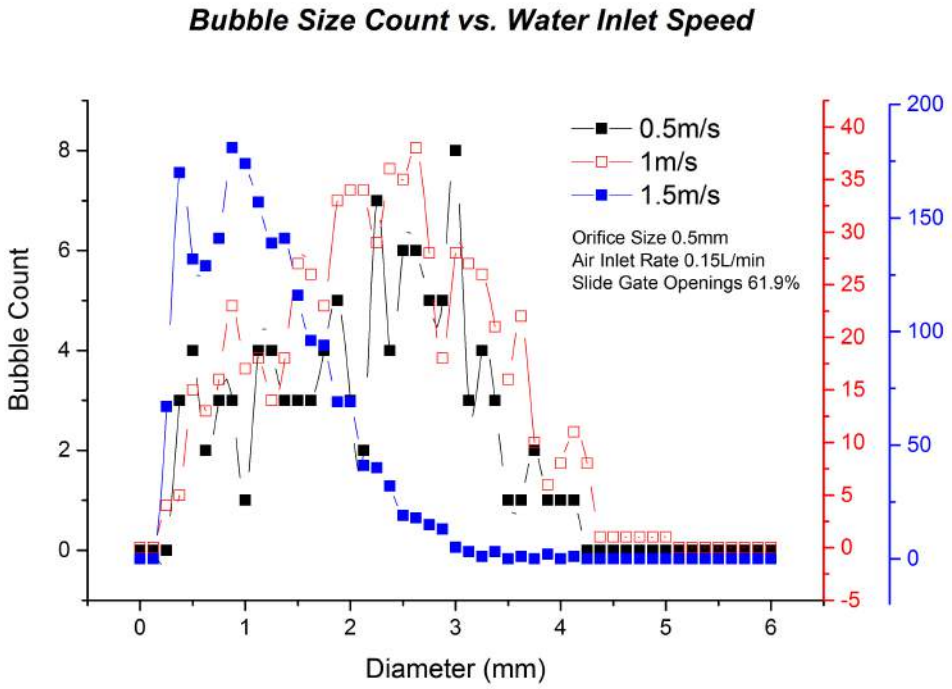

Figure 49 Bubble size vs. water inlet speed. Orifice size: 0.5mm; Air inlet flowrate: 0.15L/min; Slide gate opening ratio: 61.9%

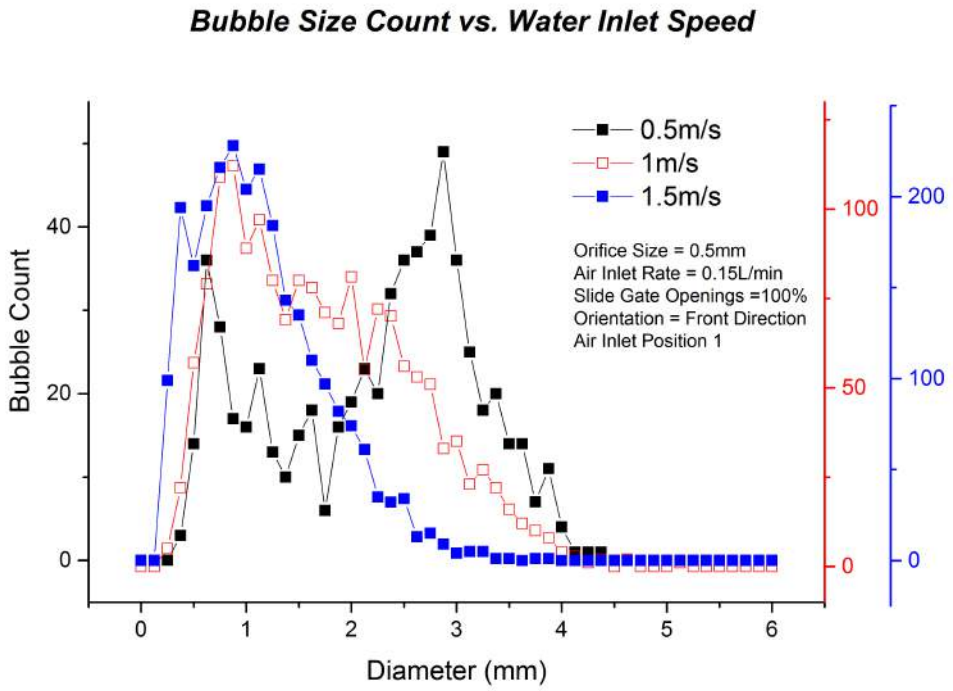

Figure 50 Bubble size vs. water inlet speed. Orifice size: 0.5mm; Air inlet flowrate: 0.15L/min; Slide gate opening ratio: 100%

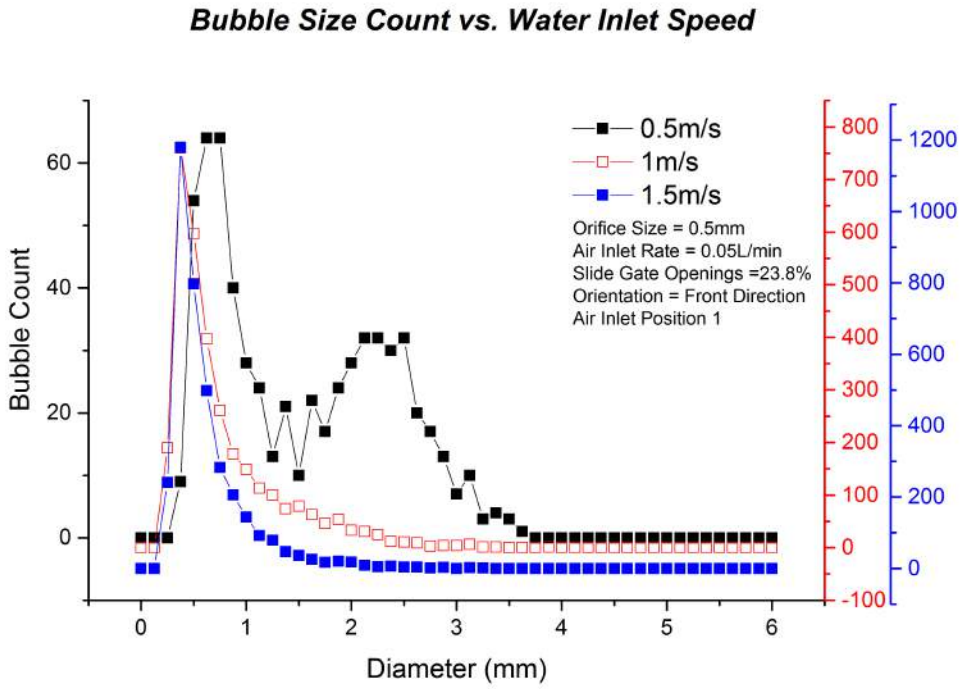

Figure 51 Bubble size vs. water inlet speed. Orifice size: 0.5mm; Air inlet flowrate: 0.05L/min; Slide gate opening ratio: 23.8%

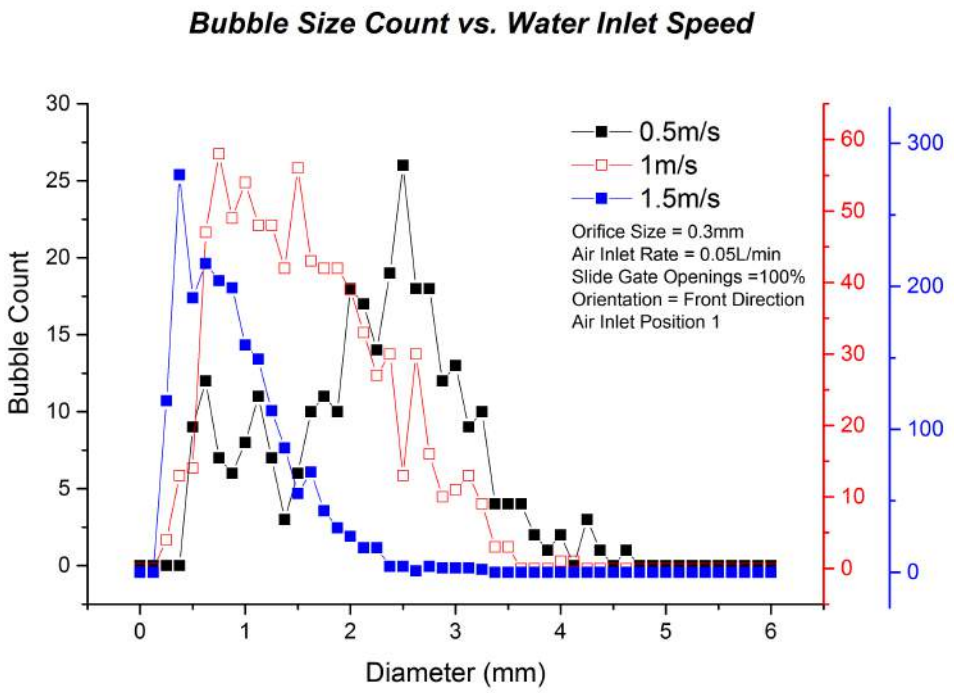

Figure 52 Bubble size vs. water inlet speed. Orifice size: 0.3mm; Air inlet flowrate: 0.05L/min; Slide gate opening ratio: 100%

4.4 Air Inlet Flowrate vs. Bubble Size

In general, the bubble size increased with the air inlet flowrate. Figure 53 and Figure 54 show the results of two sets of experiments with same set-ups and conditions, except for the air inlet flowrate. Figure 53 has low air inlet rate of 0.05L/min and Figure 54 has high air inlet rate of 0.15L/min. If one compares the blue lines (1.5m/s water) in Figure 53 and Figure 54, it is obvious that the right tail is bigger in the high air inlet rate, which means more big bubbles generated and an overall increase in the average bubble size. If one compares the red lines (1.0m/s water) in Figure 53 and Figure 54, it is obvious that the bubble size peak shifts to the right, which indicates less small bubbles generated and overall larger average bubble size. If one compares the black lines (0.5m/s water) in Figure 53 and Figure 54, it clear that bubble size peak shifts to the right as well, and the bubble size peak increased from 2.5mm in the low air inlet rate to 3.0mm in the high air inlet rate.

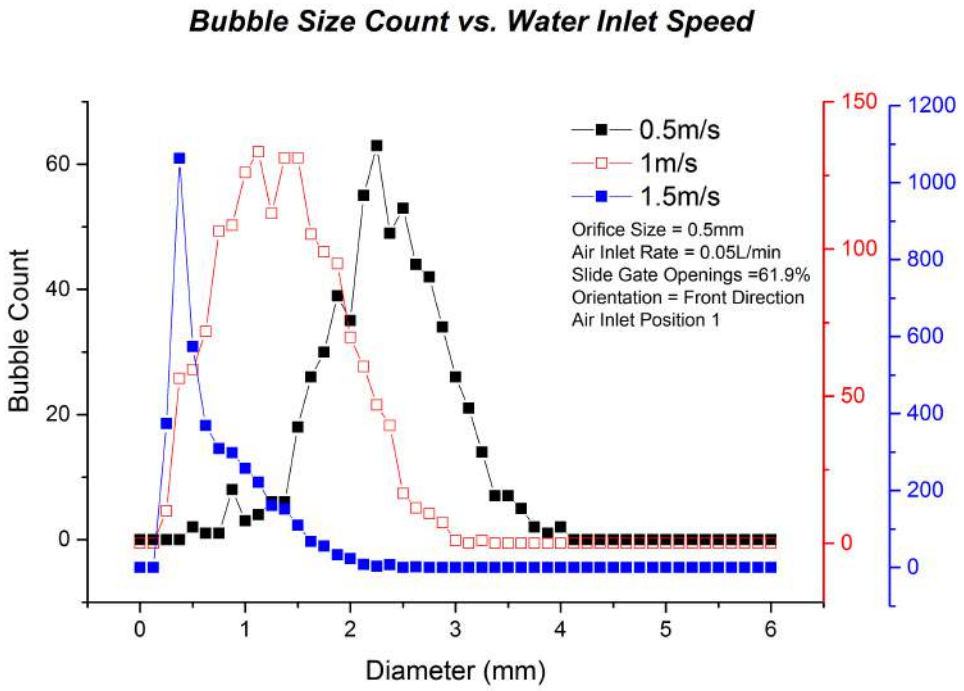

Figure 53 Bubble size vs. water inlet speed. Orifice size: 0.5mm; Air inlet flowrate: 0.05L/min; Slide gate opening ratio: 61.9%

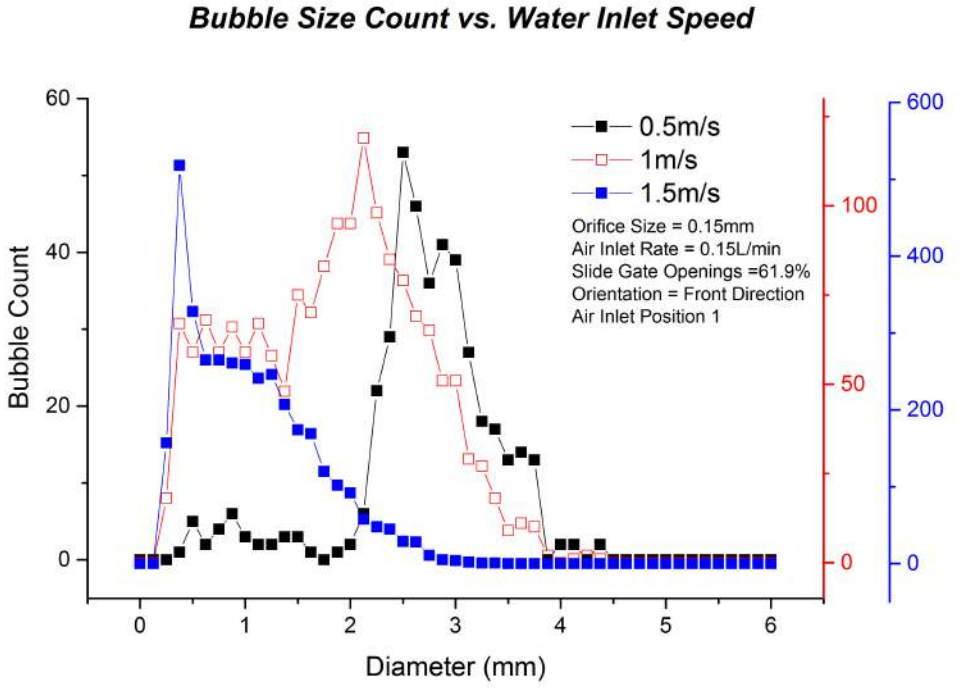

Figure 54 Bubble size vs. water inlet speed. Orifice size: 0.5mm; Air inlet flowrate: 0.15L/min; Slide gate opening ratio: 61.9%

Figure 55 to Figure 58 provide an alternative comparison to verify the effects of air inlet flowrate on bubble size. From Figure 55 to Figure 57, it is obvious that the distribution of the bubble size gradually shifts towards to the right with an increase in air inlet flowrate. This confirms that the bubble size increases with increase in air inlet flowrate. It is noticeable that there is a small peak on the left side of the distributions, which means a small quantity of small bubbles less than 1mm were created in the environment, where the majority of the bubbles generated were in the range from 2mm to 4mm. This most likely was caused by a small portion of the big bubbles breaking up into small ones. The exact bubble break-up process will be discussed later in Section 4.10.

In Figure 58, it is clear that the right tail increases with the air inlet flowrate. This means more big bubbles were generated with an increase in the air inlet flowrate, which leads to an overall average bubble size increase. The distribution shape in Figure 58 is different from the ones in Figure 55 to Figure 57, since the water speed was higher and the slide gate opening ratio was lower. High water speeds and low slide gate opening ratios are required for small bubble generation.

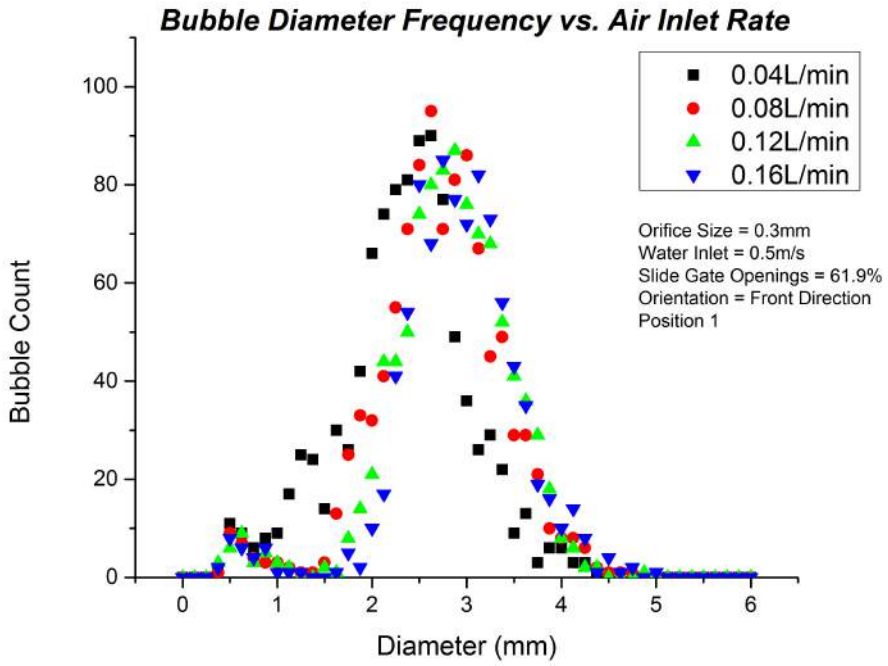

Figure 55 Bubble diameter frequencies vs. Air inlet rate. Orifice size: 0.3mm; Water speed:0.5m/s, Slide gate opening: 61.9%; Air injection at Position 1.

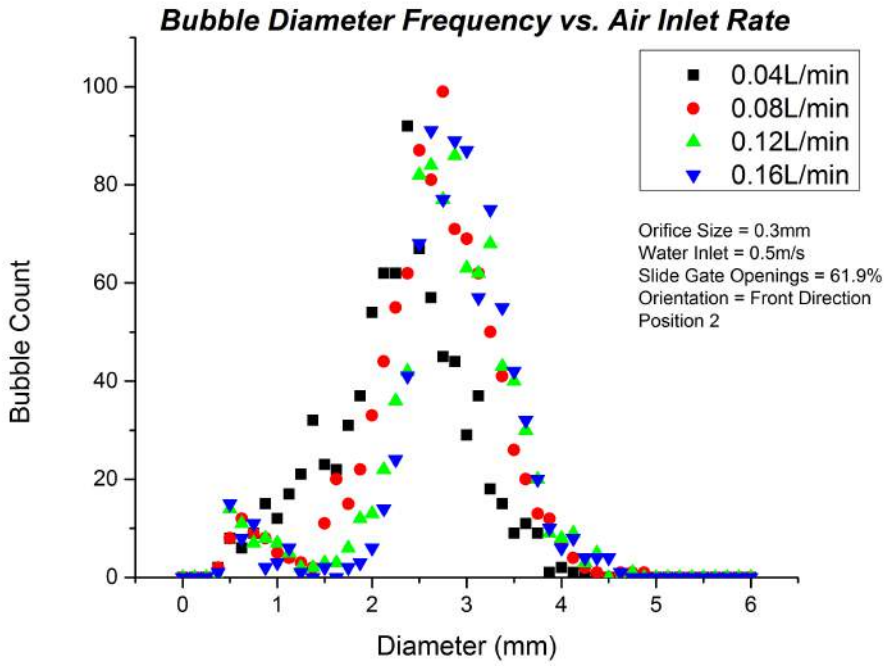

Figure 56 Bubble diameter frequencies vs. Air inlet rate. Orifice size: 0.3mm; Water speed:0.5m/s, Slide gate opening: 61.9%; Air injection at Position 2.

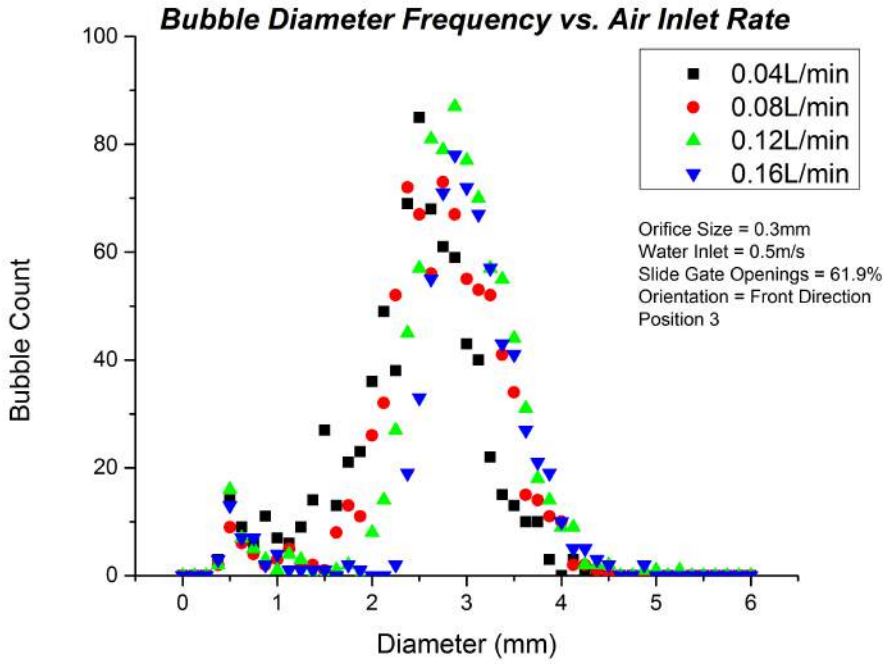

Figure 57 Bubble diameter frequencies vs. Air inlet rate. Orifice size: 0.3mm; Water speed:0.5m/s, Slide gate opening: 61.9%; Air injection at Position 3.

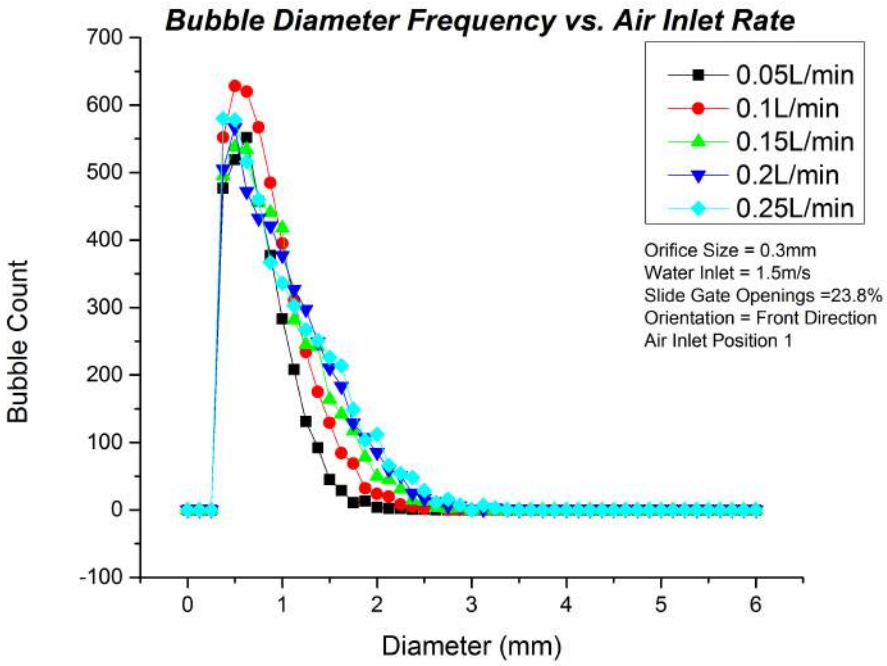

Figure 58 Bubble diameter frequencies vs. Air inlet rate. Orifice size: 0.3mm; Water speed:1.5m/s, Slide gate opening: 23.8%; Air injection at Position 1.

4.5 Orifice size vs. Bubble Size

Three orifice sizes were tested in the experiments: 0.3mm, 0.5mm and 1.0mm (all in diameter). As presented in Chapter 1, studies [20, 27-29] showed that for wetting systems, the size of bubbles generated through an orifice is positively related to the orifice size. However, from the current experimental results, the role of orifice size is more ambiguous, as shown in Figure 59 and Figure 60.

In Figure 59, where both water inlet speed and air inlet rate were low, the orifice size did not exhibit a strong correlation with the bubble size. In Figure 60, where the water speed was high and air inlet rate was low (this combination is most interesting in current study, as it can generate bubbles less than 1.0mm), the 0.3mm orifice generated smaller bubbles. The inconsistency of the role of orifice size was very likely caused by the complex interactions between experimental parameters and the bubble coalescence and break-up processes in turbulent conditions. However, to create small bubbles less than 1.0mm, a small orifice size is still recommended.

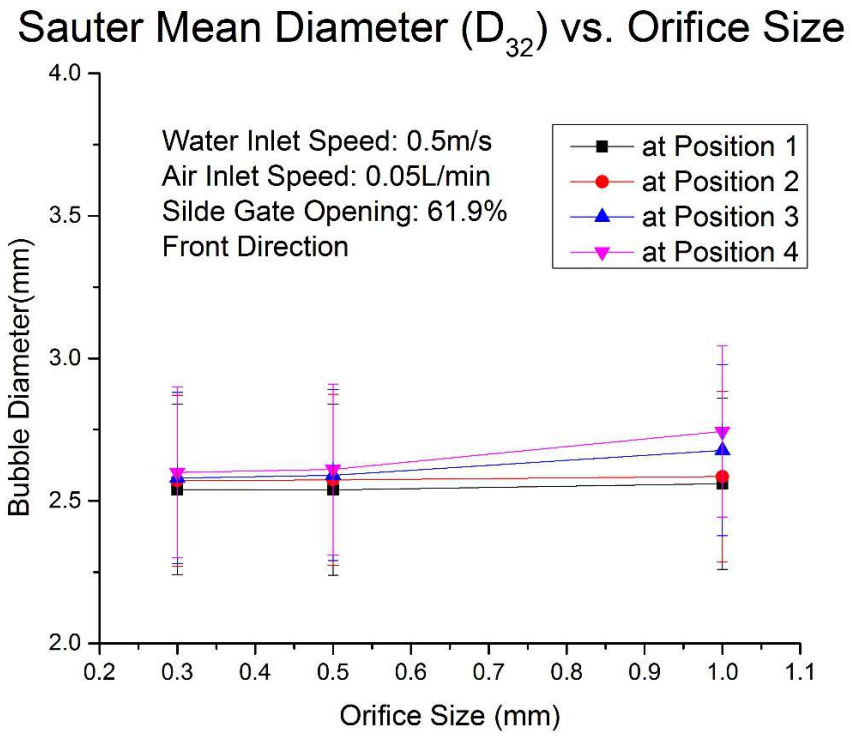

Figure 59 Bubble sauter mean diameter vs. orifice. Water speed: 0.5m/s; Air inlet rate: 0.05L/min (Positions 1-4 are demonstrated in Figure 61)

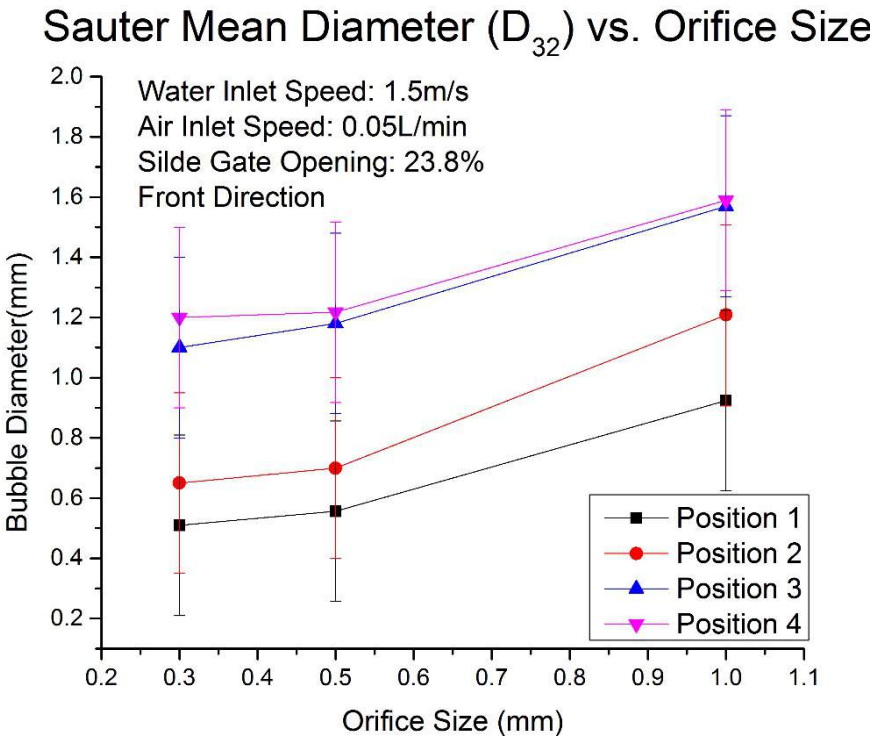

Figure 60 Bubble sauter mean diameter vs. orifice. Water speed: 1.5m/s; Air inlet rate: 0.05L/min (Positions 1-4 are demonstrated in Figure 61)

4.6 Slide Gate vs. Bubble Size (CFD and Experimental Results)

The slide gate, when partially opened, can alter the local flow patterns significantly and create flow velocity gradients around the slide gate, as shown in Figure 61. A high flow velocity gradient means high turbulence dissipation rates. As demonstrated in Section 4.10, a high water speed (1.5m/s) and high turbulence dissipation rates can help generate small bubbles. In general, it was found that smaller the slide gate opening ratio, smaller were the bubbles generated.

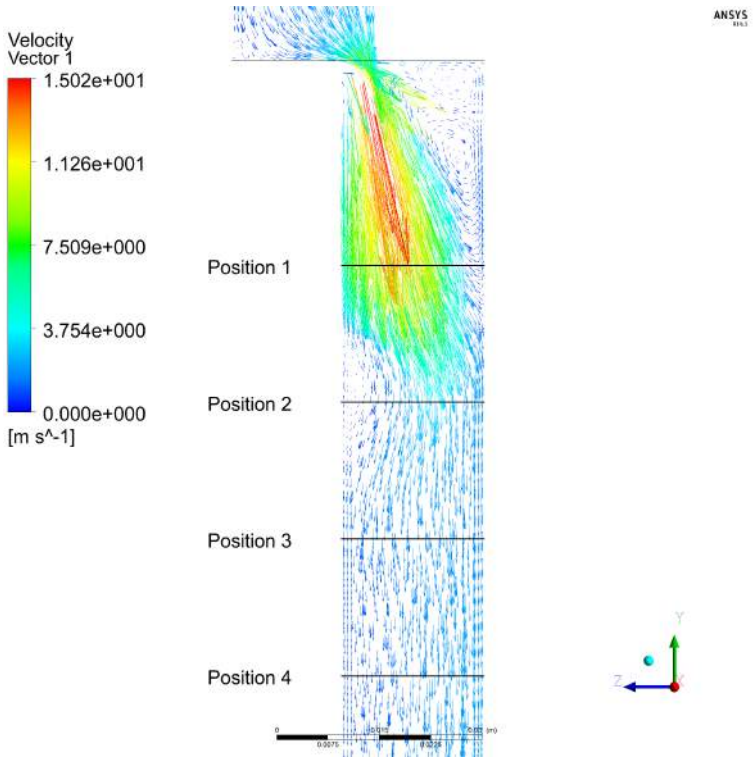

Figure 61 back flows and velocity gradient caused by partially opened slide gate

Figure 62 to Figure 74 present the CFD simulation results for 23.8% and 61.9% slide gate opening ratio with inlet water speeds of 0.5m/s and 1.5m/s. All graphs focus on the top 10% part of the ladle shroud model, where the gas injection orifices are located. The remaining 90% of the ladle shroud model are not presented because the flows practically reached steady state. Nearly zero velocity gradients and nearly zero turbulence dissipation rate existed below the top 10% part of the ladle shroud model. For the same reason, the 100% slide gate opening ratio results are not presented. Flow velocity contour

graph, flow velocity vector graph and turbulence dissipation rate contour graph are presented for each condition.

First, it was found that when the slide gate was not fully open, there were always back flows. The fluid low velocity decreased in the back flow region. For a fixed inlet water speed, the smaller the slide gate opening, the stronger the back flows. For a fixed slide gate opening ratio, the higher the inlet water speed, the stronger the back flows.

A second observation is that turbulence dissipation rate increased with water inlet speed and decreased with the slide gate opening ratio. The turbulence dissipation rate value was higher around high velocity gradients. The highest turbulence dissipation rate was achieved when the water was 1.5m/s and the slide gate opening was 23.8%. High water speed and low slide gate opening ratio are required for small bubble generation.

Finally, the turbulence dissipation rate was found to decay quickly along the ladle shroud.

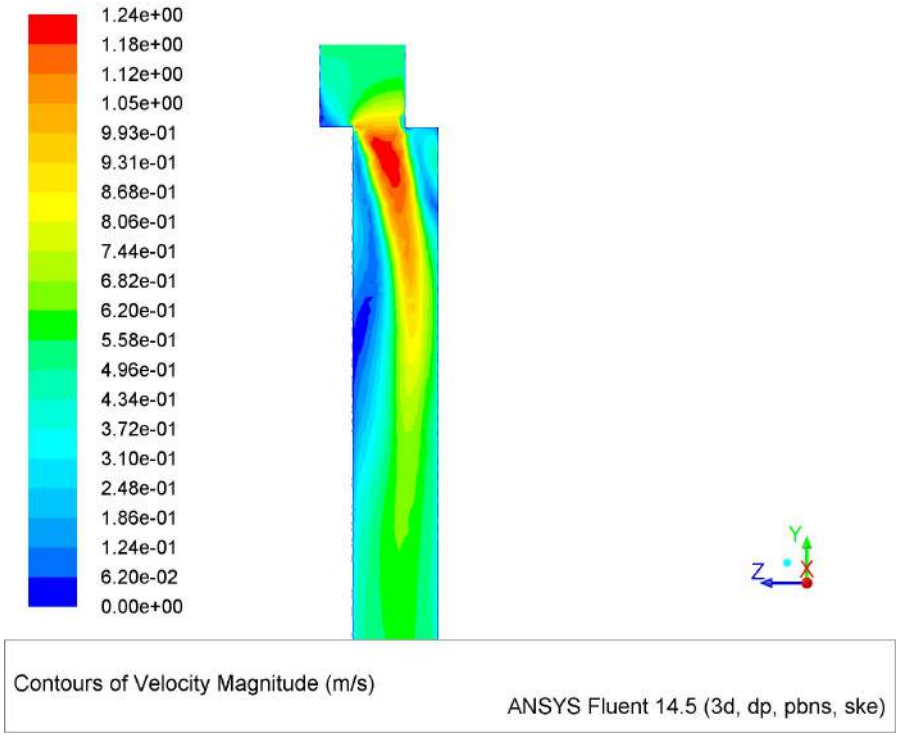

Figure 62 Velocity Contour. Water speed: 0.5m/s, slide gate opening: 61.9%

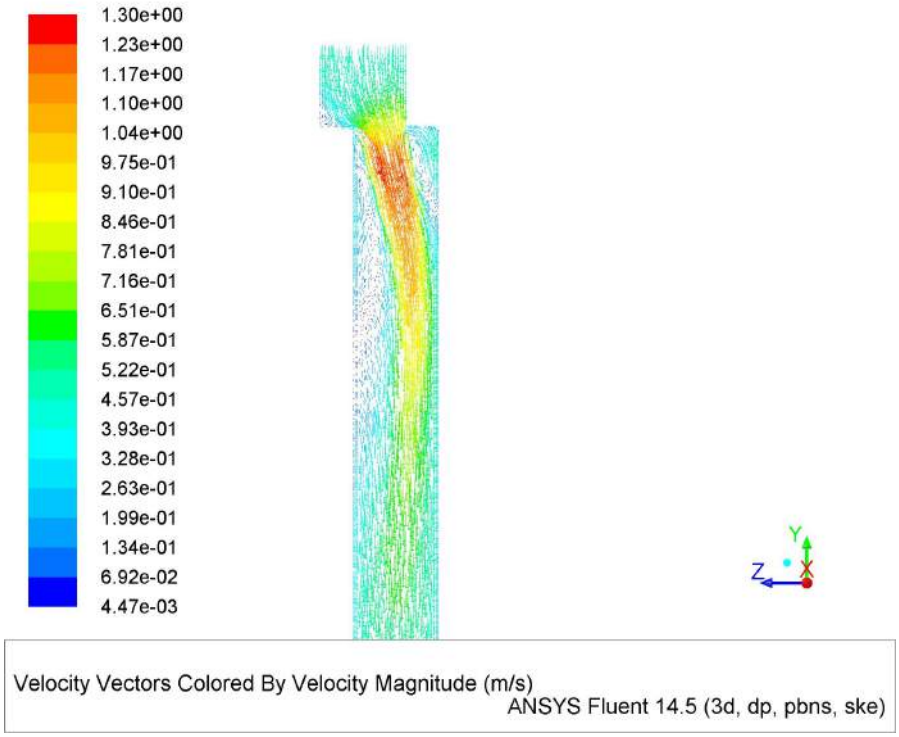

Figure 63 Velocity Vector. Water speed: 0.5m/s, slide gate opening: 61.9%

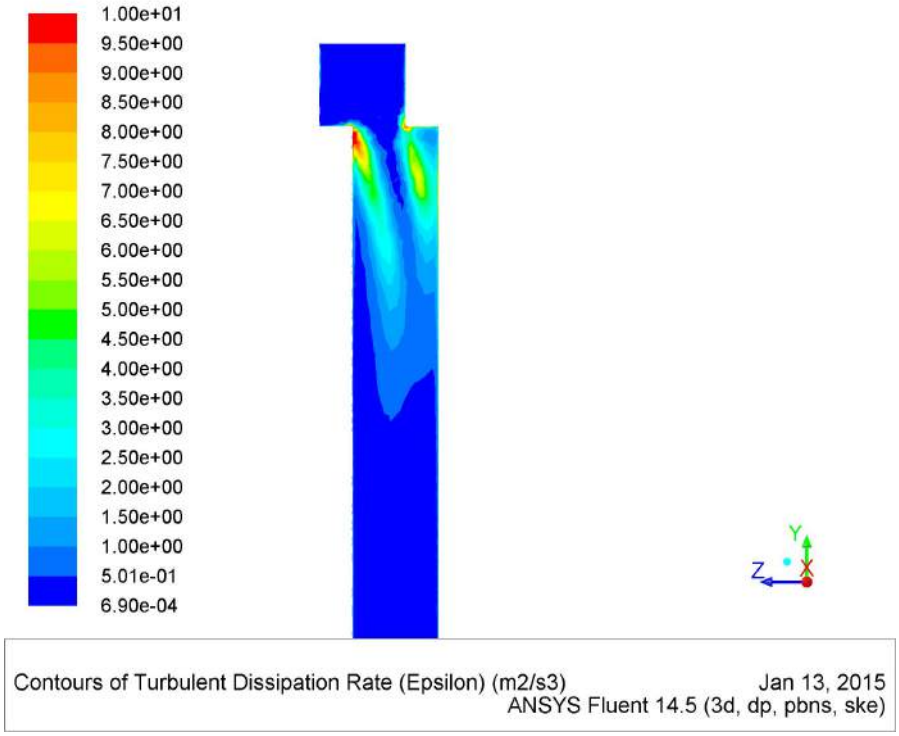

Figure 64 Turbulent Dissipation Rate Contour. Water speed: 0.5m/s, slide gate opening: 61.9%

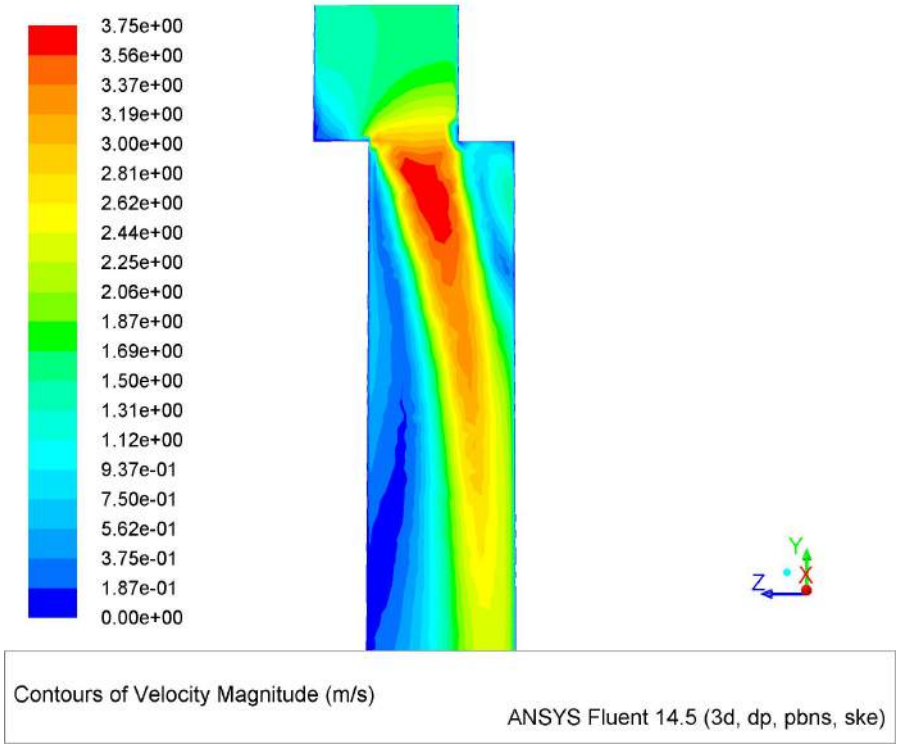

Figure 65 Velocity Contour. Water speed: 1.5m/s, slide gate opening: 61.9%

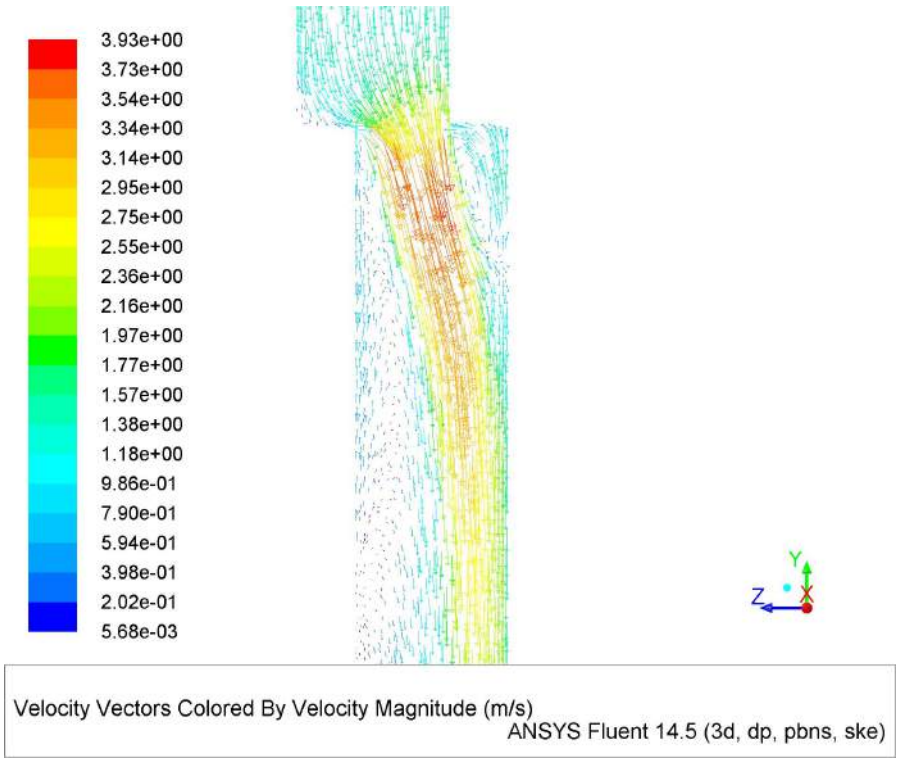

Figure 66 Velocity Vector. Water speed: 1.5m/s, slide gate opening: 61.9%

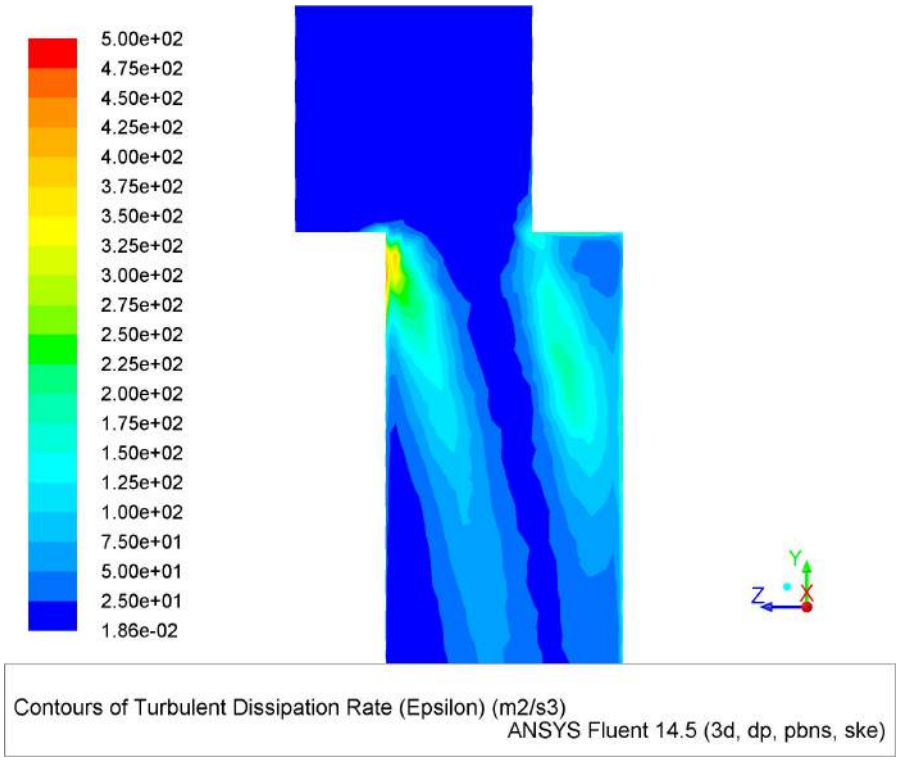

Figure 67 Turbulent Dissipation Rate Contour. Water speed: 1.5m/s, slide gate opening: 61.9%

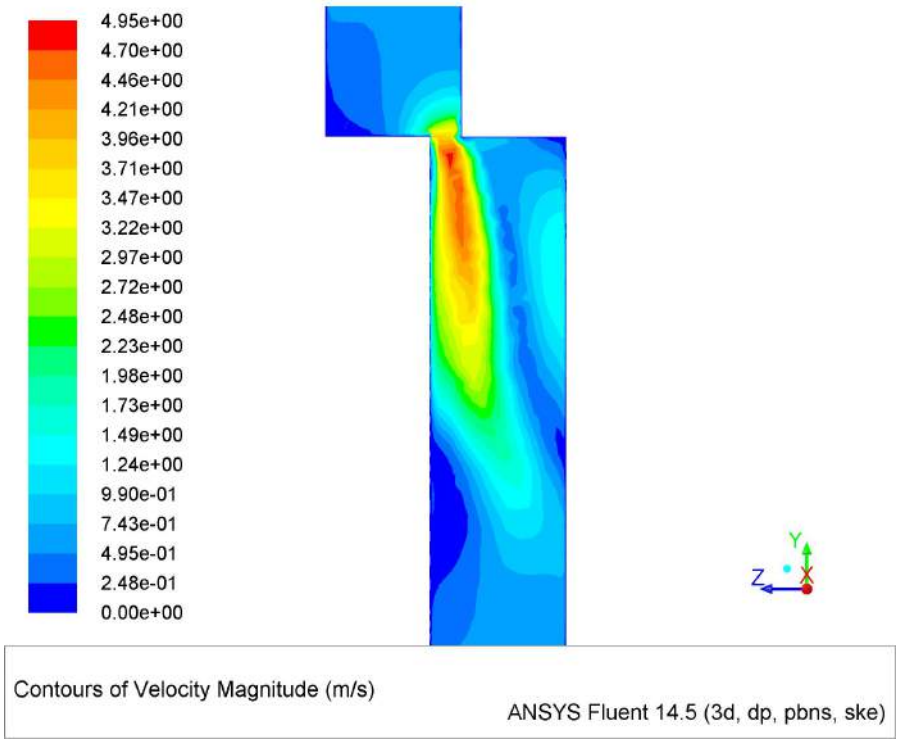

Figure 68 Velocity Contour. Water speed: 0.5m/s, slide gate opening: 23.8%

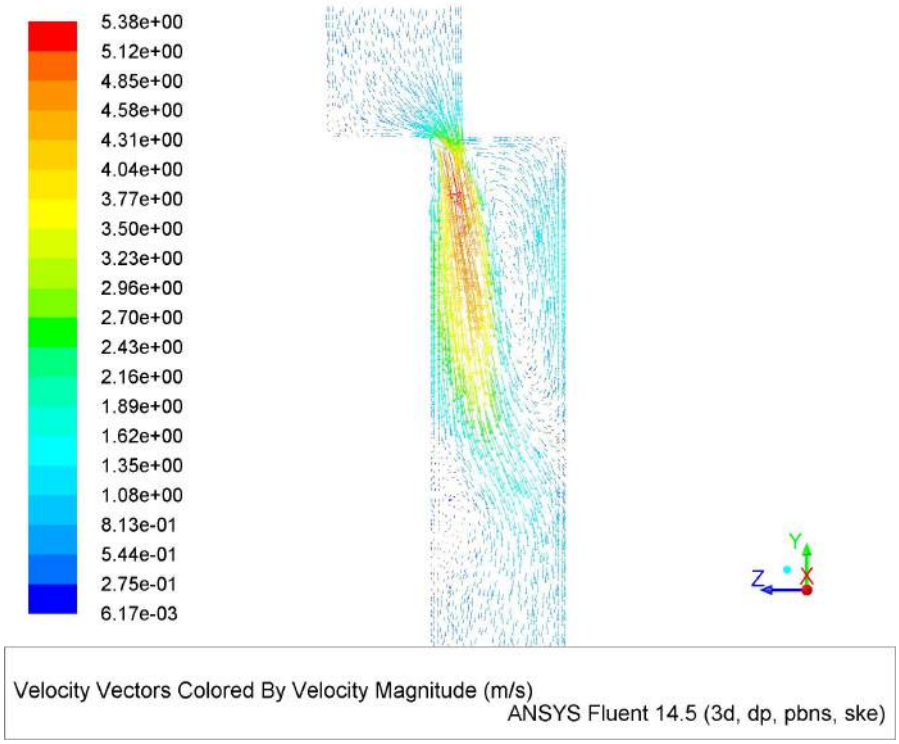

Figure 69 Velocity Vector. Water speed: 0.5m/s, slide gate opening: 23.8%

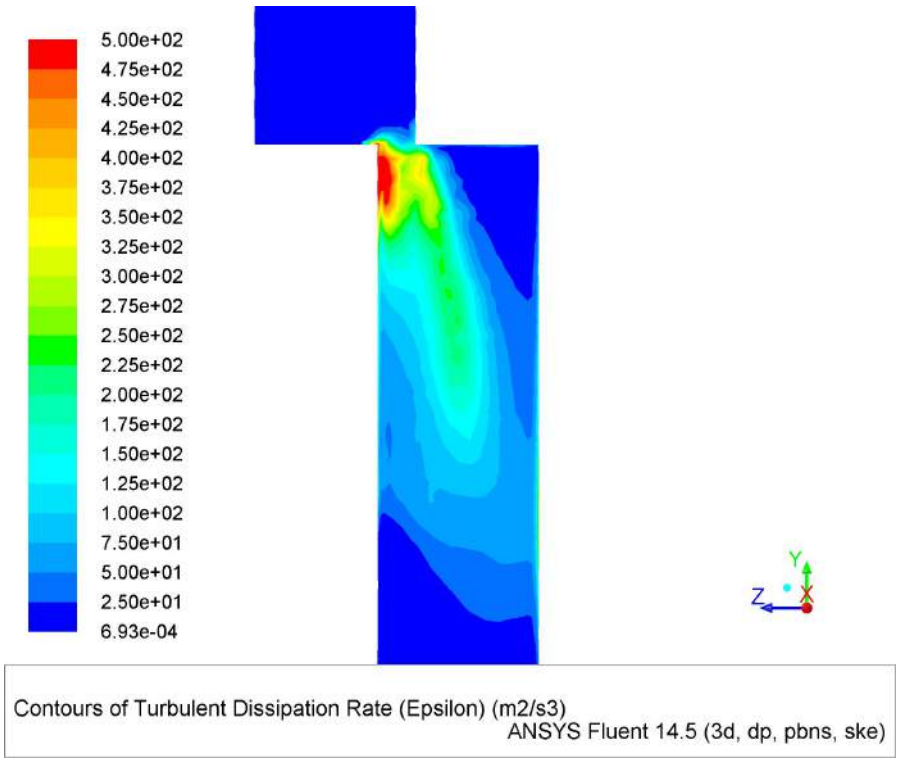

Figure 70 Turbulent Dissipation Rate Contour. Water speed: 0.5m/s, slide gate opening: 23.8%

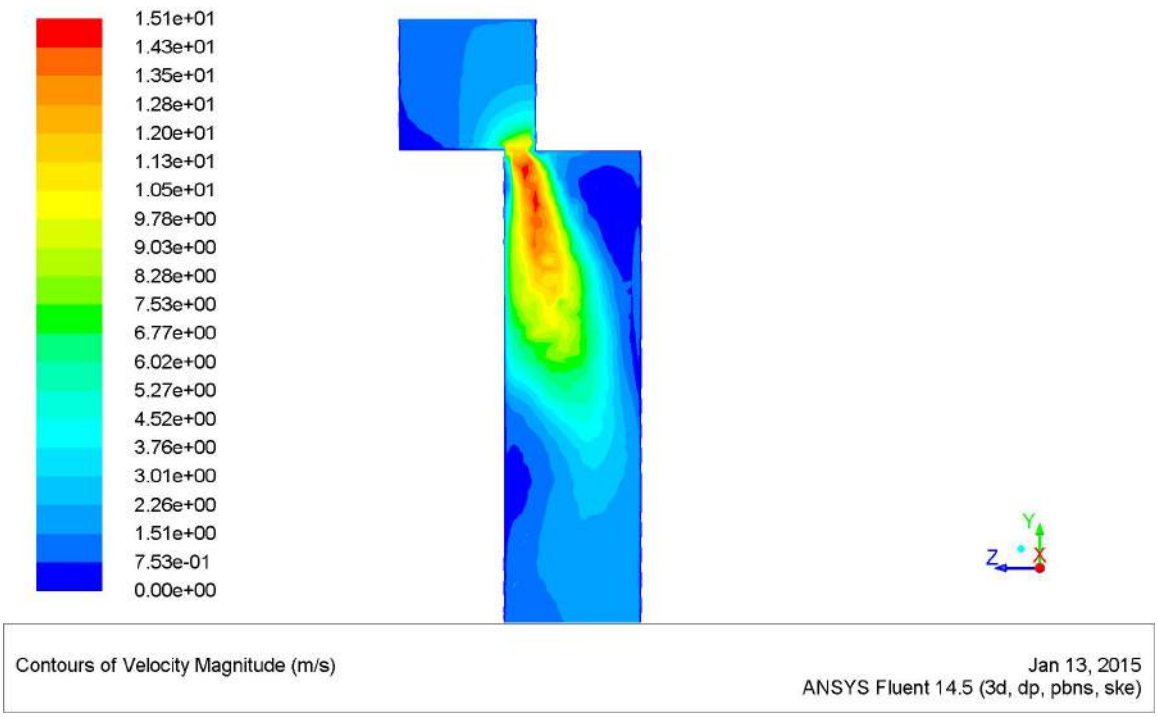

Figure 71 Velocity Contour. Water speed: 1.5m/s, slide gate opening: 23.8%

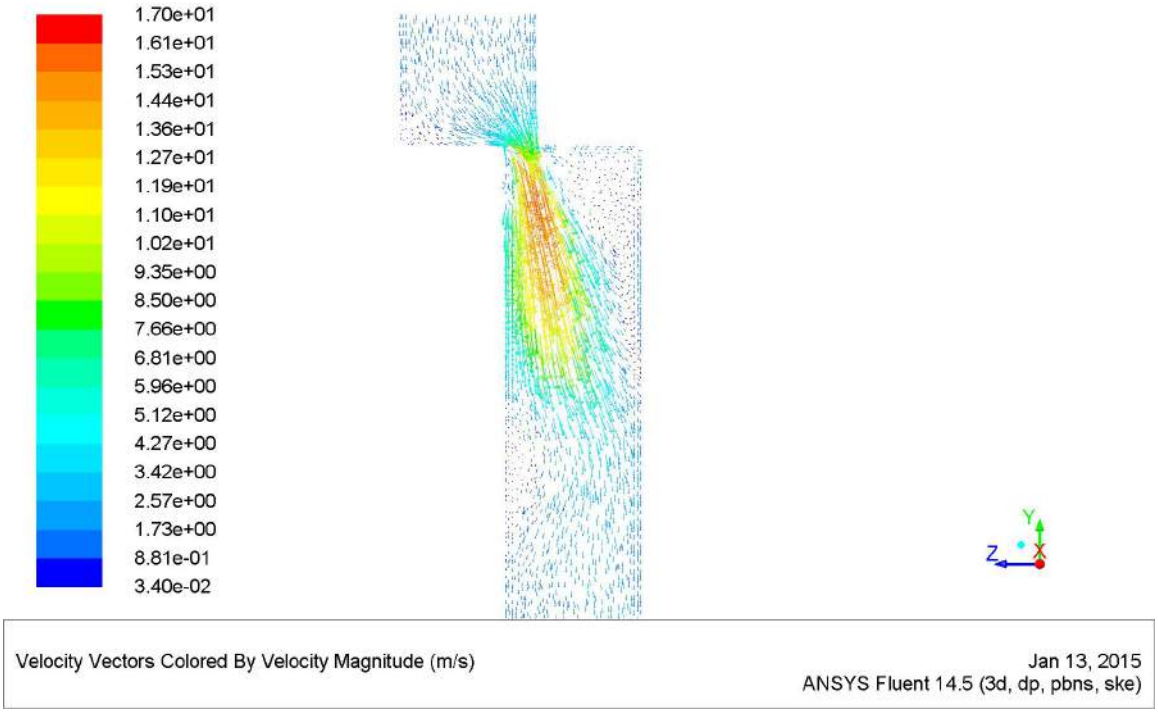

Figure 72 Velocity Vector. Water speed: 1.5m/s, slide gate opening: 23.8%

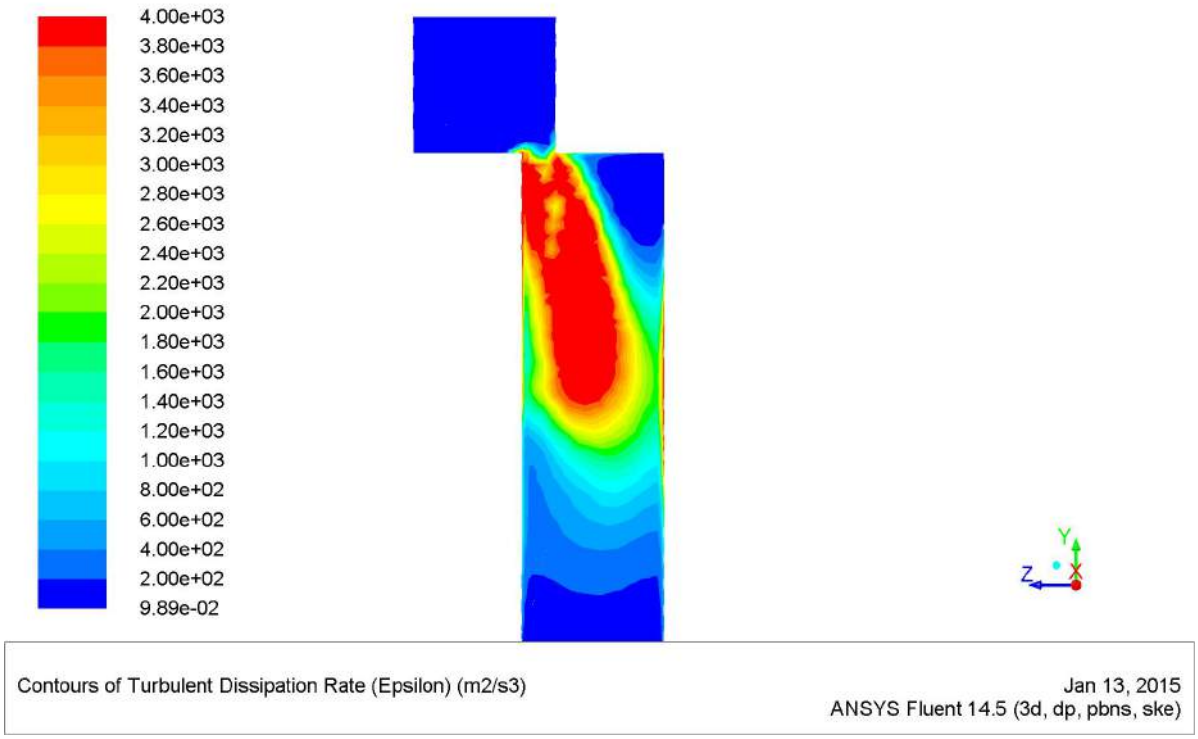

Figure 73 Turbulent Dissipation Rate Contour. Water speed: 1.5m/s, slide gate opening: 23.8%

The CFD results showed that a small slide gate opening ratio promotes the generation of smaller bubbles by altering flow patterns and creating velocity gradients. Experimental results were in good accord with this conclusion.

Figure 74 and Figure 75 showed the results of two sets of experiments with the same set-ups and conditions apart from the slide gate opening ratio. Figure 74 has high slide gate opening ratio of 61.9% and Figure 75 has a low slide gate opening ratio of 23.8%. If one compares the blue lines (1.5m/s water) in Figure 74 and Figure 75, it is obvious that the right tail is smaller in the low slide gate opening, which means more small bubbles and overall smaller average bubble size. If one compares the red lines (1.0m/s water) in in Figure 74 and Figure 75, it was found that the bubble size peak significantly shifts (from 1.5mm to 0.5mm) towards the left in the low slide gate opening, which indicates overall smaller average bubble size. If one compares the black lines (0.5m/s water) in Figure 74 and Figure 75, it is clear that a new peak was formed on the left side, which means smaller bubbles.

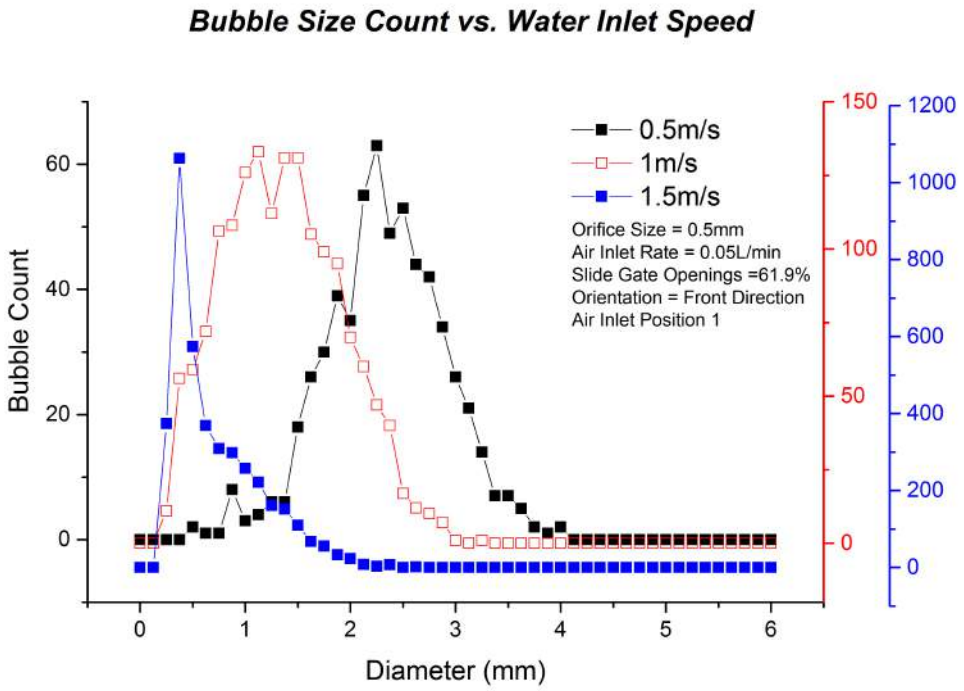

Figure 74 Bubble size vs. water inlet speed. Orifice size: 0.3mm; Air inlet rate: 0.05L/min; Slide gate opening ratio: 61.9%

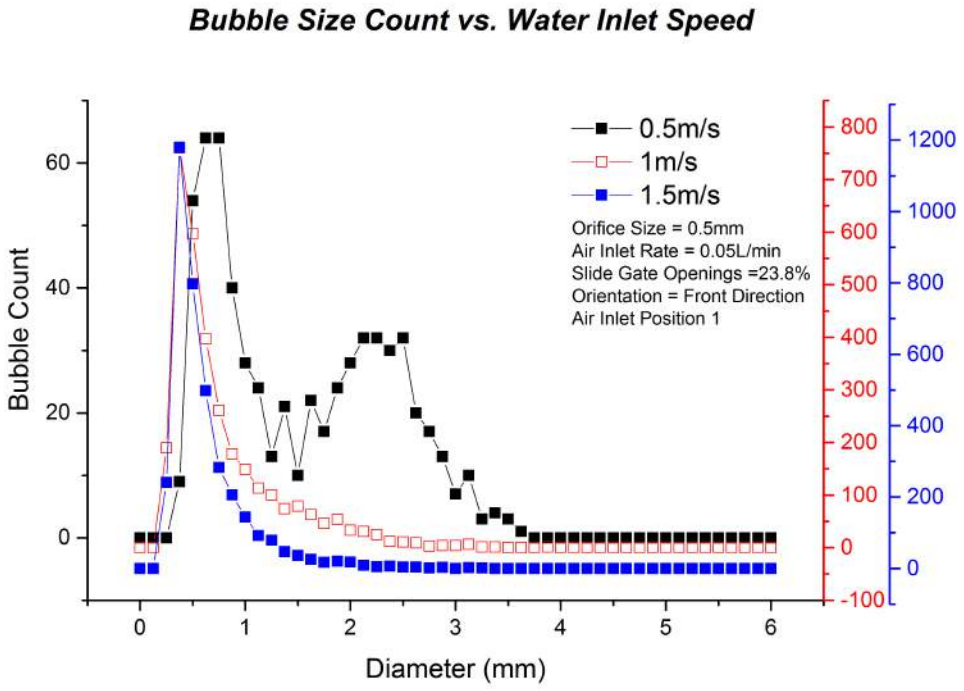

Figure 75 Bubble size vs. water inlet speed. Orifice size: 0.3mm; Air inlet rate: 0.05L/min; Slide gate opening ratio: 61.9%

4.7 Air Injection Orientation vs. Bubble Size

Due to the existence of back flows, air was injected from three different orientations: front, back and side. From the CFD results shown in Section 4.6, it was shown that the front direction had the highest flow speed; the back direction had the lowest flow speed; the flow speed was medium in the side direction.

At this point, it has been demonstrated that the water speed, the slide gate opening ratio and the air inlet rate can affect the bubble size. Therefore 4-D graphs as shown from Figure 77 to Figure 88 could be used to more effectively study the air injection orientation. Take Figure 77 for example, the water speed, the slide gate opening ratio and the air inlet rate are presented on the three axes. Each ball position represents an experimental set. The corresponding bubble size is represented both by the ball size and the color-coding. Both Sauter mean diameter and average bubble diameter were reported.

Figure 76 summarized related graphs shown from Figure 77 to Figure 88 for easier comparison purposes. The three columns from left to right are the front direction, the back direction and the side direction. The top row is the Sauter mean diameter and the bottom row is the average bubble diameter. Figure 76 shows that the bubble sizes are about the same in all three directions. Therefore, in the current experimental setups and conditions, the air injection orientation does not affect the size of bubbles generated.

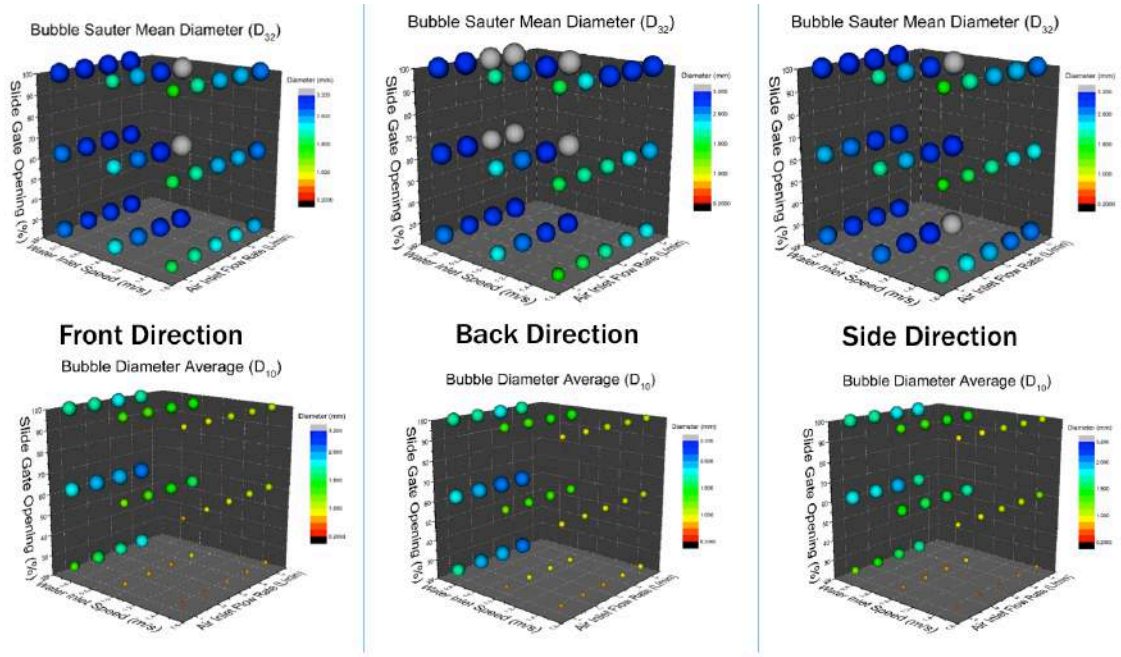

Figure 76 Air Injection Orientation Comparison 0.5mm orifice, Position 1.

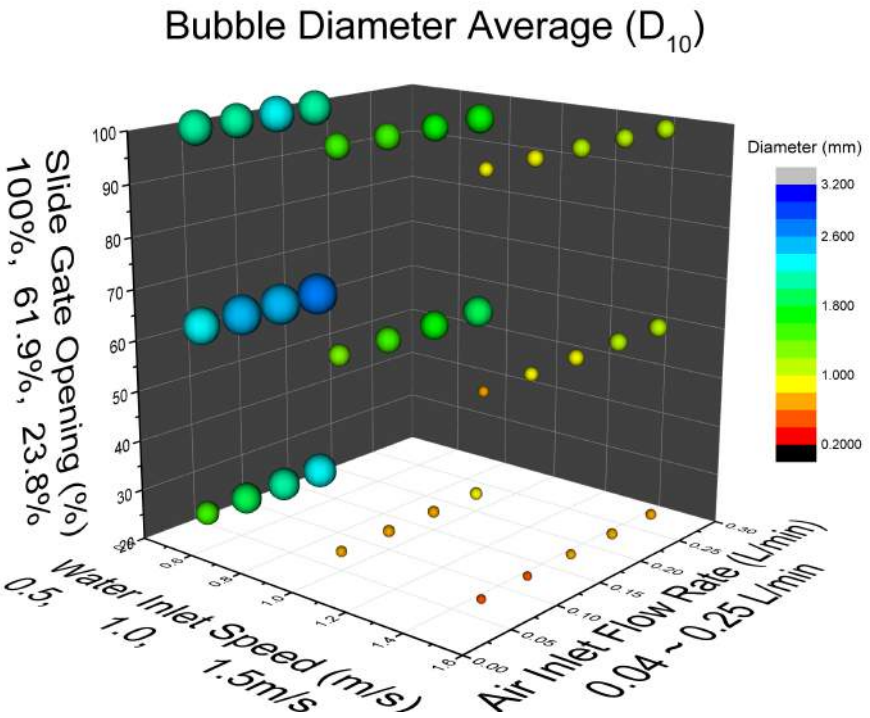

Figure 77 D10 graph 0.5mm Orifice, Front Direction, Position 1

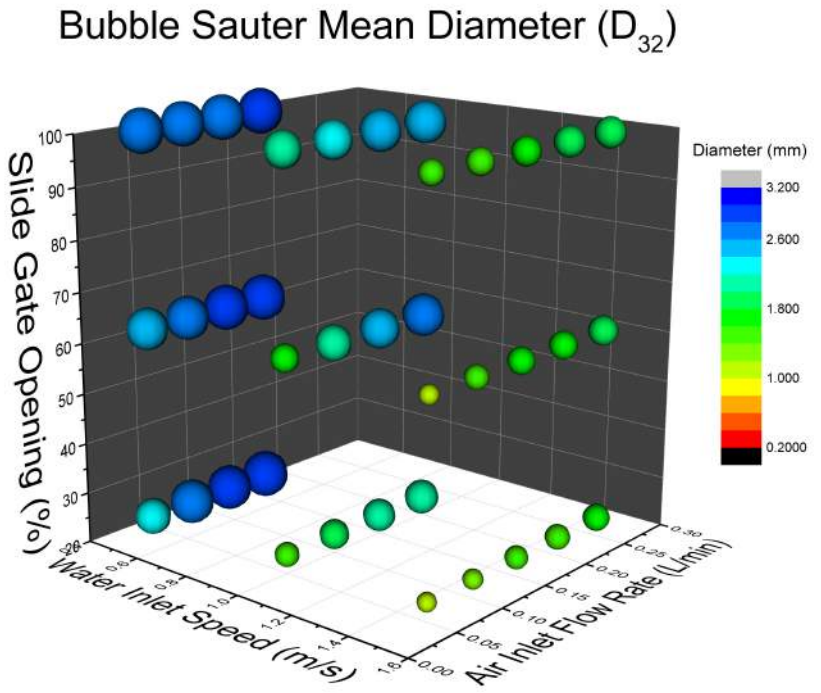

Figure 78 D32 graph 0.5mm Orifice, Front Direction, Position 1

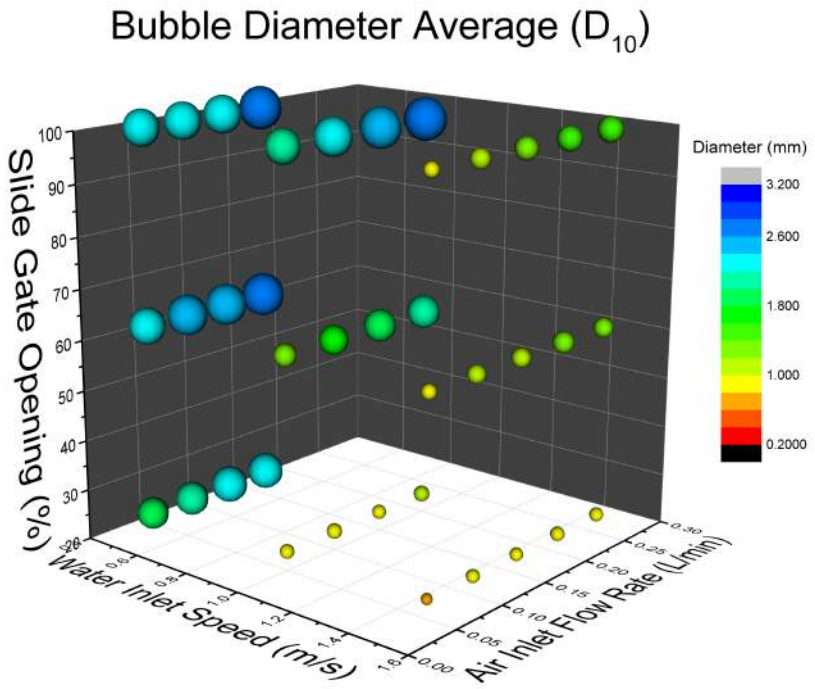

Figure 79 D10 graph 0.5mm Orifice, Front Direction, Position 2

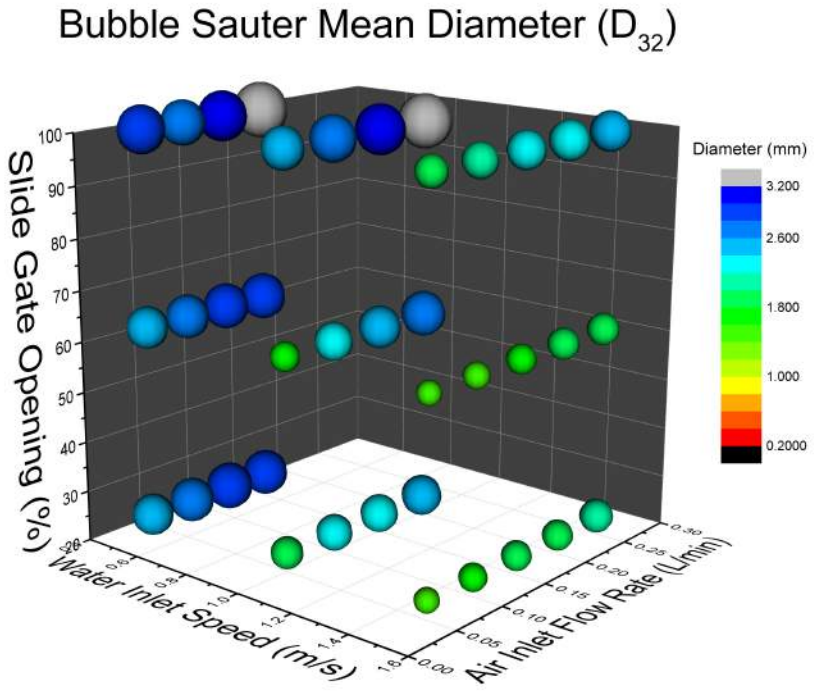

Figure 80 D32 graph 0.5mm Orifice, Front Direction, Position 2

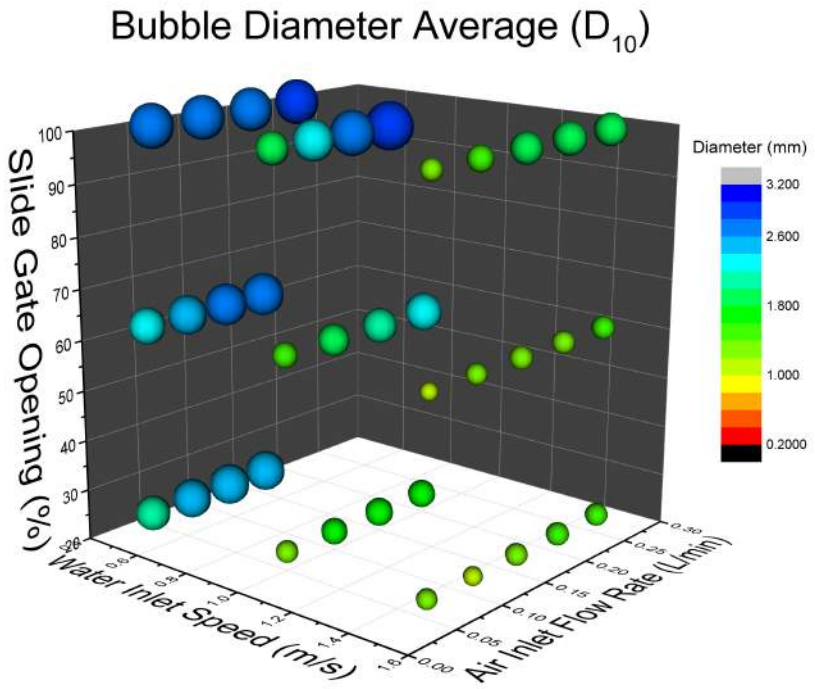

Figure 81 D10 graph 0.5mm Orifice, Front Direction, Position 3

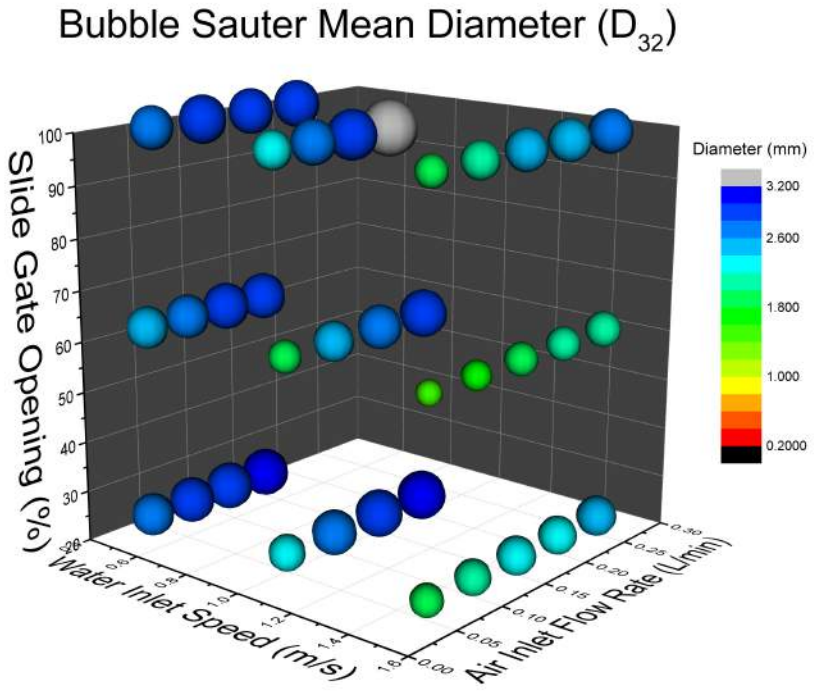

Figure 82 D32 graph 0.5mm Orifice, Front Direction, Position 3

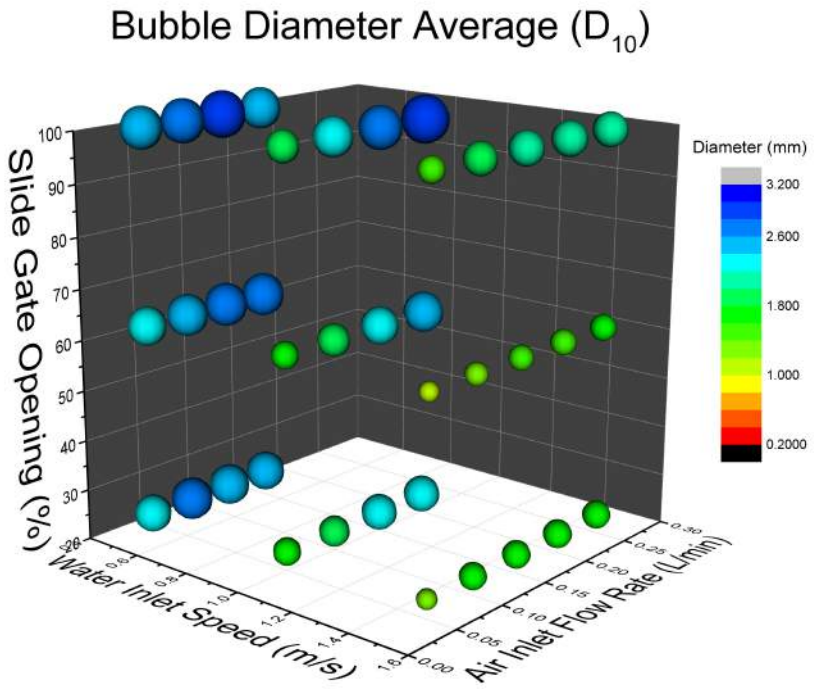

Figure 83 D10 graph 0.5mm Orifice, Front Direction, Position 4

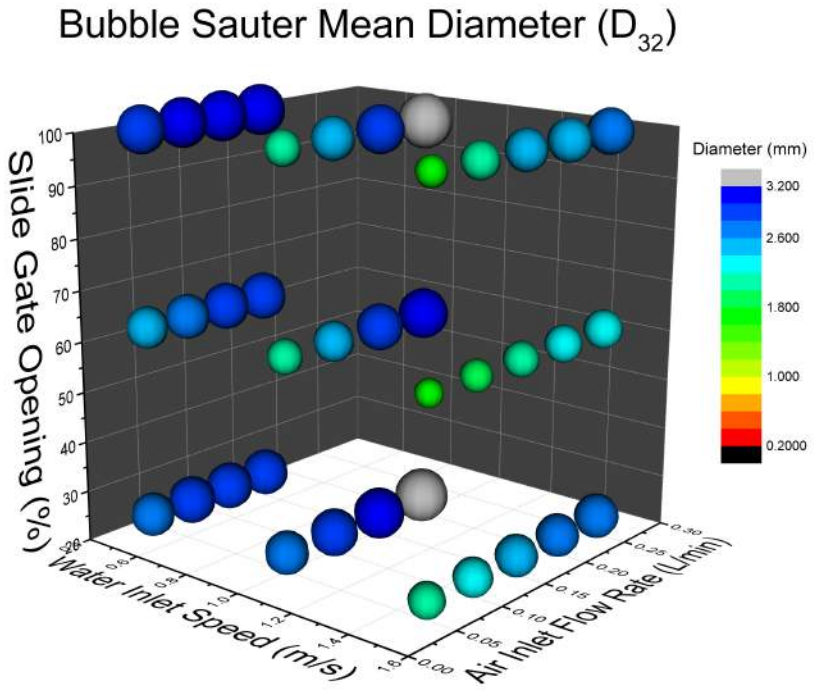

Figure 84 D32 graph 0.5mm Orifice, Front Direction, Position 4

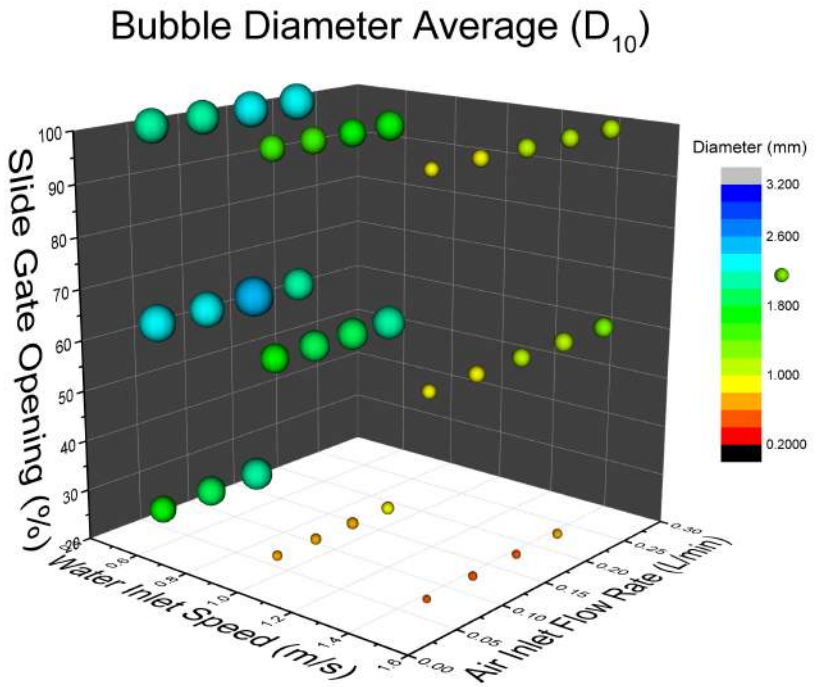

Figure 85 D10 graph 0.5mm Orifice, Back Direction, Position 1

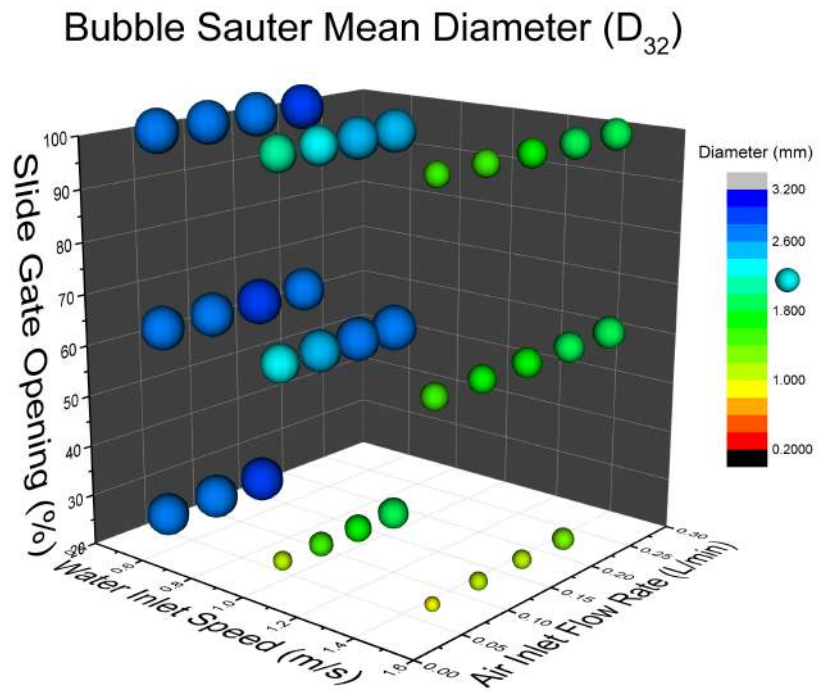

Figure 86 D32 graph 0.5mm Orifice, Back Direction, Position 1

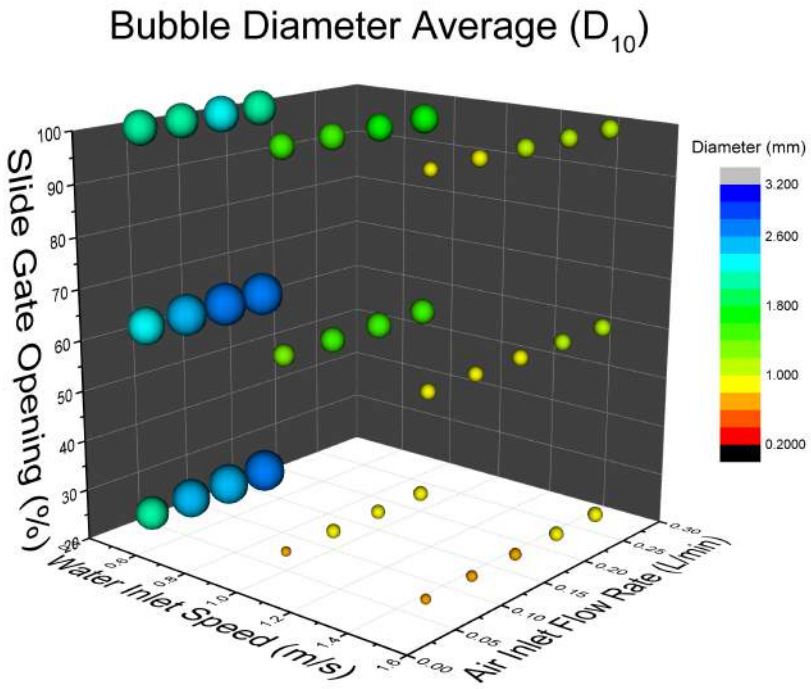

Figure 87 D10 graph 0.5mm Orifice, Side Direction, Position 1

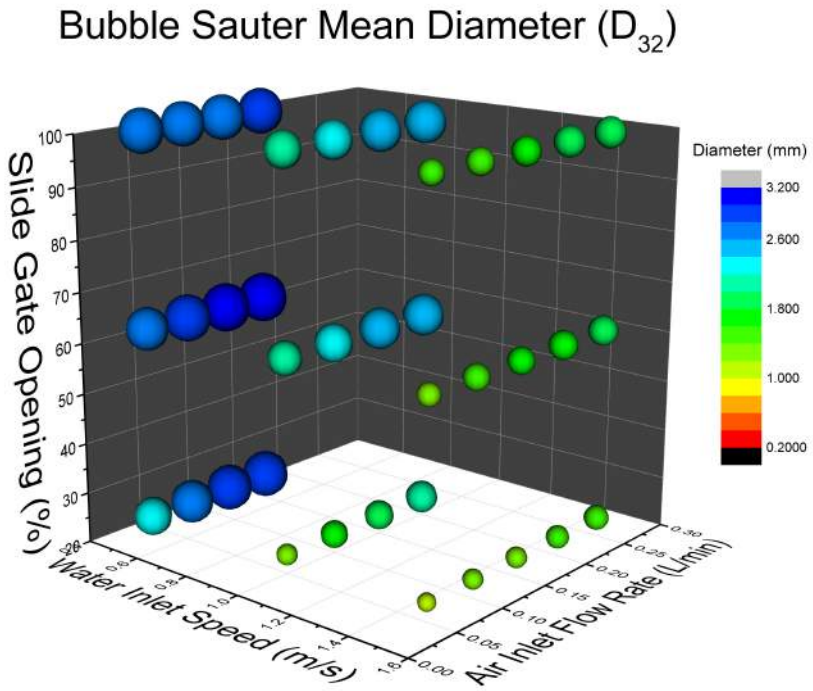

Figure 88 D32 graph 0.5mm Orifice, Side Direction, Position 1

4.8 Distance from the slide gate vs. Bubble Size

As shown in the CFD results (Section 4.6), the turbulence dissipation rate decays quickly down the tube. Four orifice positions were tested in the experiments to study the air injection point distance from the slide gate. As shown in Figure 89, from position 1 to 4 the distance from the slide gate is: 3cm, 5cm, 7cm and 9cm. The exact dimension can be found in Appendix I.

Figure 89 summarizes related graphs shown from Figure 77 to Figure 88 for easier comparison purposes. Clearly the bubble size increases with the distance from the slide gate as the ball size (represents bubble size) increases from position 1 to 4. Therefore, the air injection point should be located as close to the slide gate as possible in order to utilize the turbulence dissipation rate.

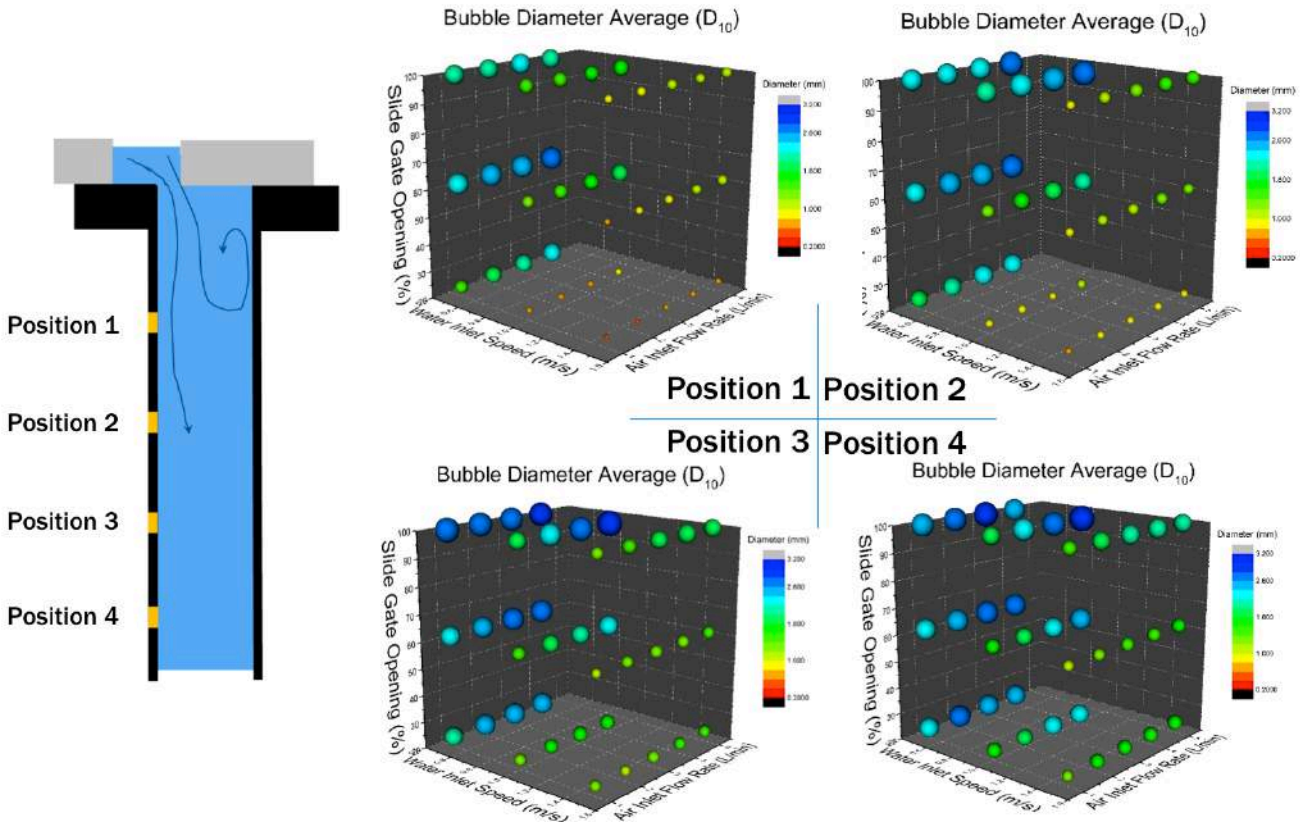

Figure 89 Distance from the slide gate vs. Bubble size 0.5mm Orifice size, Front Direction.

4.9 Bubble birth size in a cross flow

Marshall [76] proposed a semi-empirical model to predict the air bubble birth size (the initial bubble size right after generation) formed from an orifice with water horizontal cross-flow, as shown in Figure 90.

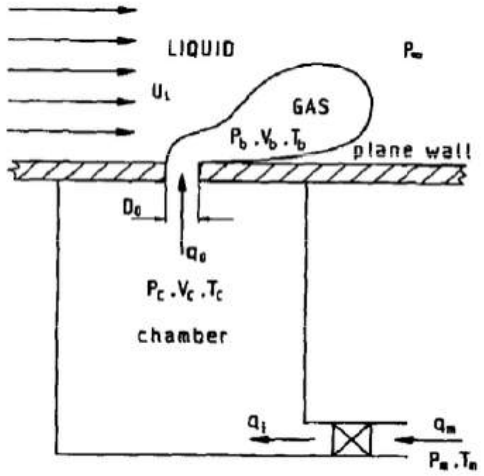

1. Schematic diagram of the liquid cross-flow bubble formation system.

Figure 90 Bubble birth size in a cross flow [76]

The semi-empirical equation for bubble birth radius is:

$$R_b = 0.48 R_{orifice}^{0.826} \left(\frac{U_{air}}{U_{Liquid}} \right)^{0.36}$$

where $R_{orifice}$ is the radius of the orifice, U_{air} is the superficial air inlet speed, and U_{liquid} is the speed of the cross flow.

$$U_{air} = \frac{Q_{air}}{\pi R_{Orifice}^2}$$

Though this study was semi-empirical, the experimental conditions (orifice size, liquid velocity, air inlet rate) are very similar with the conditions carried in the present research. Liu [77] showed that the horizontal bubble formation mechanism (as used in Marshall[76]) does not vary too much from the vertical bubble formation mechanism (the method in the current research). Therefore, it is reasonable to use this model to calculate the predicted birth size of bubbles (shown in Figure 91).

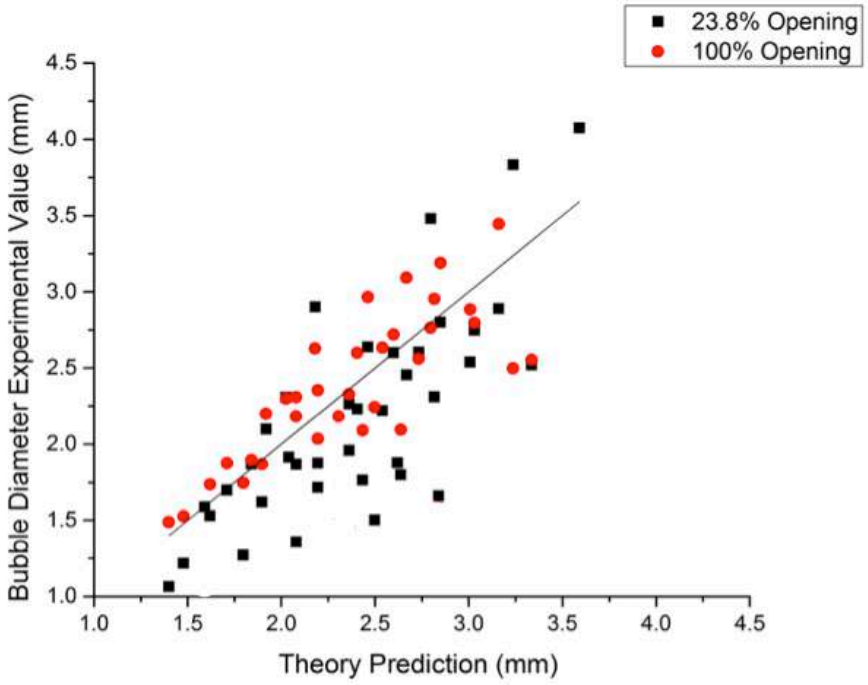

Figure 91 Bubble size comparison: Experimental results vs. Theory prediction. The solid line is 1:1 line.

Figure 91 shows the bubble size comparison between the present experimental data and the theory prediction based on Marshall's equation [76]. The black solid line is the 1:1 line. When data points lie on the 1:1 line, it means the experimental data matches well with the theory prediction. When the data points fall below the 1:1 line, it means the bubble size got from experimental results are smaller than the theory predicts.

From Figure 91, it is obvious that for a 100% slide gate opening (red dots), where there was nearly zero velocity gradients and zero turbulence dissipation rate, the data points fall nicely around the 1:1 line. This indicates the model from Marshall [76] is suitable to estimate the size of bubbles generated.

However, for a 23.8% slide gate opening (black dots), where there were usually strong velocity gradients with an accompanying high turbulence dissipation rate, a large portion of the data points fall below the 1:1 line. This means the bubbles went through break-up processes after being form.

4.10 Critical bubble size under turbulent conditions

Several studies have shown that bubble break-up depends on the turbulent dissipation rate [39-41]. The mechanism is explained as below.

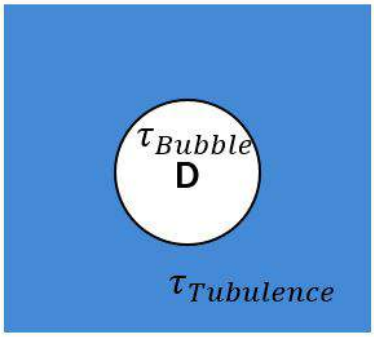

Figure 92 Schematic diagram of an air bubble in water

Bubble break-up fundamentally is caused by severe bubble surface deformations. Two forces determine the degree of bubble surface deformation: a confinement force provided by the surface tension and a deformation force provided by the turbulence stresses.

Martínez-Bazán et al. [42] showed that the surface tension of the air-water interface acts as a confinement force. The minimum energy required to deform a bubble of size D is:

$$E_{min} = \pi\sigma D^2 \tag{7}$$

Therefore, the surface restoring pressure according to [42] is :

$$\tau_{bubble}(D) = \frac{6E_{min}}{\pi D^3} = \frac{6\sigma}{D} \tag{8}$$

Under turbulent conditions, where the Reynolds number is large, viscous forces can be neglected. The determining factor in bubble break up is the dynamic pressure caused by the velocity changes over distances in the order of the bubble diameter [39]. The deformation pressure can be calculated as [42]:

$$\tau_{turbulence}(D) = \frac{1}{2}\rho\overline{\Delta u^2} \tag{9}$$

In turbulent conditions, when the bubble is larger than the Kolmogorov microscale of turbulence (defined as η in following equation), Kolmogorov [78] summarized that the eddies causing the bubble splitting are isotropic and that the kinetic

energy is independent of the viscosity and follows the energy distribution law of Kolmogorov.

$$\eta = \left(\frac{\nu^3}{\varepsilon}\right)^{1/4} \tag{10}$$

Due to the kinematic viscosity of water being very low, 1.12E-6 m^2/s, even with a very small energy dissipation rate, the Kolmogorov microscale (η) is in the order of a few microns. This is much smaller than the bubbles observed from the experiments. According to the energy distribution law of Kolmogorov [78], the velocity fluctuations between two points can be estimated as:

$$\overline{\Delta u^2} = \beta(\varepsilon D)^{2/3} \tag{11}$$

Plug Equation(11) into Equation(9), the deformation pressure can be expressed as:

$$\tau_{turbulence}(D) = \frac{1}{2}\rho\overline{\Delta u^2} = \frac{1}{2}\rho\beta(\varepsilon D)^{2/3} \tag{12}$$

When the confinement force and deformation force equal each other, the critical bubble diameter is reached. Namely for any cases where the deformation force is larger than the confinement force, the bubbles will breakup towards the critical size.

By equating the restoring pressure equation (Equation(8)) and the deformation pressure equation (Equation (12)) the following equation can be derived:

$$D_c = \left(\frac{12\sigma}{\rho\beta}\right)^{3/5} \varepsilon^{-2/5} \tag{13}$$

From Batchler [79], the β value is 8.2, and the equation above can be written as:

$$D_c = 1.26\left(\frac{\sigma}{\rho}\right)^{3/5} \varepsilon^{-2/5} \tag{14}$$

An alternative approach is to solve the critical bubble diameter by invoking a critical Weber number. The Weber number (We) measures the ratio of the inertia forces to the surface tension forces of a bubble in a liquid.

$$We = \frac{\rho v^2 l}{\sigma} \tag{15}$$

When an air bubble is in a turbulent water condition, the turbulent stresses around the air bubble will deform the bubble surface. When the turbulent stresses are strong enough, namely when a critical Weber number is reached, the bubble will be distorted

and will then break. The critical bubble diameter (D_c) can be calculated from the critical Weber number [41].

A study by Sevik et al. [39] showed that the critical Weber number is 1.26. This agrees with the previous equation derived.

$$(We)_{ct} = \left[D_B \left(\frac{\rho}{\sigma}\right)^{3/5} \varepsilon^{2/5} \right]^{5/3} = 1.26 \tag{16}$$

Now we can calculate the critical bubble size in water for a given turbulence dissipation rate based on Equation (14).

Figure 93 and Figure 94 show the calculated results for the critical bubble sizes in water for different turbulence dissipation rates in water. In Figure 93, the turbulence dissipation rate (ε) varies from 0 to 30 m^2/s^3. In Figure 94, the turbulence dissipation rate (ε) varies from 100 to 1600 m^2/s^3.

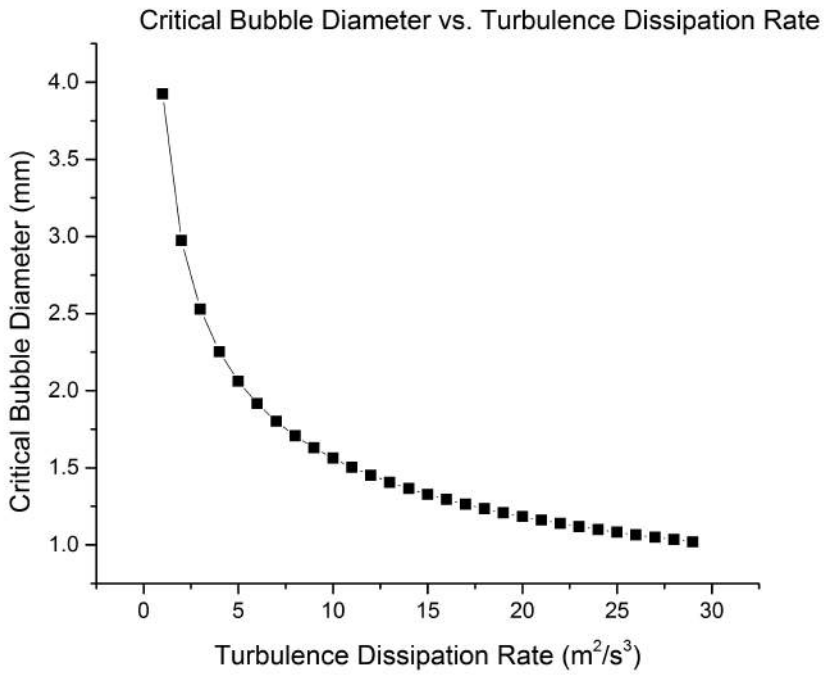

Figure 93 Critical bubble diameter in Water vs. Turbulence dissipation rate (ε from 0 to 30)

As shown in Figure 93 and Figure 94, the critical bubble size decreases with an increase in turbulence dissipation rate within the liquid. As discussed above, for a given condition of turbulence, any bubble with a size larger than the corresponding critical size, will break up to approach the critical bubble size. This explains why the data points fall

below 1:1 line in Figure 91 for the 23.8% slide gate opening. Namely, the turbulence dissipation rate was high and the bubble birth size was larger than the critical bubble size. This causes the original birth size bubbles to break down into smaller bubbles.

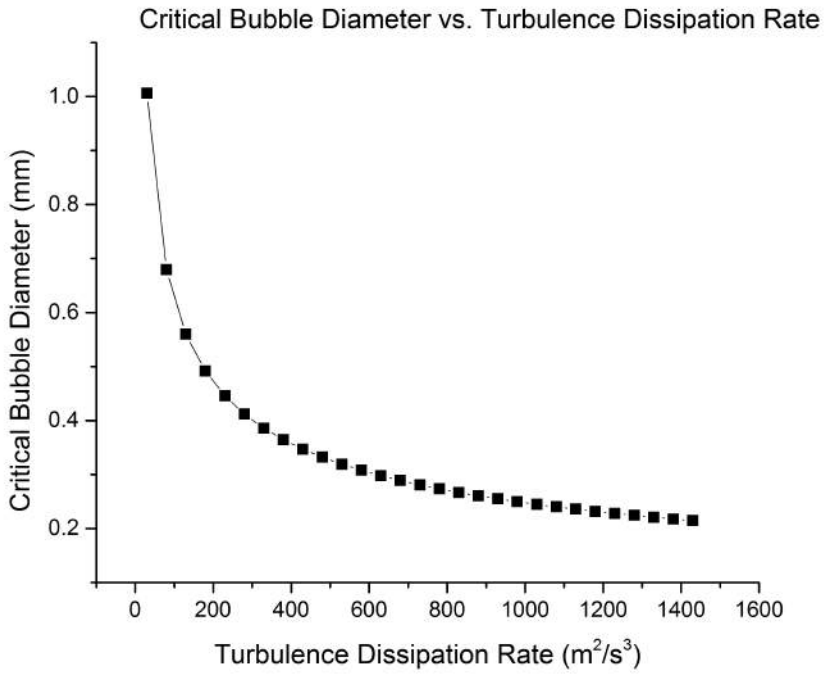

Figure 94 Critical bubble diameter in Water vs. Turbulence dissipation rate (ε from 100 to 1600)

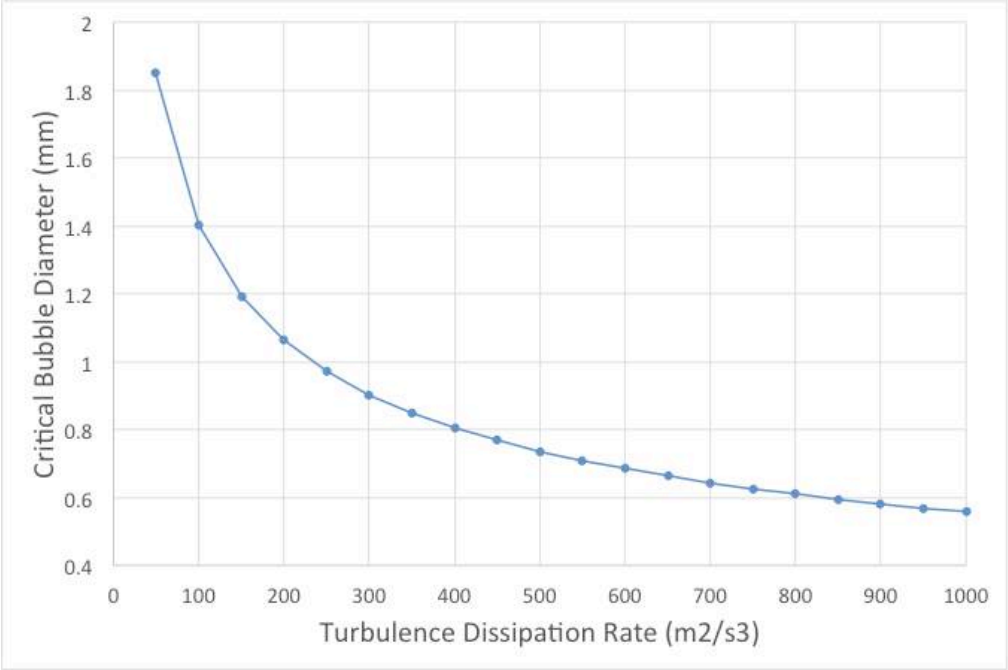

Figure 95 Critical bubble diameter in Liquid Steel vs. Turbulence dissipation rate

The critical bubble diameter in liquid steel (density: 7000 kg/m^3, surface tension: 1.8 N/m) was calculated using Equation (14) and the results are shown in Figure 95. Because of the high surface tension of liquid steel, comparing with water system, it is clear that higher turbulence dissipation rate is required to achieve low critical bubble size.

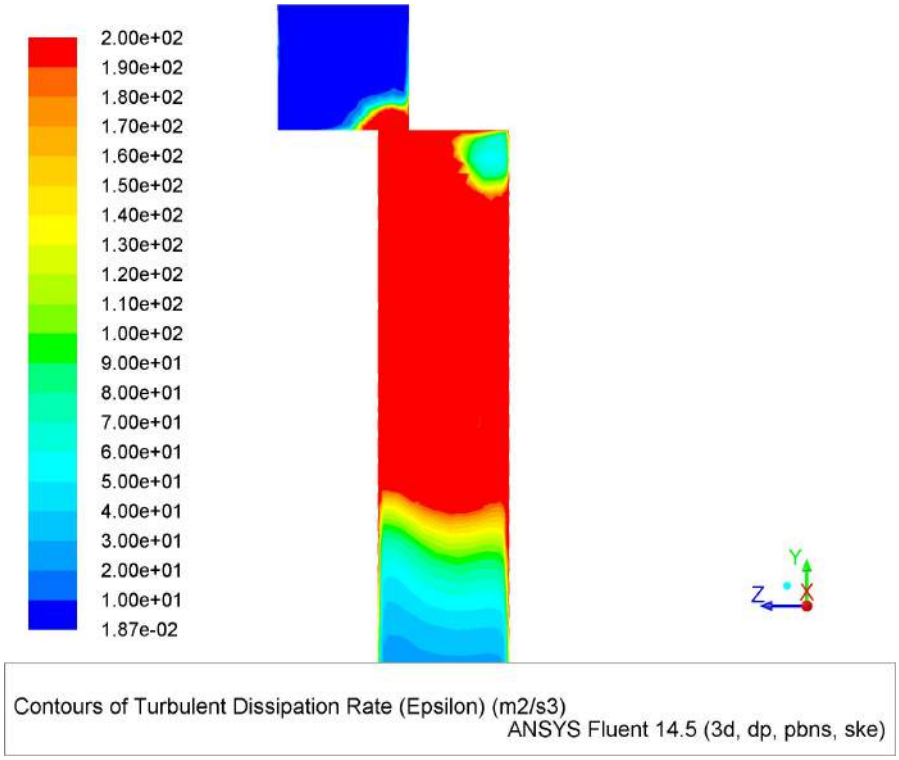

Figure 96 Turbulence dissipation rate contour. Water speed: 1.5m/s Slide gate opening 23.8% the red region are above 200.

Figure 96 shows the turbulence dissipation rate contour graph for experimental conditions of high water speed (1.5m/s) with a low slide gate opening ratio (23.8%), which is the optimal condition to generate small bubbles. The turbulence dissipation rate is higher than 200 m^2/s^3 in the red marked region.

From Figure 94, one can read that the critical bubble size for a turbulence dissipation rate of 200m^2/s^3 is 0.45mm. Theoretically, any bubble size larger than the critical value, if it stays in the turbulent condition long enough, will be break down to the critical size.

However, Figure 77 shows that the final bubble size did not reached the critical bubble size of 0.4mm. This is because the bubbles were not to exposed to the high turbulence dissipation rate region long enough. Especially considering the water speed

was as high as 1.5m/s and the 200+ m^2/s^3 turbulence dissipation rate region was less than 10cm in length.

To quantitatively predict the final bubble size generated from break up of birth size bubbles caused by turbulence will be extremely hard, as the bubbles can break down into any size between the critical size and the birth size.

Now we can answer the question of how to make target size small bubbles in the ladle shroud:

1. Use a high fluid flow, and a low slide gate opening to create high turbulence dissipation rate.
2. Use a low airflow rate, and a small orifice, to maintain a low bubble birth size.
3. Inject the air close to the slide gate to use the local high turbulence dissipation rate there.
4. Make sure the target bubble size value falls between the critical bubble size and the birth bubble size.

Chapter 5. Conclusions:

The following conclusions could be drawn based on the current study:

1. Small bubbles in the range 0.5mm to 4.5mm diameter can be generated by injecting air into the ladle shroud, immediately below the slide gate.

2. The water speed in the ladle shroud and slide gate opening ratio, determined the turbulent conditions, which in turn determined the critical bubble size. High water speeds and low slide gate opening ratios are recommended for generating small bubbles.

3. The turbulence dissipation rate increases with the water speed in the ladle shroud and decreases with the slide gate opening ratio.

4. Since the turbulence dissipation rate decays quickly down the ladle shroud, the gas injection point should be set close to the slide gate.

5. Bubble size increases with air injection rate. A small air injection rate is crucial in order to create small bubbles.

6. Orifice size does not exhibit a very strong correlation with the average bubble size. However, a small orifice is recommended when the water speed is high and air injection rate is low.

7. Despite the speed of water in the backflow region caused by the partially opened slide gate is lower than the mean water velocity, the orientation direction of the air injection point does not a show strong correlation with the average size of bubbles generated.

8. The final average size of bubbles generated is a function of the initial bubble birth size and the turbulent conditions it then experiences.

Appendix I

1. Tubes for the ladle shroud model

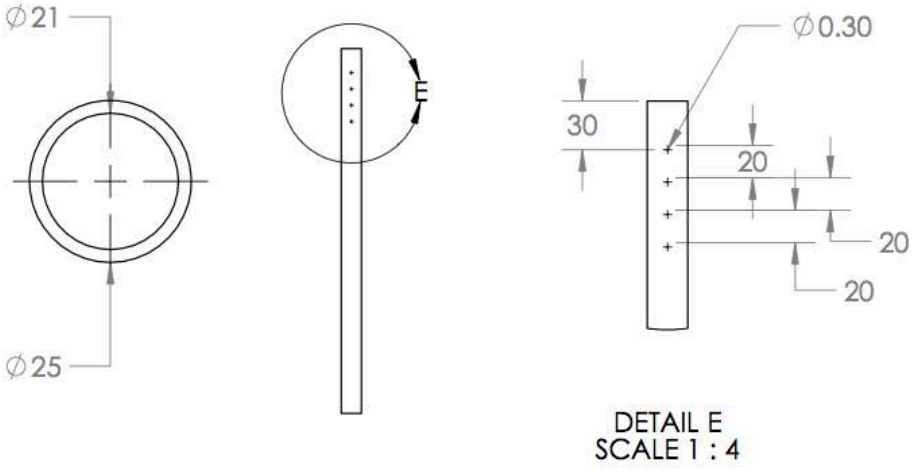

2. Top flange for the ladle shroud model

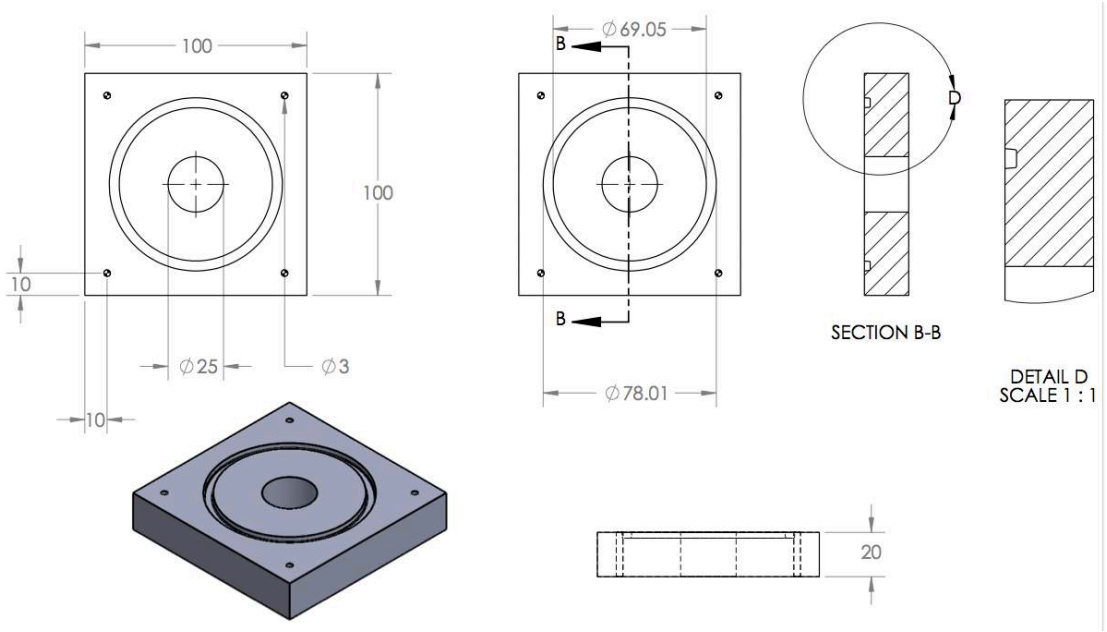

3. Connectors for the ladle shroud model

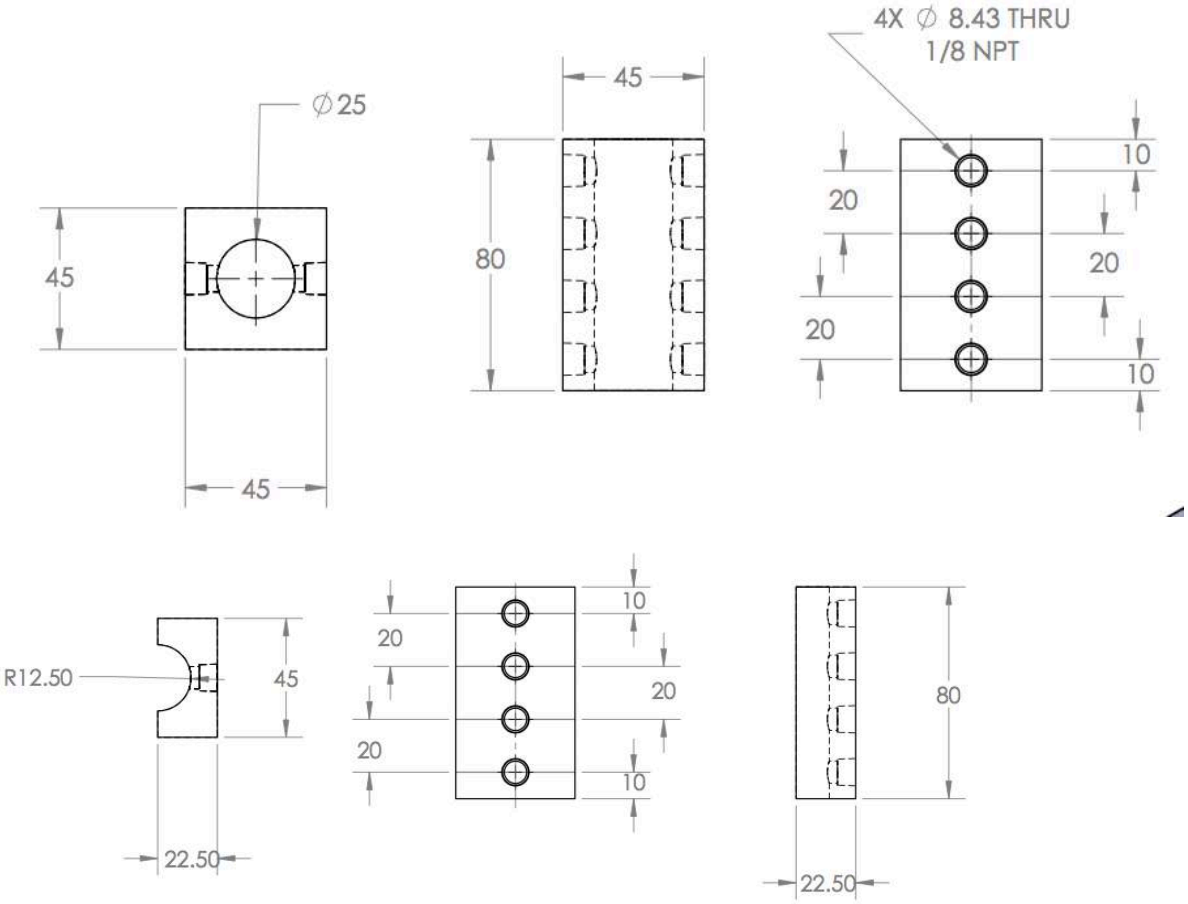

4. Final assemble for the ladle shroud model

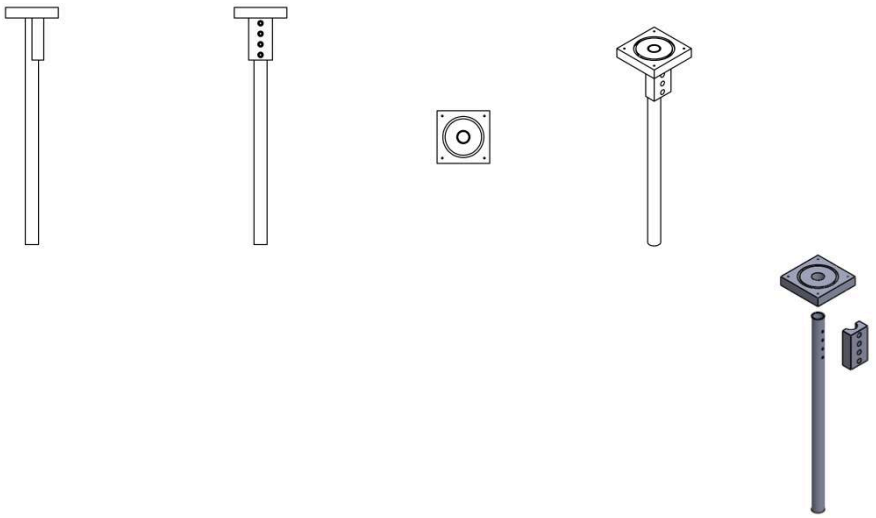

Appendix II

Slide gate plate design

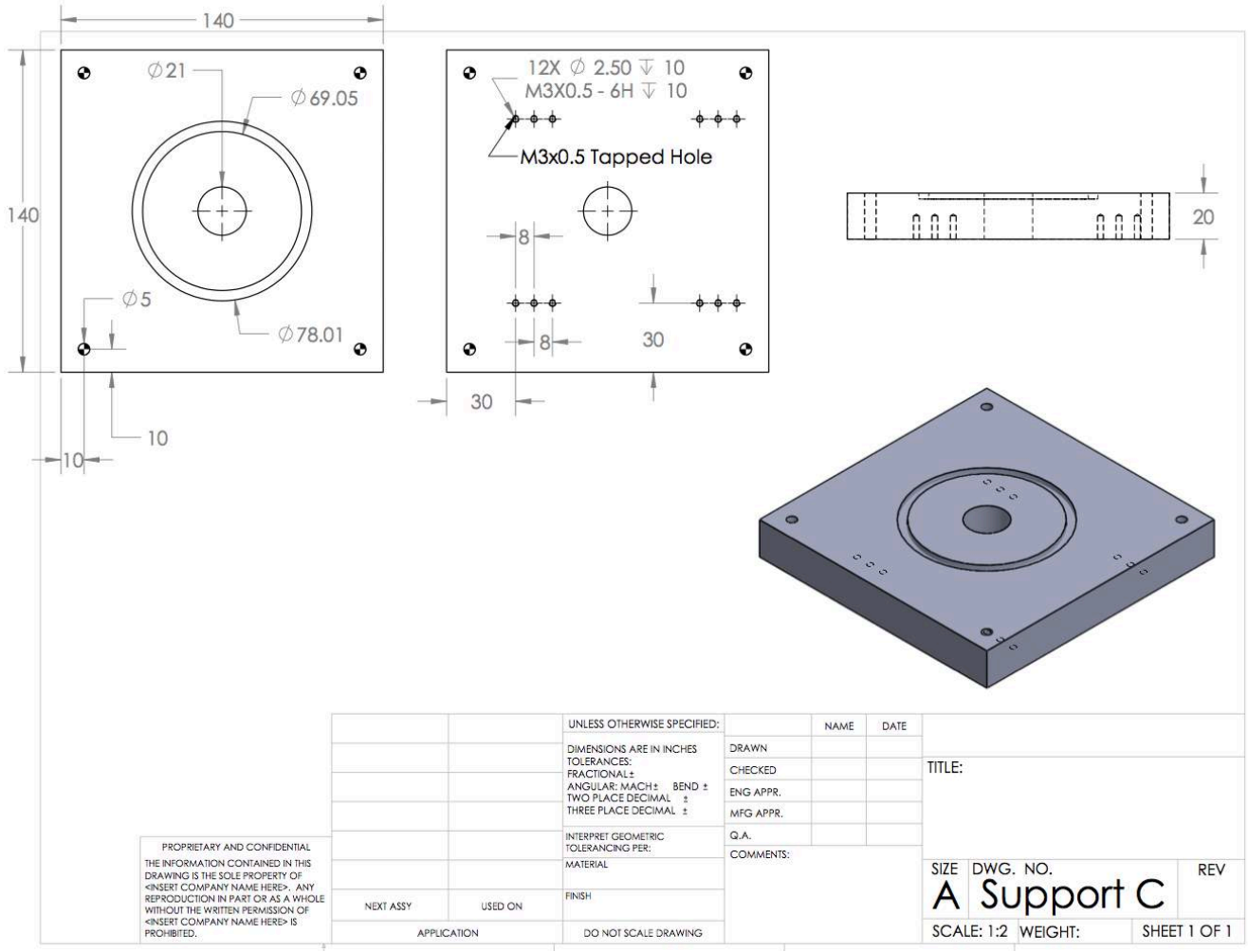

Appendix III

**********This is the ImageJ macrocode**********

```
// Author: Roger Ren
// Last Edit Date: 2014-June-01
// Macro Purposes: This Macro is designed for analyzing photo data in batch automatically.
// Contact Info: xinyu.ren@mail.mcgill.ca
	Dir_w = "F:\\Experiments Photos\\Data Process\\Results\\";
	extension = "JPG";
	Mother_Folder =  "F:\\Experiments Photos\\Good 752_1110\\REP 768_783\\"
	function BBB () {
		x = S_Num  ;
		y = E_Num + 1;
		for (z=x; z<y; z++) {
		Dir_r = Mother_Folder + z + "/";
		// Get folder name from directory
		n = lastIndexOf(Dir_r, "/");
		dir = substring(Dir_r, 0, n-1);
		m = lastIndexOf(dir, "\\");
		TestName = substring(Dir_r, m+1, n);
		//Process Photos
		run("Clear Results");
		j = 0;
		list = getFileList(Dir_r);
		for (i=0; i<list.length; i++)  {
			if (endsWith(list[i], extension) == 1) {
			open(Dir_r + list[i]);
			run("8-bit");
			setThreshold(0, thold);
		if (j==0){
```

```
                run("Set Scale...", "distance=" + Cal + " known=1 pixel=1 unit=mm global");
                j = 1;
                }
                run("Set Measurements...", "area centroid center fit circularity display invert redirect=None decimal=3");
                run("Analyze Particles...", "size=" + min_area + "-" + max_area + "circularity=" + Circ + "-1.00 show=Outlines exclude clear include in_situ");
                close();
                }
                }
                saveAs("Results", Dir_w + z + ".txt");
                }
        }

////////////////////////////////////
S_Num = 115;
E_Num = 126;
Cal = 72.50;
Circ = 0.70;
min_area = 0.1;
max_area = 29;
thold = 170;
        BBB ();
////////////////////////////////////
```

Appendix IV

```
**************************This is the Excel macrocode**********************
''''''''''''''''''''''''''''''''''''''''
 Author: Roger Ren
''''''''''''''''''''''''''''''''''''''''
 Last Edit Date: 2014-June-01
''''''''''''''''''''''''''''''''''''''''
Macro Purposes: This Macro is designed for analyzing photo data in batch automatically.
''''''''''''''''''''''''''''''''''''''''
Contact Info: xinyu.ren@mail.mcgill.ca
Sub Button1_Click()
Dim FilePath As String
Dim strLine As String
Dim i As Integer
Dim j As Integer
Dim k As Integer
Dim rogerArray() As String
Worksheets.Add().Name = "Summary"
Sheets("Summary").Range("A2").Value = "D32"
Sheets("Summary").Range("A3").Value = "D10"
k = Sheets("Start").Range("B2").Value
l = Sheets("Start").Range("B3").Value
l = l + 1
yu = 1
mi = 2

While k < l
FilePath = "F:\Experiments Photos\Data Process\Results\" & k & ".txt"
Open FilePath For Input As #1
i = 3
Worksheets.Add().Name = k
```

```
While EOF(1) = False
   Line Input #1, strLine
   j = 1
   rogerArray() = Split(strLine, vbTab)

   For Each roger In rogerArray()
      Cells(i, j) = roger
      j = j + 1
   Next roger
   i = i + 1
Wend
   Range("O3").Select
   ActiveCell.FormulaR1C1 = "Diameter"
   Range("P3").Select
   ActiveCell.FormulaR1C1 = "D2"
   Range("Q3").Select
   ActiveCell.FormulaR1C1 = "D3"
   Range("O4").Select
   ActiveCell.FormulaR1C1 = "=(4*RC[-12]/PI())^0.5"
   Range("P4").Select
   ActiveCell.FormulaR1C1 = "=(RC[-1])^2"
   Range("Q4").Select
   ActiveCell.FormulaR1C1 = "=(RC[-2])^3"

Dim lastRow As Long
   lastRow = Range("A" & Rows.Count).End(xlUp).Row
   Range("Q1").Value = lastRow - 3
   Range("P1").Value = "Count"
Dim youbet1 As Range
   Set youbet1 = Range("O4:O" & lastRow)
```

```
Dim youbet2 As Range
   Set youbet2 = Range("P4:P" & lastRow)
Dim youbet3 As Range
   Set youbet3 = Range("Q4:Q" & lastRow)



   Range("O4").AutoFill Destination:=youbet1
   Range("P4").AutoFill Destination:=youbet2
   Range("Q4").AutoFill Destination:=youbet3
 ''''''''''''''''''''''''''''''''''''''''''
   Range("N1").Select
   ActiveCell.FormulaR1C1 = "D32"
   Range("N2").Select
   ActiveCell.FormulaR1C1 = "D10"
''''''''''''''''''''''''''''''''''''''''''''
   Range("O2").Value = WorksheetFunction.Average(youbet1)
   Range("O1").Value = WorksheetFunction.Sum(youbet3) /
WorksheetFunction.Sum(youbet2)
Sheets("Summary").Cells(yu, mi).Value = k
Sheets("" & k).Range("O1:O" & lastRow).Copy
Sheets("Summary").Cells(yu + 1, mi).PasteSpecial Paste:=xlPasteValues
Close #1
mi = mi + 1
k = k + 1
Wend
Worksheets("Summary").Activate
Dim LastC As Long
   LastC = Cells(1, Columns.Count).End(xlToLeft).Column
Cells(2, LastC + 2).Value = 0
ij = 3
```

```
While ij < 15
Cells(ij, LastC + 2).Value = Cells(ij - 1, LastC + 2).Value + 0.5
ij = ij + 1
Wend
Dim BinArray As Range
Set BinArray = Range(Cells(2, LastC + 2), Cells(14, LastC + 2))
Dim Tile As Range
Set Title = Range(Cells(1, 2), Cells(1, LastC))
Title.Copy
Cells(1, LastC + 3).PasteSpecial Paste:=xlPasteValues
rr = 2
res1Col = LastC + 3
While rr < LastC + 1
Dim lastRow2 As Long
lastRow2 = Cells(Rows.Count, rr).End(xlUp).Row
Dim Data As Range
Set Data = Range(Cells(5, rr), Cells(lastRow2, rr))
Dim Results As Range
Set Results = Range(Cells(2, res1Col), Cells(14, res1Col))
Results.FormulaArray = WorksheetFunction.Frequency(Data, BinArray)
rr = rr + 1
res1Col = res1Col + 1
Wend
Dim FinalCopy As Range
Set FinalCopy = Range(Cells(1, 2), Cells(2, LastC))
FinalCopy.Copy
Cells(16, LastC + 3).PasteSpecial Paste:=xlPasteValues
End Sub
```

References

1. Zhu, M., et al. *Inclusions removal by gas bubbles in steel continuous casting tundish*. 2013.
2. Wang, L., H.G. Lee, and P. Hayes, *A new approach to molten steel refining using fine gas bubbles.* ISIJ International, 1996. **36**(1): p. 17-24.
3. Wang, L., H.G. Lee, and P. Hayes, *Prediction of the optimum bubble size for inclusion removal from molten steel by flotation.* ISIJ International, 1996. **36**(1): p. 7-16.
4. Zheng, S. and M. Zhu, *Water model study on removing inclusions in a ladle with argon injected through nozzle and porous plug.* Acta Metallurgica Sinica, 2006. **42**(11): p. 1143-1148.
5. Sinha, A.K. and Y. Sahai, *Mathematical modeling of inclusion transport and removal in continuous casting tundishes.* ISIJ International, 1993. **33**(5): p. 556-566.
6. Zhang, L. and B.G. Thomas, *State of the art in the control of inclusions during steel ingot casting.* Metallurgical and Materials Transactions B: Process Metallurgy and Materials Processing Science, 2006. **37**(5): p. 733-761.
7. Lange, K.W., *THERMODYNAMIC AND KINETIC ASPECTS OF SECONDARY STEELMAKING PROCESSES.* International Materials Reviews, 1988. **33**(2): p. 53-89.
8. Kiessling, R., *Clean steel - A debatable concept.* Met. Sci., 1980. **15**(5): p. 161-172.
9. Zhang, L. and B.G. Thomas, *State of the art in evaluation and control of steel cleanliness.* ISIJ International, 2003. **43**(3): p. 271-291.
10. Pérez, J. and G.A. Irons. *Inclusion control model in the ladle metallurgy furnace*. 2013.
11. Guthrie, R.I.L., *Fluid flows in metallurgy - Friend or foe?* Metallurgical and Materials Transactions B: Process Metallurgy and Materials Processing Science, 2004. **35**(3): p. 417-437.

12. Guthrie, R.I.L., *A review of fluid flows in liquid metal processing and casting operations.* ISIJ International, 2009. **49**(10): p. 1453-1467.
13. Chattopadhyay, K., M. Isac, and R.I.L. Guthrie, *Physical and mathematical modelling of inert gas shrouding in a tundish.* ISIJ International, 2011. **51**(4): p. 573-580.
14. Wang, L.T., et al., *Fundamental of inclusion removal from molten steel by rising bubble.* Journal of Iron and Steel Research International, 2004. **11**(6): p. 5-9.
15. Zhang, L. and S. Taniguchi, *Fundamentals of inclusion removal from liquid steel by bubble flotation.* International Materials Reviews, 2000. **45**(2): p. 59-82.
16. Zhang, L., S. Taniguchi, and K. Matsumoto, *Water model study on inclusion removal from liquid steel by bubble flotation under turbulent conditions.* Ironmaking and Steelmaking, 2002. **29**(5): p. 326-336.
17. Zhang, L. and S. Taniguchi, *Fundamentals of inclusion removal from liquid steel by bubble flotation.* International materials reviews, 2000(81).
18. Yoon, R.H. and G.H. Luttrell, *The Effect of Bubble Size on Fine Particle Flotation.* Mineral Processing and Extractive Metallurgy Review, 1989. **5**(1-4): p. 101-122.
19. Zheng, X., P.C. Hayes, and H.G. Lee, *Particle removal from liquid phase using fine gas bubbles.* ISIJ International, 1997. **37**(11): p. 1091-1097.
20. McCann, D.J. and R.G.H. Prince, *Regimes of bubbling at a submerged orifice.* Chemical Engineering Science, 1971. **26**(10): p. 1505-1512.
21. Guthrie, R.I.L., M. Isac, and X.R. Ren. *The fundamentals of gas bubbling into liquid metals*. in *Conference of Metallurgists*. 2013. Montreal.
22. Irons, G.A. and R.I.L. Guthrie, *BUBBLING BEHAVIOUR IN MOLTEN METALS.* Canadian Metallurgical Quarterly, 1980. **19**(4): p. 381-387.
23. Kulkarni, A.A. and J.B. Joshi, *Bubble Formation and Bubble Rise Velocity in Gas−Liquid Systems: A Review.* Industrial & Engineering Chemistry Research, 2005. **44**(16): p. 5873-5931.
24. Irons, G.A. and R.I.L. Guthrie, *Bubble formation at nozzles in pig iron.* Metallurgical Transactions B, 1978. **9**(2): p. 101-110.

25. Muller, R.L. and R.G.H. Prince, *Regimes of bubbling and jetting from submerged orifices.* Chemical Engineering Science, 1972. **27**(8): p. 1583-1592.
26. Benzing, R.J. and J.E. Myers, *Low Frequency Bubble Formation at Horizontal Circular Orifices.* Industrial & Engineering Chemistry, 1955. **47**(10): p. 2087-2090.
27. Kumar, R. and N.K. Kuloor, *The Formation of Bubbles and Drops*. 1970. p. 255-368.
28. Sano, M. and K. Mori, *BUBBLE FORMATION FROM SINGLE NOZZLES IN LIQUID METALS.* Trans Jpn Inst Met, 1976. **17**(6): p. 344-352.
29. Mori, K., Y. Ozawa, and M. Sano, *A direct observation of interactions of gas jets with liquid metal at a submerged orifice.* Metallurgical Transactions B, 1979. **10**(4): p. 679-680.
30. Sano, M., Y. Fujita, and K. Mori, *Formation of bubbles at single nonwetted nozzles in mercury.* Metallurgical Transactions B, 1976. **7**(2): p. 300-301.
31. J. F. Davidson, B.O.G.S., *Bubble formation at an orifice in a inviscous liquid.* Trans. Inst. Chem. Eng., 1960. **38**: p. 335-342.
32. Leibson, I., et al., *Rate of flow and mechanics of bubble formation from single submerged orifices. I. Rate of flow studies.* AIChE Journal, 1956. **2**(3): p. 296-300.
33. Sano, M., K. Mori, and Y. Fujita, *DISPERSION OF GAS INJECTED INTO LIQUID METAL.* Tetsu To Hagane, 1979. **65**(8): p. 1140-1148.
34. Davidson, L. and E.H. Amick, *Formation of gas bubbles at horizontal orifices.* AIChE Journal, 1956. **2**(3): p. 337-342.
35. Sano, M., K. Mori, and T. Sato, *BUBBLE FORMATION AT SINGLE NOZZLES IMMERSED IN MOLTEN IRON.* Tetsu-To-Hagane/Journal of the Iron and Steel Institute of Japan, 1977. **63**(14): p. 2308-2315.
36. Kyriakides, N.K., et al., *Bubbling from nozzles submerged in water: Transitions between bubbling regimes.* The Canadian Journal of Chemical Engineering, 1997. **75**(4): p. 684-691.
37. Ozawa, Y., K. Mori, and M. Sano, *BEHAVIOR OF INJECTED GAS OBSERVED AT THE EXIT OF A SUBMERGED ORIFICE IN LIQUID METAL.* Tetsu-To-

Hagane/Journal of the Iron and Steel Institute of Japan, 1981. **67**(16): p. 2655-2664.

38. Mori, K., Y. Ozawa, and M. Sano, *CHARACTERIZATION OF GAS JET BEHAVIOR AT A SUBMERGED ORIFICE IN LIQUID METAL.* Transactions of the Iron and Steel Institute of Japan, 1982. **22**(5): p. 377-384.
39. Sevik, M. and S.H. Park, *SPLITTING OF DROPS AND BUBBLES BY TURBULENT FLUID FLOW.* Journal of Fluids Engineering, Transactions of the ASME, 95, 1973. **1**: p. 53-60.
40. Schulze, H.J., *Developments in Mineral Processing: Physico-chemical Elementary Processes in Flotation An Analysis from the Point of View of Colloid Science Including Process Engineering Considerations*. 1984, Berlin: Springer.
41. Evans, G.M., G.J. Jameson, and B.W. Atkinson, *Prediction of the bubble size generated by a plunging liquid jet bubble column.* Chemical Engineering Science, 1992. **47**(13-14): p. 3265-3272.
42. Martínez-Bazán, C., J.L. Montañés, and J.C. Lasheras, *On the breakup of an air bubble injected into a fully developed turbulent flow. Part 1. Breakup frequency.* Journal of Fluid Mechanics, 1999. **401**: p. 157-182.
43. Martínez-Bazán, C., J.L. Montañés, and J.C. Lasheras, *On the breakup of an air bubble injected into a fully developed turbulent flow. Part 2. Size PDF of the resulting daughter bubbles.* Journal of Fluid Mechanics, 1999. **401**: p. 183-207.
44. Tang, F., et al., *Formation mechanism of fine bubbles in the shroud nozzle of a ladle.* Beijing Keji Daxue Xuebao/Journal of University of Science and Technology Beijing, 2004. **26**(1): p. 22-25.
45. Arai, H., et al., *Model experiment on inclusion removal by bubble flotation accompanied by particle coagulation in turbulent flow.* ISIJ International, 2009. **49**(7): p. 965-974.
46. Arai, H., et al., *Water model experiment of removal of inclusions in liquid steel by bubble flotation.* Revue de Metallurgie. Cahiers D'Informations Techniques, 2008. **105**(6): p. 309-316+III-IV.

47. Zhang, L., J. Aoki, and B.G. Thomas, *Inclusion removal by bubble flotation in a continuous casting mold.* Metallurgical and Materials Transactions B: Process Metallurgy and Materials Processing Science, 2006. **37**(3): p. 361-379.
48. Rogler, J.P., L.J. Heaslip, and M. Mehrvar, *Inclusion removal in a tundish by gas bubbling.* Canadian Metallurgical Quarterly, 2004. **43**(3): p. 407-416.
49. Rogler, J.P., L.J. Heaslip, and M. Mehrvar, *Physical modelling of inclusion removal in a tundish by gas bubbling.* Canadian Metallurgical Quarterly, 2005. **44**(3): p. 357-368.
50. Arcos-Gutierrez, H., et al., *Mathematical analysis of inclusion removal from liquid steel by gas bubbling in a casting tundish.* Journal of Applied Mathematics, 2012. **2012**.
51. Meijie, Z., et al., *Numerical simulation and industrial practice of inclusion removal from molten steel by gas bottomblowing in continuous casting tundish.* Journal of Mining and Metallurgy, Section B: Metallurgy, 2011. **47**(2): p. 137-147.
52. Zhang, M.J., et al., *Mathematical simulation of molten steel flow field with gas blowing at tundish bottom.* Journal of Iron and Steel Research, 2006. **18**(6): p. 16-20.
53. Vargas-Zamora, A., et al., *Inertial and buoyancy driven water flows under gas bubbling and thermal stratification conditions in a tundish model.* Metallurgical and Materials Transactions B: Process Metallurgy and Materials Processing Science, 2004. **35**(2): p. 247-257.
54. Ramos-Banderas, A., et al., *Mathematical simulation and modeling of steel flow with gas bubbling in trough type tundishes.* ISIJ International, 2003. **43**(5): p. 653-662.
55. Li, D., B. Li, and J. He, *The Numerical Simulation of Two Phase Flows and Inclusion Removal in Tundish by Bottom Blowing.* INDUSTRIAL HEATING, 2000. **4**.
56. Li, D., B. Li, and J. He, *THE REMOVAL OF INCLUSION IN TUNDISH BY GAS BLOWING.* Acta Metallurgica Sinica, 2000. **36**(4): p. 6.

57. Feng, W.X., W.Q. Chen, and J.Z. Zhao, *Water model study on inclusion removal in tundish with argon bubbling.* Kang T'ieh/Iron and Steel (Peking), 2009. **44**(10): p. 21-25.
58. Bao, Y., J. Liu, and B. Xu, *Behaviors of fine bubbles in the shroud nozzle of ladle and tundish.* Journal of University of Science and Technology Beijing: Mineral Metallurgy Materials (Eng Ed), 2003. **10**(4): p. 20-23.
59. Wang, L.T., et al., *Mathematical model for removal of inclusion in molten steel by injecting gas at ladle shroud.* ISIJ International, 2005. **45**(8): p. 1138-1144.
60. Cho, J.S. and H.G. Lee, *Cold model study on inclusion removal from liquid steel using fine gas bubbles.* ISIJ International, 2001. **41**(2): p. 151-157.
61. Li, J., et al., *A new application of turbulator in removing inclusions by injecting gas from the shroud.* Metalurgia International, 2012. **17**(7): p. 57-62.
62. Zhang, Q.Y., L.T. Wang, and Z.R. Xu, *A new method of removing inclusions in molten steel by injecting gas from the shroud.* ISIJ International, 2006. **46**(8): p. 1177-1182.
63. Chattopadhyay, K., et al., *Physical and mathematical modeling of Inert gas-shrouded ladle nozzles and their role on slag behavior and fluid flow patterns in a delta-shaped, four-strand tundish.* Metallurgical and Materials Transactions B: Process Metallurgy and Materials Processing Science, 2010. **41**(1): p. 225-233.
64. Bai, H. and B.G. Thomas, *Bubble formation during horizontal gas injection into downward-flowing liquid.* Metallurgical and Materials Transactions B: Process Metallurgy and Materials Processing Science, 2001. **32**(6): p. 1143-1159.
65. Sahai, Y. and T. Emi, *Criteria for water modeling of melt flow and inclusion removal in continuous casting tundishes.* ISIJ International, 1996. **36**(9): p. 1166-1173.
66. Sano, M. and K. Mori, *GAS HOLDUP AND AVERAGE RISING VELOCITY OF BUBBLE SWARMS IN LIQUID METAL.* Tetsu-To-Hagane/Journal of the Iron and Steel Institute of Japan, 1978. **64**(12): p. 1714-1722.
67. Andreini, R.J., J.S. Foster, and R.W. Callen, *Characterization of gas bubbles injected into molten metals under laminar flow conditions.* Metallurgical Transactions B, 1977. **8**(3): p. 625-631.

68. Mori, K., M. Sano, and T. Sato, *SIZE OF BUBBLES FORMED AT SINGLE NOZZLE IMMERSED IN MOLTEN IRON.* Transactions of the Iron and Steel Institute of Japan, 1979. **19**(9): p. 553-558.
69. R. Clift, J.R.G., M.E. Weber, *Bubbles, Drops and Particles*. 1978, New York: Academic Press.
70. Atkinson, B.W., et al. *Bubble breakup and coalescence in a plunging liquid jet bubble column*.
71. Kuo, J.T. and G.B. Wallis, *Flow of bubbles through nozzles.* International Journal of Multiphase Flow, 1988. **14**(5): p. 547-564.
72. Dietrich, N., et al., *Bubble formation at an orifice: A multiscale investigation.* Chemical Engineering Science, 2013. **92**: p. 118-125.
73. Saarenrinne, P. and M. Piirto, *Turbulent kinetic energy dissipation rate estimation from PIV velocity vector fields.* Experiments in Fluids, 2000. **29**(SUPPL. 1): p. S300-S307.
74. ANSYS, *Fluent User and Theory Manual* 2014.
75. Hewitt, G.F., J.M. Delhaye, and N. Zuber, *Multiphase Science and Technology: Volume 2*. 1986: Springer.
76. Marshall, S.H., M.W. Chudacek, and D.F. Bagster, *A model for bubble formation from an orifice with liquid cross-flow.* Chemical Engineering Science, 1993. **48**(11): p. 2049-2059.
77. Liu, C., et al., *Effects of Orifice Orientation and Gas-Liquid Flow Pattern on Initial Bubble Size.* Chinese Journal of Chemical Engineering, 2013. **21**(11): p. 1206-1215.
78. Kolmogorov, A.N., *On the disintegration of drops in a turbulent flow.* Dokl. Akad. Nauk. SSSR, 1949(66): p. 825–828.
79. Batchelor, G.K., *The Theory of Homogeneous Turbulence*. Cambridge Science Classics. 1982: Cambridge University Press.